Subcellular Calcium Patterns In Ventricular Myocytes

Joshua Veasy, MSc

Thesis submitted to The University of Nottingham for the degree of Doctor of Philosophy

September 2018

Abstract

Understanding the biology and mechanisms as to how the heart contracts has long been a point of interest for biologists and mathematicians alike. Since inconsistent beating of the heart has been linked to multiple pathological conditions, research into this area has been extensive but we still only have some of the answers. One of the key findings over the last century has been the role of calcium in activating the machinery within the heart that drives contraction. Further studies have shown that when calcium is mishandled by the heart's myocytes, it can lead to some of these pathological conditions. Since such discoveries a major point of research into the heart has focused on the possible avenues that calcium mishandling can occur.

This thesis explores some of these avenues using a mathematical model of the ventricular myocyte developed by Thul and Coombes in their 2010 paper *Understanding cardiac alternans: A piecewise linear modeling framework* [1]. The chosen model contains key components involved in the movement of calcium within the myocyte. Moreover, the model used is piecewise linear and the stability of some important behaviours can be studied exactly without the need for approximations and reductions. This is often an issue in many other models used to study the calcium dynamics within a ventricular myocyte.

The avenue towards calcium mishandling that this thesis predominantly focuses on is that of intracellular calcium diffusion between the building blocks of ventricular myocytes known as sarcomeres. Our research extends previous research into how strong diffusion between sarcomeres can cause unwanted calcium dynamics. Further to this, we explore how the balance in the strength of different forms of calcium diffusion between sarcomeres can drive a variety of spatial patterns in terms of how the calcium is distributed throughout the cell. Throughout these studies we also investigate the role of other parts of the myocyte, particularly the sarcoplasmic reticulum Ca^{2+}-ATPase pumps and sarcoplasmic reticulum release in relation to diffusion driven instabilities.

As well as intracellular diffusion of calcium, this thesis considers the role of intercellular diffusion of calcium through gap junctions. This form of diffusion has historically been considered to a lesser extent than intracellular diffusion. As

such this thesis introduces new ideas concerning gap junctions. These include a role in driving the mishandling of calcium as well as altering behaviours driven by intracellular diffusion. An important message is that calcium diffusion within the myocyte is far more important in terms of how unwanted behaviours can appear than previous studies suggest.

Acknowledgements

I would first like to thank my supervisors Rüdiger Thul and Stephen Coombes. Their guidance and support throughout my studies has been invaluable and without it I would not have reached this point.

I am grateful to the many friends I have made in the mathematics department, in particular Jessie for being such a fantastic housemate during the majority of my Phd. I am also thankful to the many great friends I have made in the University of Nottingham Kayak club for providing me with great times on and off the water.

I wish to thank my family for their continued love, support and encouragement. A final special thanks goes to Agata. She has been an absolute rock for me, being there with love and support throughout it all.

Contents

List of Figures

List Of Abbreviations

APD	Action Potential Duration
Ca^{2+}	Calcium
CICR	Calcium-Induced-Calcium-Release
CRU	Calcium Release Unit
CSQN	Calsequestrin
DADs	Delayed Afterdepolarizations
DI	Diastolic Interval
EADs	Early Afterdepolarizations
ECM	Extracellular Matrix
JSR	Junctional Sarcoplasmic Reticulum
K^{+}	Potassium
NCX	Sodium-Calcium Exchanger
MCU	Mitochondrial Calcium Uniporter
NCLX	Mitochondrial Sodium-Calcium Exchanger
PCL	Pacing Cycle Length
PWL	Piecewise Linear
SERCA	Sarcoplasmic Reticulum Ca^{2+}-ATPase
SCA	Spatially Concordant Alternans
SDA	Spatially Discordant Alternans
SCR	Spontaneous Calcium Release
SR	Non-Junctional Sarcoplasmic Reticulum
TWA	T-Wave Alternans

1 Introduction

Calcium, in its ionic form Ca^{2+}, is a key component of the cardiac system. In respect to the Ca^{2+} found in cardiac myocytes, Ca^{2+} helps regulate heart contraction as a direct activator for the myofilaments, which cause the heart to contract [4, 5]. The amount of total free intracellular Ca^{2+}, the Ca^{2+} found in the cytosol and subsarcolemmal space, determines the strength of contraction at each heart beat. Mismanagement of the concentration levels of Ca^{2+} from beat to beat has been linked to some unwanted cardiac behaviours, such as cardiac alternans.

The term cardiac alternans is used to describe an oscillation in the contraction strength of the heart from beat to beat, at a specific heart rate. These cardiac alternans have been linked to types of cardiac arrythmia, such as ventricular fibrillation [6], and, therefore, the many problems that cardiac arrythmia can cause [7]. Hence, understanding the underlying causes of cardiac alternans, such as Ca^{2+} alternans, is considered of great importance and interest. Ca^{2+} alternans refers to a beat-to-beat oscillation in the levels of intracellular Ca^{2+}, found in cardiac cells. The term can be used to describe such behaviour at subcellular or cellular levels. A more in depth discussion about how cardiac myocytes cause the heart to contract, including the role of Ca^{2+} within this contraction, is included in the first half of Chapter 2.

Many models have been proposed to describe the changing of these Ca^{2+} levels, known as the Ca^{2+} cycle, in the hope to determine some of the underlying mechanisms for Ca^{2+} alternans. Mathematical models suggest that Ca^{2+} alternans occur due to a period-doubling bifurcation. One aim of this thesis is to determine such bifurcations as we vary physiologically important model parameters. Since many myocyte models contain large numbers of variables and are nonlinear, direct analysis of such models is challenging. As such, these models are often reduced to low dimensional maps [8, 9, 10]. This means that the analysis and simulations may not always agree due to assumptions made when reducing these models to low dimensional maps. One of the models that does not have this problem is the piecewise linear (PWL) Shiferaw-Karma model developed by Thul and Coombes [1].

By circumventing the need to reduce the model to one or two dimensional maps, the PWL Shiferaw-Karma model allows for direct stability analysis of the systems orbits and synchronised states without the fear of disagreement between analysis and simulations. This provides the added advantage of being able to find the values of parameters within the model at which bifurcations in the system occur. The ability to do this means that the behaviour at the onset of a bifurcation can be studied without the need for tedious simulations to find the onset point. Within this thesis we seek to exploit this advantage of the PWL Shiferaw-Karma model to help us to further understand how the processes involving Ca^{2+} may cause Ca^{2+} alternans. Since the PWL Shiferaw-Karma model does not require reduction for an analytical stability approach to be deployed, we are able to draw highly reliable conclusions. Further information about the PWL Shiferaw-Karma model, along with some discussion about the findings of other cardiac myocyte models, is included in the second half of Chapter 2.

One of the most studied parts of the myocyte is the sarcoplasmic reticulum Ca^{2+}-ATPase (SERCA) pump. The role of the SERCA pump is to replenish Ca^{2+} levels in the non-junctional sarcoplasmic reticulum (SR) after the heart contracts. When the SR is not fully replenished in time, Ca^{2+} alternans can ensue. Mathematical models have illustrated that a reduction in the uptake strength of the SERCA pump can help to promote alternans [8, 11]. It has also been shown that a significantly large reduction can suppress alternans [12]. In Chapter 3, through the use of our stability approach and simulations, we seek to find some underlying reasons to why these two apparently conflicting views exist.

Whilst providing further insight into the role of the SERCA pump will form part of Chapter 3, the main focus of this chapter and Chapter 4 will be around intracellular diffusion. Unlike the SERCA pump, very few models have focused on the role of intracellular diffusion [1, 13] in promoting alternans. Within this thesis we will expand this limited knowledge by focusing on both the role of cytosolic and SR Ca^{2+} diffusion in the myocyte. Current knowledge shows that strong cytosolic diffusion can promote Ca^{2+} alternans whilst there appears to be no literature focused solely on the role of Ca^{2+} diffusion in the SR. One of the main goals within this thesis is to rectify this lack of research by studying

both these forms of diffusion individually as well as their combined effect on the calcium dynamics within the PWL Shiferaw-Karma model.

Intracellular diffusion also has a role in the spatial Ca^{2+} distribution within the myocyte. Since alternans have been shown to appear in a multitude of spatial patterns at the subcellular level [14], we will study how the diffusion rates drive these patterns in Chapters 3 and 4. These studies shall include a focus on phenomena known as spatially concordant alternans (SCA) and spatially discordant alternans (SDA). Since SDA has been deemed more pathological than SCA [15], finding any links between the two would be highly beneficial in terms of treating conditions linked to SDA.

Considering such spatial patterns are potentially linked to bifurcations of the systems they are likely to be dictated by the eigenvectors of the system. Since the eigenvalues of the PWL Shiferaw-Karma model can be found directly, the eigenvectors of the network can also be found. In Chapter 3 we will illustrate how these eigenvectors are found. We will also demonstrate that the spatial behaviour of the system just after a bifurcation is reflected by the shape of the eigenvector.

Another area in which Ca^{2+} diffusion can occur is between cells via gap junctions. Much like with intracellular diffusion, the literature concerning this is limited [16]. Whilst the lack of literature may be down to the belief that Ca^{2+} is unlikely to travel in this manner [17] or that the difference between the diffusion rates of the voltage and Ca^{2+} is so great that Ca^{2+} diffusion is ignored [18], with evidence also supporting its existence [19] it should not be overlooked. Thus in Chapter 5 we extend our studies into the effects of Ca^{2+} diffusion to include gap junctions. With this we show that Ca^{2+} diffusion through gap junctions should not be overlooked in terms of its contribution towards alternans. Chapter 6 concludes this thesis with a summary of our findings and discusses ways in which our research can be extended.

2 Background and Methodology

Some of earliest experimental developments of the calcium cycle within the ventricular myocyte appeared during the 1960s and 1970s, see reviews [20, 21]. Since then, as experimental techniques have improved, so has our understanding of the calcium cycle and both its related processes and the pathological conditions associated with it. This in turn has been reflected in the modelling world with both the improved detail of biological processes contained within models and the ability to strike a balance between simplifying the description of the processes whilst maintaining contact with biological reality. Within this chapter we discuss both the biological aspects of the calcium cycle, with emphasis on those parts that are of interest to us, as well as some of the models that have been developed over the last few decades.

2.1 Biological Background

When talking about Ca^{2+} alternans and the Ca^{2+} cycle, we refer to the Ca^{2+} dynamics found in a type of cell known as a cardiac myocyte. These are the cells that contain the myofilaments responsible for contracting the heart. In this thesis we will focus upon ventricular myocytes, which contain an extensive T-tubule network, unlike atrial myocytes. This network means that the calcium dynamics within the centre of the myocyte are similar to those at the edge of the myocyte. As such a healthy ventricular myocyte should have an even distribution of Ca^{2+} within the cytoplasm. On the other hand, healthy atrial myocytes display a gradient between the edge and centre of the myocyte when considering its Ca^{2+} transient. The focus of our thesis is to understand how aspects of the calcium dynamics can cause the loss of homogeneity within these ventricular myocytes.

2.1.1 The Ventricular Myocyte and The Calcium Cycle

In Figure 2.1A we present a schematic for the parts of the ventricular myocytes that we consider throughout this thesis. The figure shows five of the key components of the ventricular myocyte: the sarcolemma, subsarcolemmal space, bulk cytosol, the SR and junctional SR (JSR), as well as the extracellular ma-

trix (ECM). The majority of the myocyte volume is taken up by the cytosol, which contains the contractile apparatus, as well as other organelles not shown here. The SR is a complex network threaded throughout the myocyte that makes up most of the remaining volume. The subsarcolemmal space refers to the part of the cytosol that lies closest to the sarcolemma. This is the space into which channels crossing the sarcolemma deliver molecules from the ECM as well as from where they are removed out of the myocyte. One such key part are the T-tubules which, as Figure 2.1A illustrates, are invaginations of the sarcolemma. These invaginations allow the transport of molecules across the sarcolemma throughout the myocyte. We will explain the importance of this later within this section. It is worth stating that although prevalent in fully developed mammalian ventricular myocytes, T-tubules have yet to be found in birds, reptiles, fish or amphibians [22]. Furthermore, the number of T-tubules increase with maturation of the ventricular myocyte [23]. The bulk of this thesis is concerned with fully matured mammalian ventricular myocytes. However, it has been shown that T-tubules can appear in mammalian atrial myocytes. The extent of these atrial T-tubule networks appear dependent on the size of the mammal, whilst sparse networks have been found in rats [24], much more extensive networks have been found in larger mammals such as sheep and humans [25]. Thus, the work done in this thesis could be applied to atrial myocytes of larger mammals with minimal adaptations.

Figure 2.1A is a simplistic picture of the ventricular myocyte. In reality the SR is a complex tubular network that runs throughout the ventricular myocytes surrounding the T-tubules [26]. The surrounding of these T-tubules by the SR forms a key signalling component known as the Ca^{2+} release units (CRUs). Figure 2.1B shows a CRU in more detail whilst the section marked out by the dashed box in Figure 2.1A shows where they are found. Figure 2.1B contains a few of the channels we would expect to find in a CRU along with the five parts of the myocyte shown in Figure 2.1A and the ECM. As we can see in Figure 2.1B the L-Type Ca^{2+} channel and the SR release channel are directly opposed to each other. They are opposed in this way as the calcium entering from the L-Type channel activates release of further calcium from the SR release channel. The other two channels displayed in Figure 2.1B are the sarcoplasmic reticulum Ca^{2+}-ATPase

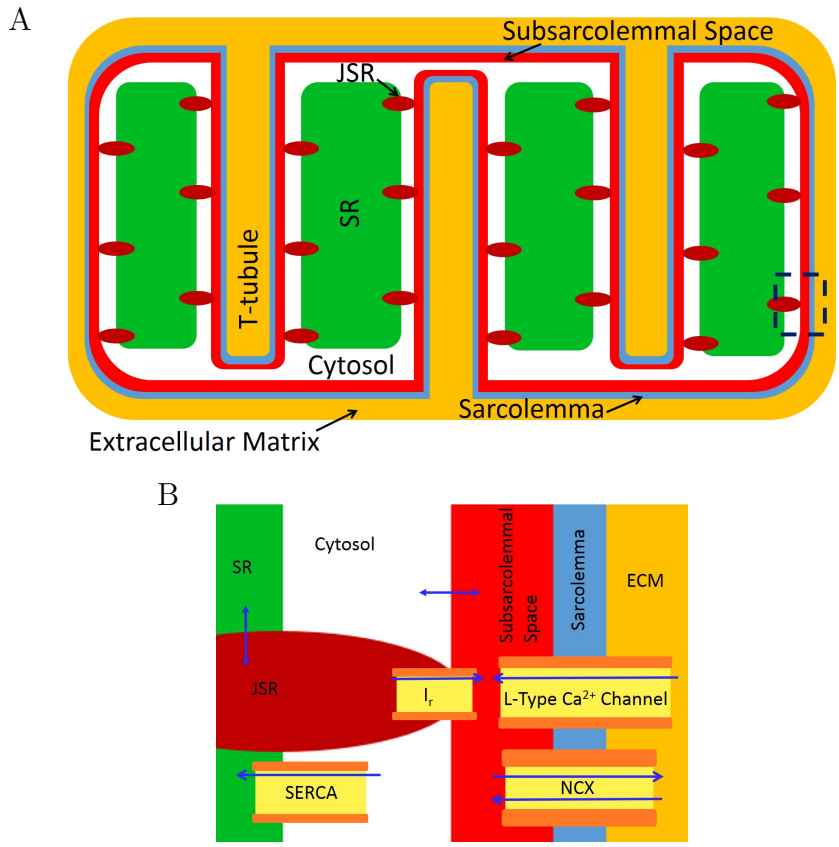

Figure 2.1: Diagram of ventricular myocyte and CRU. (A) A simple diagram showing the parts of a ventricular myocyte that are of interest to us. (B) A closer look at a Ca^{2+} release unit (CRU). Channels contained in B are the L-Type Ca^{2+} Channel, the SERCA pumps, the SR release channel (I_r) and sodium-Ca^{2+} exchange (NCX). The blue arrows indicate how Ca^{2+} moves around the CRU. Blue arrows not contained within a channel represent simple diffusion.

(SERCA) pump and the sodium-calcium exchanger (NCX). The function of the SERCA pump is to pump calcium from the cytosol into the non-junctional SR whilst the NCX moves calcium in and out of the myocyte by exchanging it with sodium.

Figure 2.1A only gives some of the organelles contained within the ventricular myocyte. It must also be stated that the ratio in volume between the cytosol and SR is different to that suggested in Figure 2.1. The enlargement of the SR in these diagrams is for the purpose of showing the relationship of the SR with the T-tubules. The diagrams in Figure 2.1 show the parts of the ventricular myocyte we shall focus on from a modelling perspective. First, we review the process of excitation-contraction coupling as this is highly pertinent to the process of calcium cycling.

Excitation-contraction coupling describes the process from a myocyte being electrically excited to the contraction of the heart [4, 5]. This process can be broken down into four major parts. The first part is the initiation of a depolarising action potential that travels throughout the myocyte. The cardiac action potential is a change in voltage across the cell membranes of multiple heart cells, including cardiac myocytes. The cardiac action potential is initiated by a group of specialized cells and uses gap junctions to then pass from one cell to the next. The initiation of the depolarising action potential usually occurs at the sino-atrial node, located in the right atrium away from the ventricular myocytes. The action potential then travels across the left and right atrium before arriving at the atrioventricular node. It is then distributed by the atrioventricular node, via branches from its lower section, throughout the left and right ventricle, eventually being distributed to the ventricular myocytes. Upon arrival to the ventricular myocytes, the action potential sweeps throughout the cell almost instantaneously causing the membrane to depolarize. The action potential is able to sweep throughout the cell at such pace due to the T-tubules. These T-tubules provide direct paths for the action potential to take throughout the myocyte. This initiation step lies outside of our modelling as we are only concerned with the behaviour within the ventricular myocytes (or networks of ventricular myocytes) and not the propagation of the action potential stimulus across the heart. Since this thesis is focusing on the behaviour of calcium within ventricular myocytes, it is from this point in the process of excitation-contraction coupling that our studies focus on.

Once the membrane depolarises, the second part begins with activation of channels along the membrane. The depolarisation of the membrane activates channels that control the transport of Ca^{2+} across the membrane, primarily the NCX and the L-Type Ca^{2+} channel. The activation of these channels leads to a large influx of Ca^{2+} into the cytosol. The influx from the L-Type channel enters into an area known as the dyadic cleft, which is a small area found in the subsarcolemmal space between the sarcolemma and the junctional area of the SR. The sudden increase of the Ca^{2+} concentration in the dyadic cleft induces further release of Ca^{2+} from the SR. This occurs as high levels of Ca^{2+} allow it to bind with parts of the junctional SR known as ryanodine receptors, activating the

SR release. Such a release from an individual CRU is known as a spark and on average a ventricular myocyte contains approximately 20,000 CRUs. This process where Ca^{2+} activates further Ca^{2+} release is known a Ca^{2+}-induced-Ca^{2+}-release (CICR) and is a key part of the excitation-contraction process.

Once released into the dyadic cleft, the Ca^{2+} then diffuses into the bulk cytosol and so starts the third part. This causes an increase of the free intracellular Ca^{2+} concentration, also known as the Ca^{2+} transient, allowing the Ca^{2+} to bind to the myofilament protein troponin C. Upon binding the contractile parts of the myofilaments are activated, allowing the myofilaments to contract and thus the heart to contract. The strength of the contraction is proportionally dependent upon the amount of Ca^{2+} found within the cytosol.

The final part, in which the levels of Ca^{2+} within the cytosol must deplete to allow for heart relaxation, starts once contraction completes. This is achieved by many different mechanisms but the two most dominant pathways by which Ca^{2+} is removed are the SERCA pumps and the NCX. As can be seen in Figure 2.1B the SERCA pumps remove Ca^{2+} directly from the bulk cytosol into the SR whilst the NCX extrudes Ca^{2+} from the subsarcolemmal space across the membrane and out into the extracellular matrix. The amount of Ca^{2+} removed into the extracellular matrix in this phase should be equivalent to the amount that entered at the beginning of the heart beat for the cell to maintain dynamic homeostasis.

2.1.2 Layout Of Myofibrils

In this thesis we will be look at both subcellular and cellular networks. To extend to both one and two spatial dimensions, we need to consider in more detail the contractile elements of the ventricular myocytes. The contractile elements of the ventricular myocyte are contained in rod like parts of the myocytes known as myofibrils. These myofibrils lie in the longitudinal direction along the myocyte and are packed tightly side by side, as well as above and below each other, in the ventricular myocyte right up to the sarcolemma [27]. Figure 2.2 gives a very basic idea of how these myofibrils are divided up into sarcomeres. These sarcomeres are the basic unit for contraction contained in the myocyte and are divided along

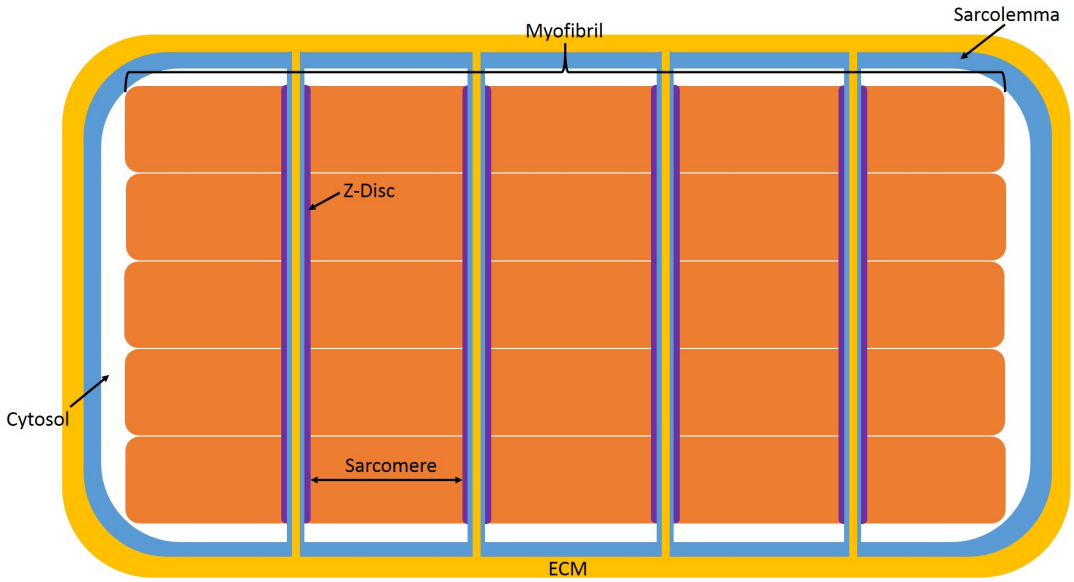

Figure 2.2: Diagram illustrating how myofibrils are stacked within the myocytes. The sarcomeres within each myofibril line up in the transversal direction along what are known as z-discs. These z-discs are made of the T-tubules and sarcolemma, highlighted within the purple regions. Although not shown here, the SR network surrounds this myofibrils and also crosses the z-discs.

the myofibrils by z-discs. It is within these z-discs that the T-tubules are usually found, although it has been shown that the T-tubule system may contain branches in the longitudinal direction of the cell between z-discs [28, 29]. The sarcoplasmic reticulum network surrounds these myofibrils and also crosses the z-discs. This provides one of the paths for Ca^{2+} to diffuse throughout the myocyte. The fact these sarcomeres are so clearly defined by the z-discs and edges of the myofibrils, allows us to easily create well structured model networks.

In this thesis we will model these 1D and 2D subcellular networks using rectangular grids. We can do this since it has been shown that these z-discs within the myofibrils in cardiac myocytes become aligned during the maturing process of cardiac myocytes [30]. Thus by using purely the aligned z-discs as borders and combining the dynamics of all the sarcomeres between them, we can split the myocyte longitudinally to create 1D networks. To move from 1D to 2D networks we then take these longitudinal sections and split these in the transversal direction. We achieve this by treating the gaps between the myofibrils as transversal borders between sections of the myocyte.

2.1.3 Gap Junctions In Cardiac Myocytes

We also study cellular networks with gap junction coupling. To do this we first introduce a very basic model for gap junctions. Gap junctions are connections between neighbouring cells allowing for the flow of both molecules and action potentials between the cell. However, biologically gap junctions are more complicated. Thus it is worth discussing how gap junctions work in more detail. This provides us with some considerations we need to take into account when looking at the model's findings. Our understanding of how gap junctions work in terms of cardiac myocytes is predominantly informed by the review by Severs *et al* [31].

Whilst gap junctions are found along the length of the ventricular myocyte's membrane, they tend to be found in greater number at the end of the cells. This is to promote a longitudinal direction of travel for the action potential throughout the ventricular myocardium. These gap junctions are assembled from a group of proteins known as connexins, with connexin43 being the predominant form found in all mammalian ventricular myocytes. The presence of connexin40 and connexin45 have also been shown in canine ventricular myocytes [32] and that all three interact to form gap junctions. However, other studies have shown that connexin40 is not present in all fully developed, mammalian ventricular myocytes [33].

Gap junctions form between cells in much the same way throughout the body. As described in the review by Bruzzone *et al* [34], the connexins in each cell align into a hexagonal group of six known as a hemichannel. Two hemichannels align between the cells to form a gap junction. With the gap junction formed between ventricular myocytes, its main role is to allow the propagation of the action potential between cells. The diffusion of Ca^{2+} through gap junctions, whilst theoretically possible, has yet to be confirmed. While studies on species such as rats suggest that it may be unlikely [17] that calcium diffuses this way in ventricular myocytes, studies on different mammalian species suggest some movement of Ca^{2+} may occur [19].

2.1.4 What Are Alternans and Why Are They Important?

A visual representation of calcium alternans can be seen in Figure 2.3A. In both Figures 2.3A and 2.3B, the time between each beat is denoted by PCL which stands for pacing cycle length. In reality the PCL represents the time from the arrival of one action potential released from the atrioventricular node to the next. As we can see in Figure 2.3A calcium alternans are the beat to beat oscillations in the amplitude of the bulk cytosolic Ca^{2+} concentration within cardiac myocytes under a constant heart rate.

Figure 2.3B presents a visual representation of action potential duration (APD) alternans. As Figure 2.3B shows, APD alternans are the beat to beat oscillations in the length of the APD, the length of time the voltage is above its base level, and the diastolic interval (DI), the amount of time between each APD. Despite these variations the PCL, which is the sum of the APD and DI lengths remains constant. These are normally found in the pattern of long APD, short DI during one beat followed by short APD, long DI during the following beat.

The very first study of what are known as mechanical alternans, the beat to beat oscillation in contraction strength, was performed by Traube in 1872 and the first studies revealing electrical alternans, the beat to beat oscillation in the APD, occurred towards the start of the 20th century [35]. Much later, the first studies of alternating patterns in the intracellular calcium concentration levels began [36, 37, 38] due to the development of techniques allowing for the measurement of intracellular Ca^{2+}. Since these first studies into calcium alternans the field has moved along at a rapid pace, quickly showing the link between calcium alternans and electrical alternans, also known as APD alternans, due to the bidirectional coupling of the calcium and voltage systems. The term bidirectional coupling refers to how both the calcium and voltage systems within the myocyte directly affect one another. This bidirectional coupling has led to some debate about whether APD alternans induce calcium alternans or whether it is the other way around.

There is evidence that APD alternans may come first due to the relationship between the APD and DI lengths [39, 40]. However, more recent experimental studies involving the clamping of voltage reveal how calcium alternans can occur

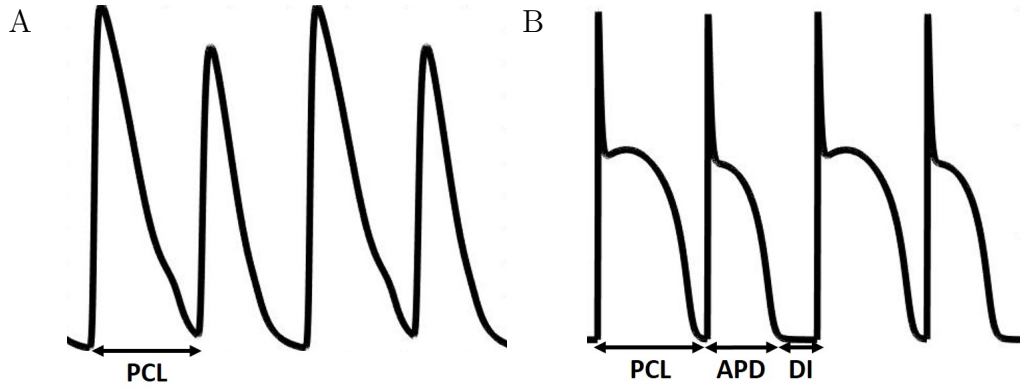

Figure 2.3: Alternan traces. A trace of calcium alternans (A) and a trace of APD alternans (B) taken from the Shannon model [46]. Acronyms stand for pacing cycle length (PCL), action potential duration (APD) and diastolic interval (DI).

independently of electrical alternans [41, 42, 43] suggesting that calcium is the primary instigator. An experimental study performed by Pruvot *et al*, in 2004, involving a direct comparison of the restitution curve against calcium cycling without voltage clamping provides further evidence of this [44]. The restitution curve describes the recovery of the APD as a function of the DI [45]. Restitution curves are described in more depth in Section 2.2.1.

Although the order in which calcium alternans and APD alternans occur is still up for debate, the fact they are linked is one of the many reasons why understanding calcium alternans is so important. Due to being linked with APD alternans, calcium alternans can be deemed as a precursor to what are known as T-Wave alternans (TWA), also known as repolarisation alternans. T-Wave alternans are the manifestation of APD alternans at the tissue level and have been directly linked to many conditions such as ventricular arrythmia [6, 47], which is a precursor for sudden cardiac arrest [7], long QT-syndrome [48], which is a precursor to a form of ventricular tachycardia known as torsade de pointes, and acute myocardial ischemia [49] to name a few examples. Considering the seriousness of these conditions, it is for these reasons that the study of calcium alternans is of such importance.

As well as the general description of alternans given at the beginning of this section, calcium alternans, along with APD alternans, can display spatial alternans. If we consider the sarcomere networks described in Section 2.1.2, one basic pattern that alternans may display are nearest-neighbour alternans. This is sim-

ply a beat-to-beat oscillation between neighbouring sarcomeres of the amplitude of the peak Ca^{2+} concentration in the bulk cytosol. Some other spatial patterns that have been of interest to many in the field are spatially concordant and discordant alternans. A basic diagram illustrating these two behaviours within a single myocyte can be seen in Figure 2.4. An example of spatially concordant alternans is shown in Figure 2.4A. During one beat the peak free intracellular Ca^{2+} concentration is high, represented by the colour red, and on the next beat it is low, represented by the dark blue colour. On each beat the peak concentration is uniform throughout the myocyte, bordered by the membrane represented by the light blue colour. On the other hand, in Figure 2.4B, we see spatially discordant alternans. During each beat one half of the myocyte has a high peak intracellular Ca^{2+} concentration, whilst the other half has a low peak concentration. On the next beat these two halves switch. This half and half split is the most obvious form of spatially discordant alternans, but any regional splitting that follows this beat to beat pattern is regarded as SDA. There is evidence to suggest that patterns similar to nearest-neighbour spatial alternans, or indeed just chaotic patterning within subcellular alternans, can be a precursor to the formation of spatially discordant alternans within cells [14]. At a tissue level APD alternans can be described as spatially concordant or discordant. For example, APD alternans are deemed spatially discordant if one region of tissue has a short APD and long DI whilst another region has a long APD and short DI during the same beat and then these roles are reversed during the next beat.

These different forms of alternans, along with many others, have been of great interest to both mathematicians and biologists due to the links to numerous cardiac pathologies. In the next section, we shall discuss the different mathematical modelling approaches taken and also how these approaches may inform each other along with our research.

In experimentation Ca^{2+} alternans are seen by the use of fluorescent indicators. An example of this, taken from the paper by Diaz *et al* [2], can be seen in Figure 2.5. These experiments were performed on isolated on myocytes. The three panels equate to the responses of the myocyte to three consecutive voltage pulses. The voltage pulse is represented by the trace given above the panel. Com-

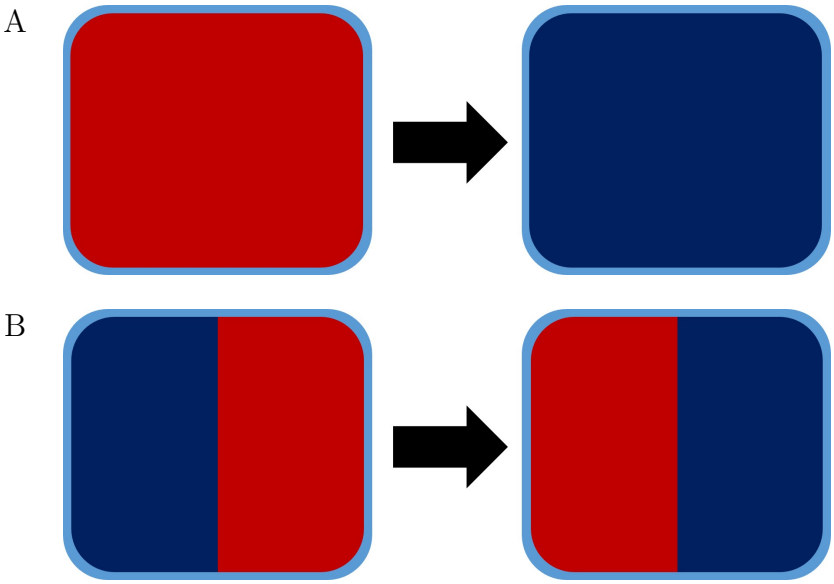

Figure 2.4: Diagrams of SCA and SDA. (A) A diagram representing spatially concordant alternans (SCA) within single myocyte. The red represents a high peak intracellular Ca^{2+} concentration whilst the dark blue represents a low peak intracellular Ca^{2+} concentration. The light blue represents the myocytes membrane. The arrow represents the transition from one beat to the next. (B) A diagram representing spatially discordant alternans (SDA) within a single myocyte. Colours are the same as in A

paring these panels we can see that pulsus one and three lead to much higher Ca^{2+} concentrations than pulsus two. The other takeaway from these experimental results is the difficulty to discern sarcomere boundaries, thus the importance of mathematical modelling studies such as those contained within this thesis.

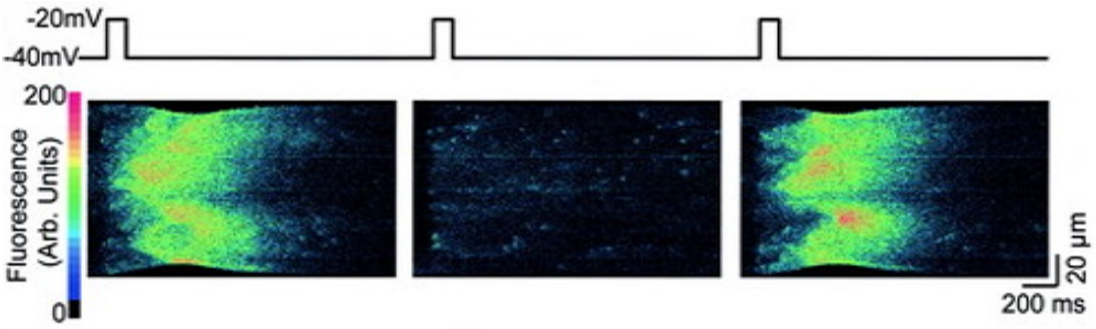

Figure 2.5: Experimental results from Diaz *et al* [2]. The top trace represents the spacing of the voltage pulsus whilst the panels are linescans of the myocyte showing the calcium concentrations throughout each pulse.

2.2 Literature Review

Although action potential models can trace their roots back to the Hodgkin and Huxley model [50], the introduction of calcium currents came later with one such example being the introduction of McAllister *et al*'s model of a Purkinje fibre in 1975 [51]. Soon after the first model of a ventricular myocyte was developed by Beeler and Reuter in 1977 [52], the world of myocyte modelling began. Since then models have increased in accuracy through the use of a growing set of experimental data. This data has allowed modelers to create better representations of the biological processes involved in the calcium cycle. Due to their improving accuracy, models have been used more and more extensively to research the many possible avenues under which calcium alternans and other instabilities can occur. They are also used to understand the effects of the bidirectional coupling between the calcium and voltage systems within the myocyte. This is a key area of interest as an instability in one of the dynamics usually leads to an instability in the other.

2.2.1 Voltage Driven Instabilities

The first studies [53, 54] into the onset of APD alternans preceded the development of calcium dynamics within myocyte modelling. As discussed in Section 2.1, one possible cause of calcium instabilities within the myocyte may be associated with the relationship between the APD and DI. This relationship is often described using the APD restitution curve. APD restitution is the primary method to study the voltage stability. The voltage is deemed stable when the length and

shape of the APD and DI are consistent from beat to beat. Any other shape or pattern seen within the voltage is deemed to represent an instability in the voltage. These studies are still worth consideration as they set the groundwork for later.

The idea of APD restitution was first discussed by Nolasco and Dahlen [39]. They showed that the relationship between the APD and DI could be used to predict the possibility of APD alternans within a graphical model. By plotting the current APD length against the previous DI length, they used the shape of the resultant curve to suggest whether APD alternans would develop or not. Using mathematical theory developed by Riggs [55], they suggested that a restitution curve with a gradient greater than 1 would equate to the onset of alternans. In 1984 the mathematical theory of APD restitution was extended by Guevara *et al* [56]. By developing an equation linking the length of the current APD to the length of the previous APD and then studying the steady state of such an equation, they revealed that the onset of APD alternans could be described by a period-doubling bifurcation. They then demonstrated that these period-doubling bifurcations of the steady state would occur when the APD restitution curves had a slope greater than one. Examples of these restitution curves taken from a study by Koller *et al* [3] can be seen in Figure 2.6. In their study Koller *et al* revealed how increasing the external potassium concentration decreased the range of short DI values for which the restitution curve had a gradient greater than 1. This equated to suppressing the chances of APD alternans. These curves were generated from experimental results.

More recent work on a piecewise linear map describing the next APD as a function of the current DI by Berger *et al* [57] found that behaviour of the system close to the period-doubling bifurcation point could suggest a smooth bifurcation whilst the behaviour of the system further away from the bifurcation point could suggest a border-collision bifurcation. By border-collision bifurcation we are referring to a bifurcation point that on a bifurcation diagram is non-differentiable. Further to this, they pointed out than when data points close to the bifurcation were limited it could be hard to distinguish which of these two bifurcations are actually occurring. They termed this an unfolded border-collision

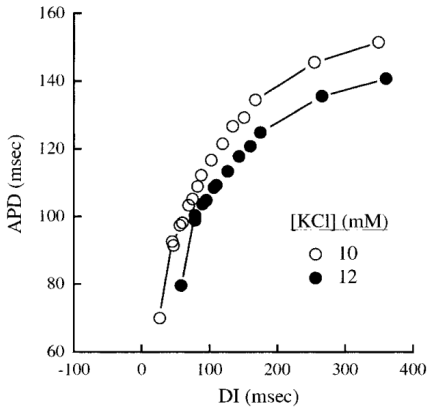

Figure 2.6: Two restitution curves from the study by Koller *et al* [3]. The white dots represent data from experiments where the external potassium concentration ([KCl]) was 10 mM whilst the black dots are from experiments where the concentration was 12 mM.

bifurcation and suggested that to track these bifurcations, models would need a way to include elements of nonsmooth behaviour. These nonsmooth behaviours could include mechanisms in the myocyte that become activated or altered when a threshold is reached, such as the activation of the L-type Ca^{2+} channel.

Mathematical groundwork for restitution curves opened the door for modelling research into the effects of APD restitution on alternans. Qu *et al* [58] revealed that steep APD restitution could cause SCA. Furthermore, they demonstrated that, when combined with conduction velocity restitution, these SCA can then turn into SDA. Along similar lines Fox *et al* [59] created one of the first detailed, experimentally accurate ionic models for the voltage measured in a canine ventricular myocyte by combining attributes of the well known models by Lou and Rudy [60], Winslow [61] and Chudin [41]. In fact the Fox model is so successful, that many of its equations used for the ionic currents within myocytes are still used to this day. Using their model, Fox *et al* demonstrated that the restitution curve could be flattened by either increasing the magnitude of some potassium channels or decreasing the magnitude of the L-Type Ca^{2+} channel. However, such findings based on the L-Type Ca^{2+} channel immediately raise the problem of whether the APD alternans are due to the restitution curve or due to a mishandling in the calcium dynamics and thus the result of calcium alternans. A similar study by Mahajan *et al* [62] has tried to unpick the close relationship by studying the onset of alternans due to changes in the L-Type Ca^{2+} chan-

nel. Their findings showed that at rapid pacing periods the slope of restitution increased dramatically. Mahajan *et al* suggested such behaviour implied APD restitution as the main driver for alternans at very fast pacing periods. Such rates tend to be linked more with conditions such as fast ventricular tachycardia and fibrillation as opposed to healthy hearts [63].

Despite the number of findings discussed within this section that give possible causes of APD alternans unrelated to the calcium dynamics, the role the calcium dynamics have and how it controls the shape of the action potential cannot be overlooked. The increasing consensus that, in general, calcium alternans precede APD alternans has caused mathematical biologists to move away from studying the onset of alternans at the cellular level from the electrical perspective. However, many studies still note the importance of APD alternans due to the bidirectional coupling between the voltage and calcium dynamics. One such modelling study by Livshitz and Rudy [64] focused on pacing rates slow enough that APD restitution was not the primary cause of alternans. They revealed that increasing the inward rectifier K^+ current suppressed APD alternans but had little effect on calcium alternans suggesting a weakening of the bidirectional coupling. This further supports the importance of calcium alternans, particulary in healthy hearts, as it suggests clinical approaches for suppressing alternans need to focus on calcium dynamics.

This recognition has led to a large push in the modelling of processes involved within calcium dynamics of the ventricular myocytes. Furthermore, the diversity of research into which parts of the myocyte can cause calcium alternans is much more spread and detailed when compared to the simplicity of the restitution curve. This is due to the shift of focus onto the values of parameters within calcium mechanisms for the onset of alternans, as opposed to the lengths of the APD and DI used in restitution curves.

2.2.2 Calcium Driven Instabilities

Early calcium models mainly focused on replicating experimental results, as opposed to focusing on instabilities relating to alternans. This has led to modelling insights such as the need to keep the Ca^{2+} concentration subsarcolemmal space,

in which CICR takes place, as its own variable [65] and the use of local control [66, 67] to achieve high gain and graded SR Ca^{2+} release. Many reviews have looked over the general history of model development [68, 69, 70, 71], but our focus will revolve around those modelling studies involving insights into calcium instabilities.

The SERCA pump has been experimentally shown [72, 73] to play a key role in the formation of calcium alternans. As such it has been a key focus of modelling studies. Multiple studies have shown that a decrease in the pump strength promotes alternans [8, 11]. However studies by Nivala and Qu [9] and Huertas *et al* [12] revealed that a further decrease in the strength of the SERCA pump would eventually suppress alternans. Nivala and Qu suggested a continuing decrease in uptake strength would eventually lead to a low enough reduction in spark recruitment to suppress alternans.

As important as the SERCA pump has been deemed in the formation of calcium alternans, so has the release of Ca^{2+} from the SR. In a modelling study Shiferaw and Karma [11] revealed that a steeper release for high SR load could promote alternans as well as more chaotic behaviours. The idea of steeper release stems from the fact that Ca^{2+} from the SR is not linearly proportional to the Ca^{2+} concentration in the SR but lies on a curve with increasing gradient. By steeper release we are referring to the idea of increasing the gradient of this curve even more for higher SR Ca^{2+} concentrations. Xie *et al* [8] also drew such conclusions from their analysis of an iterated map parameter from a different representation of the SR release slope. As well as the strength of the SR release, modelling studies have looked at the sensitivity of Ryanodine receptors (RyRs). Nivala and Qu found that a reduced sensitivity could promote both alternans and other irregular patterns of free intracellular Ca^{2+}.

Since steeper release has been linked with the promotion of alternans, studies have also looked at the effects of overloading the SR. Such overloading has not only been studied as a direct promoter of alternans but also as a possible cause of alternan precursors such as calcium waves and spontaneous calcium release (SCR). One such study by Shiferaw [74] illustrated that calcium waves could promote alternans in myocytes that have had a large reduction in the number of

CRUs containing L-type Ca^{2+} channels.

This relationship between the SR load, SERCA pump activity and SR release has been shown experimentally as one of the main ways in which the calcium dynamics can produce alternans [75, 76]. Theoretical studies have represented this relationship as a pair of iterated maps, relating the onset of alternans to a bifurcation [77, 78]. However, it has been shown this cannot be the only cause of calcium alternans [79].

Another major mechanism proposed to cause alternans is linked to the role of ryanodine receptor refractoriness, which is caused by a slow recovery of the ryanodine receptors from inactivation [80]. Whilst modelling studies focusing on the SERCA pumps and the size of SR release date back over the last few decades, studies into the role of the ryanodine receptor refractoriness is still in its infancy. One of the most popular models used for the gating dynamics of the ryanodine receptors is the four state model developed by Stern *et al* [81]. This has meant most studies into the role of ryanodine receptor refractoriness have mostly been numerical based [82]. However, a simplified model by Cantalapiedra *et al* [83], has allowed for some analytical bifurcation theory and thus given them the ability to reveal that as well as slow recovery from inactivation, alternans can also be promoted by fast recovery for slower pacing periods.

Whilst the SERCA pump and SR release are often the most considered part of the calcium cycle when studying calcium alternans, other parts of the myocyte have been shown to have a role too. As the two major routes that control flow of calcium across the membrane of the myocyte, the NCX and L-type Ca^{2+} channel have also been studied through mathematical models.

The role of the L-type Ca^{2+} channel in calcium alternans has been considered due to its importance in CICR. The 2003 model by Shiferaw and Karma [11] suggested, through numerical simulations, that a steeper calcium dependence on the calcium-induced inactivation of the L-type Ca^{2+} channel could both increase the length of each pacing period at which the onset of alternans would occur and the amplitude of such alternans. Biologically, this implies that alternans are more likely when the rate at which that L-type Ca^{2+} channel goes from fully open to fully closed is increased. Furthermore, it was clear this was a calcium driven

instability as the model used a clamped voltage.

From a spatial point of view, a modelling study by Tao *et al* [84], revealed that blocking of L-type Ca^{2+} channels within parts of the myocyte can help promote alternans by causing a delay in the release of Ca^{2+} from the SR within some CRUs. However, this initiation in alternans may not be solely due to the loss of L-Type Ca^{2+} channels but more likely an interruption in the overall CICR process.

Although these studies demonstrated a possible role for the L-type Ca^{2+} channel to promote or suppress alternans under some conditions, it appears to have no role in most conditions. The modelling study by Livshitz and Rudy [64] revealed that both calcium and APD alternans could persist when the L-Type Ca^{2+} Channel is clamped. Similar behaviour has been observed experimentally [2, 85]. This suggests that, despite its importance in CICR, the L-Type Ca^{2+} channel's role in alternans may be limited compared to that of other channels within the myocyte.

Experimental studies based on the NCX links to instabilities within the myocyte have tended to focus on its role in the action potential [86]. However, some mathematical studies have considered the NCX in terms of the calcium dynamics. Nivala and Qu's study [9] of the NCX role in alternans focused on increasing the strength of the NCX. By doing this, they showed that an increased NCX strength could suppress alternans due to its effects on SR Ca^{2+} load and the probability of a spark recruiting neighbouring CRUs. Similar results were obtained by Huertas *et al* [12]. They also revealed that large decreases in the strength of the NCX could suppress alternans, as well.

Along with the major calcium currents, two other parts of the calcium cycle have been shown to have a role in calcium alternans. These are the buffers and diffusion of Ca^{2+} across the myocyte. Buffers are proteins within the cell that bind to Ca^{2+} to help regulate the level of free calcium ions within each part of the cell. For example, when Ca^{2+} is released into the cytoplasm, most of it will then bind to buffers to prevent an excessive change in the free intracellular calcium levels. Whilst studies on the role of buffers have become more common, the role of diffusion has been less looked at.

In 2008 Restrepo *et al* [13] developed a model that incorporated the effects of the luminal buffer Calsequestrin (CSQN) on RyR channels. Using numerical simulations they revealed that an increase in either the concentration of CSQN or CSQN unbinding time can promote alternans. These findings were researched further by Alvarez-Lacalle *et al* [87] who, using the Shannon model [46], illustrated that the luminal buffer had a larger effect on alternans linked to fluctuations in SR calcium loading, compared to those linked with a slow recovery from RyR inactivation. The Shannon model differs from the Restrepo model in its approach to the CSQN concentration by not treating it as a constant but as a variable. Since this is more biologically realistic, it provides stronger backing to the possibility of CSQN promoted alternans in nature. Nivala *et al* [9] focused on the effect of the SR buffer within the cytosol, finding that reduced buffering would promote alternans by increasing the probability of spark recruitment in neighbouring CRUs.

In ODE models intracellular diffusion is predominantly modelled by a linear term linking neighbouring sarcomeres through the SR and cytosol in an approach known as diffusive coupling. This approach would include a parameter to describe the coupling strength between the sarcomeres. This coupling strength would be deemed to represent the rate of diffusion between sarcomeres. The first model to note that increased strength in intracellular diffusive coupling would lead to subcellular alternans, is the 2008 model by Restrepo *et al* [13]. Restrepo *et al* suggests that diffusive coupling cause these alternans by synchronising the firing of CRUs Ca^{2+} release alternans. Huertas *et al* [12] revealed that increases in the rate at which Ca^{2+} transfers from the non-junctional SR to the JSR could promote period-two alternans and even period-four patterns.

As well as the diffusion strength, studies have considered the role of diffusion in synchronising local alternating events into a global pattern. These models focus on the stochastic dynamics that can cause such local release events. The results of such synchronisation have meant that alternans have been linked to an order-disorder phase transition by Alvarez-Lacalle *et al* [88]. Alvarez-Lacalle *et al* revealed that alternating sparking within single CRUs could translate to Ca^{2+} alternans due to the short range Ca^{2+} diffusion between neighbouring CRUs. At

fast enough pacing the calcium diffusion would cause the neighbouring CRUs to synchronise with this alternating pattern. Eventually large regions of the myocyte would synchronise causing calcium alternans. Such behaviour can be described in the same way as order-disorder transitions seen in models of the universality Ising class.

The majority of these findings were made via simulations or performing bifurcation theory on 1D or 2D maps. Whilst experimental findings often reveal similar findings since these maps are made by largely reducing the system phenomenologically, direct comparisons can be lost due to the combining of parameters. The 3R theory [9, 89, 90] is one of the the theories that has stemmed from these map approaches, which sought to understand how all these possible causes of alternans relate to one another. The 3Rs refer to randomness of Ca^{2+} sparks, recruitment of Ca^{2+} sparks by its neighbouring CRUs and refractoriness of the CRUs. This theory uses an iterated map in which the 3Rs are each represented as variables. This is the approach Nivala *et al* [9] used to make their findings. One disadvantage of the original 3R theory [89] is that it ignores the balance between the SERCA pump, SR load and SR release as a possible avenue for calcium alternans. This disadvantage was rectified by Qu *et al* [10] through the introduction of a iterated map for this relationship. The advantage of the updated 3R theory is that it allows one to see which parts of the myocyte can alter either one of the 3Rs or the balance between the SR currents. The main disadvantage is that as the system is now represented as a set of iterated maps some aspects of the system may be lost. This includes the ability to study spatially discordant alternans and the role of some parameters deemed to have a possible role in alternans such as the spark duration.

As well as calcium alternans, other calcium instabilities have been shown to occur within the myocyte but studies on these behaviours are limited. One study that does go more into depth is that by Bien *et al* [91]. Within their study Bien *et al* considered the possibility of quasiperiodicity and intermittency using both an experimental and modelling approach. Within this study they demonstrated that both these forms of instabilities could be linked with VF-like episodes. Furthermore, they demonstrated that these different instabilities could coexist

within tissue. Such coexisting of differing behaviours linked to varying calcium instabilities was also reported by Skardal and Restrepo [92] who demonstrated that chaos could stem from varying period-doubling cascades within a network of myocytes.

2.2.3 Role Of Bidirectional Coupling

As well as looking at individual parts of the myocyte to understand their role in alternans, some models have considered the effect of the bidirectional coupling itself. Shiferaw *et al* [93] took the Shiferaw-Karma model, combining it with the voltage dynamics of the Fox model [59] (Shiferaw-Fox model), to reveal how SCA would form due to positive calcium to voltage coupling whilst SDA would form due to negative calcium to voltage coupling. Shiferaw and Karma extended their study in 2006 [94]. First, they reduced the Shiferaw-Fox model down to a 2D iterative map to describe the beat-to-beat dynamics in each sarcomere for the APD and peak Ca^{2+} transient. Then, by integrating these maps across the length of the myocyte and assuming that the voltage equilibrates rapidly, they were able to create two partial differential equations to describe the amplitude in the APD and Ca^{2+} alternans close to the onset. By perturbing around the point of zero amplitude in the alternans they were able to derive conditions under which alternans could appear from the Jacobian of the system. Further to this, they used these conditions to show that SDA could form from a homogenous system via a Turing instability. The same approach was used by Restrepo *et al* [95] to confirm the formation of SDA can be due to a Turing stability linked to negative coupling between the calcium and voltage dynamics but that it is also possible with positive coupling.

Shiferaw and Karma's research was then taken a step further by Gaeta *et al* [96]. By using a protocol developed by Li and Otani [97] to study the stability of the system, Gaeta *et al* gave further backing to Shiferaw and Karma's theory but additionally found that the calcium dynamics must be more unstable than those of the voltage. By more unstable, Gaeta *et al* mean that when the voltage was clamped, the calcium dynamics would give an eigenvalue lying further into the region of instability than the voltage dynamics gave when the calcium pattern

was clamped.

Work by Groenendaal *et al* [98], suggested that the effect of the voltage's stability on the appearance of subcellular alternans may be negligible but that unstable calcium dynamics are essential. Unstable calcium dynamics were deemed essential as stable calcium dynamics could limit alternans formed by the voltage dynamics. On the other hand, the voltage dynamics would have little effect on the calcium dynamics. Thus any instabilities in the calcium dynamics would enforce subcellular alternans. In a similar vein, a study by Cherry [99] focused on a way to differentiate the driver of alternans in systems with bidirectional coupling. By using a constant DI within the pacing regime, Cherry revealed that when a constant DI is present, calcium must be the driver of alternans within the Mahajan model [62]. Cherry suggested such a protocol may be used for other models with both voltage and calcium dynamics to discern the critical driving force for instabilities.

As well as the role bidirectional coupling plays in alternans, its effect has been considered in terms of instabilities normally associated solely with the voltage dynamics. One particular study by Song *et al* [100] revealed how calcium can play an important role in the modulation of early afterdepolarizations (EADs) and delayed afterdepolarizations (DADs). These are unwanted voltage patterns linked to multiple pathological conditions.

These studies illustrate the importance of the calcium dynamics at both a subcellular and cellular level. Due to the bidirectional coupling between calcium and the voltage, an instability within the calcium dynamics could have a severe effect on the voltage dynamics. This, as discussed in Section 2.2.1, could then have an effect on the calcium dynamics elsewhere within the heart and, through a knock-on effect, produce conditions such as ventricular arrythmia.

2.3 The Piecewise Linear Shiferaw-Karma Model

Within this thesis we will be using a version of the Shiferaw-Karma model [11] adapted by Thul and Coombes to be PWL [1]. The PWL model was developed in such a way to maintain the quantitative behaviour of the original Shiferaw-Karma model whilst opening the door to a direct approach for stability analysis.

Periodic orbits produced by the PWL model can be described using a series of switching events. The term switching events refers to a point in the periodic orbit where the form of one of the functions within the model changes. By describing the periodic orbit as a sequence switching events we are able to use an approach towards the stability analysis which does not require the reduced maps discussed in Section 2.2.2. We will discuss this approach in more depth in Section 2.4. The following is an introduction to the PWL Shiferaw-Karma model.

The PWL Shiferaw-Karma model consists of the five ODEs as opposed to the Shiferaw-Karma model which contains nine ODEs. The full Shiferaw-Karma model can be found in Appendix D whilst the PWL Shiferaw-Karma model is;

$$\begin{aligned}
\frac{\mathrm{d}c_\mathrm{s}}{\mathrm{d}t} &= \beta_s \left[\frac{v_\mathrm{i}}{v_\mathrm{s}} \left(I_\mathrm{r} - \frac{c_\mathrm{s} - c_\mathrm{i}}{\tau_\mathrm{s}} - I_\mathrm{CaL} \right) + I_\mathrm{NaCa} \right], \\
\frac{\mathrm{d}c_\mathrm{i}}{\mathrm{d}t} &= \beta_i \left[\frac{c_\mathrm{s} - c_\mathrm{i}}{\tau_\mathrm{s}} - I_\mathrm{up} \right], \\
\frac{\mathrm{d}c_\mathrm{j}}{\mathrm{d}t} &= -I_\mathrm{r} + I_\mathrm{up}, \\
\frac{\mathrm{d}c'_\mathrm{j}}{\mathrm{d}t} &= \frac{c_\mathrm{j} - c'_\mathrm{j}}{\tau_\mathrm{a}}, \\
\frac{\mathrm{d}I_\mathrm{r}}{\mathrm{d}t} &= -gI_\mathrm{CaL} Q\left(c'_\mathrm{j}\right) - \frac{I_\mathrm{r}}{\tau_\mathrm{r}}.
\end{aligned} \tag{2.1}$$

The variables are $\mathrm{c_s}$ (subsarcolemmal Ca^{2+} concentration), $\mathrm{c_i}$ (cytosolic Ca^{2+} concentration), $\mathrm{c_j}$ (total SR Ca^{2+} concentration), $\mathrm{c'_j}$ (unrecruited JSR Ca^{2+} concentration) and $\mathrm{I_r}$ (the release current from the SR into the cytosol).

The parameters β_s and β_i represent calcium buffering in the subsarcolemmal space and bulk cytosol respectively. Other parameters that can be seen in equations (2.1) are the subsarcolemmal/cell volume ($v_\mathrm{s}/v_\mathrm{i}$) and the release current strength (g). Also included are the submembrane diffusion time constant (τ_s), the relaxation time of c'_j to c_j (τ_a) and the average spark life time (τ_r). Currents included in equations (2.1) are the L-type Ca^{2+} channel (I_CaL), the NCX (I_NaCa) and the SERCA pump (I_up).

The L-type Ca^{2+} channel is a heaviside like function of the form $I_\mathrm{CaL} = \Theta(V - V_\mathrm{L}) i_\mathrm{CaL}$, where Θ represents the heaviside function, V_L is the voltage value at which the L-type Ca^{2+} channel stops releasing calcium and i_CaL is the constant conductance. The SERCA pump is represented by the linear equation $I_\mathrm{up} = v_\mathrm{up} c_\mathrm{i}$,

where v_{up} is the uptake strength of the SERCA pump. The NCX function takes the form; $I_{\text{NaCa}} = \phi(V) - \psi(V)c_{\text{s}}$ where $\phi(V)$ is a continuous function dependent on the voltage and $\psi(V)$ is a piecewise constant function controlled by the voltage. For a more in depth description of these functions, see Appendix C.

The PWL function $Q\left(\mathrm{c_j'}\right)$ represents the load-release from the SR to the cytosol and takes the form

$$Q\left(\mathrm{c_j'}\right) = 10^{-3}\begin{cases} 0, & 0 \leq \mathrm{c_j'} < 50 \\ \mathrm{c_j'} - 50, & 50 \leq \mathrm{c_j'} < 115 \\ u\mathrm{c_j'} + s, & \mathrm{c_j'} \geq 115 \end{cases} . \tag{2.2}$$

The parameters are the release slope of Ca^{2+} from the SR to the cytosol (u) and the constant chosen to make Q continuous (s). Equation 2.2 provides an example of a function that can change due to a switching event since the form of Q is dependent upon the value of $\mathrm{c_j'}$. For example when the orbit of the system passes through the point $\mathrm{c_j'} = 115$, the form of Q alters. It is at this point that a switching event occurs. Within this thesis we shall take a close look at the effect on the calcium dynamics that the parameters v_{up} and u have.

Due to the PWL nature of this model, we are able to rewrite the system in equations (2.1) as

$$\dot{x} = Mx + f\left(t\right), \tag{2.3}$$

where x is a vector containing the five variables in equation (2.1). The matrix $M \in \mathbb{R}^{5\times5}$ is a matrix of constants, whilst $f \in \mathbb{R}^5$ is a time dependent vector. We can do this as the values of the constants contained in M only change when we pass through a switch in the system. By switch we refer to the crossing of a value in either the voltage or the unrecruited JSR Ca^{2+} concentration that alters the shape of one of the piecewise functions contained within the model.

As well as studying a single myocyte, the model can be extended to a subcellular network of sarcomeres via the methods discussed in Section 2.1.2. To extend this system to a subcellular network of sarcomeres we add the term $\sum_{\zeta\in cc}(\mathrm{c_i}^{\zeta} - \mathrm{c_i}^{\mu})/\tau_{\text{c}}$ to the dynamics for the cytosolic Ca^{2+} concentration and the term $\sum_{\zeta\in cc}(\mathrm{c_j}^{\zeta} - \mathrm{c_j}^{\mu})/\tau_{\text{sr}}$ to the dynamics of the total SR Ca^{2+} concentration.

These terms represent diffusive coupling between subcellular sarcomeres, where μ is the sarcomere that the dynamics are related to and $\zeta \in cc$ are the sarcomeres connected to sarcomere μ. The parameters τ_{c} (for cytosolic coupling) and τ_{sr} (for SR coupling) represent the coupling strength. This transforms equations (2.1) for a single sarcomere μ contained within a network to;

$$\begin{aligned}
\frac{\mathrm{d}c_{\mathrm{s}}^{\mu}}{\mathrm{d}t} &= \beta_s \left[\frac{v_{\mathrm{i}}}{v_{\mathrm{s}}} \left(I_{\mathrm{r}}^{\mu} - \frac{c_{\mathrm{s}}^{\mu} - c_{\mathrm{i}}^{\mu}}{\tau_{\mathrm{s}}} - I_{\mathrm{CaL}} \right) + I_{\mathrm{NaCa}}^{\mu} \right], \\
\frac{\mathrm{d}c_{\mathrm{i}}^{\mu}}{\mathrm{d}t} &= \beta_i \left[\frac{c_{\mathrm{s}}^{\mu} - c_{\mathrm{i}}^{\mu}}{\tau_{\mathrm{s}}} - I_{\mathrm{up}}^{\mu} \right] + \sum_{\zeta \in cc} (\mathrm{c_i}^{\zeta} - \mathrm{c_i}^{\mu})/\tau_{\mathrm{c}}, \\
\frac{\mathrm{d}c_{\mathrm{j}}^{\mu}}{\mathrm{d}t} &= -I_{\mathrm{r}}^{\mu} + I_{\mathrm{up}}^{\mu} + \sum_{\zeta \in cc} (\mathrm{c_j}^{\zeta} - \mathrm{c_j}^{\mu})/\tau_{\mathrm{sr}}, \\
\frac{\mathrm{d}c_{\mathrm{j}}'^{\mu}}{\mathrm{d}t} &= \frac{c_{\mathrm{j}}^{\mu} - c_{\mathrm{j}}'^{\mu}}{\tau_{\mathrm{a}}}, \\
\frac{\mathrm{d}I_{\mathrm{r}}^{\mu}}{\mathrm{d}t} &= -g I_{\mathrm{CaL}} Q\left(c_{\mathrm{j}}'^{\mu}\right) - \frac{I_{\mathrm{r}}^{\mu}}{\tau_{\mathrm{r}}}.
\end{aligned} \tag{2.4}$$

In equations (2.4) the currents I_{NaCa} and I_{up} are now dependent on calcium concentrations contained in sarcomere μ. On the other hand, since I_{CaL} is the only current purely dependent on the voltage it takes the same value across all sarcomeres. The nearest neighbour coupling used in this thesis is based on the fact we treat individual sarcomeres as nodes and thus effectively discretize the myocyte. This means that we no longer have need to model intracellular diffusion using Fick's 2$^{\mathrm{nd}}$ law of diffusion. Instead we use the linear terms previously mentioned, these terms are effectively discretized versions of Fick's 2$^{\mathrm{nd}}$ law in which the coupling parameter crudely represents the average time for Ca^{2+} to diffuse across the average distance between the centre of two sarcomeres. One note to make is that the size of sarcomeres do not tend to vary much within healthy myocytes and thus standardising the distance between them is not unjustified.

Although coupling between cells can occur through gap junctions, it is not yet clear whether Ca^{2+} itself is passed between cells or just the signalling molecule IP_3. Hence, any conclusions we draw from studies on networks purely coupled by the cytosol can be applied to cellular networks as long as we consider this proviso. The parameters τ_{c} and τ_{sr} are of interest when studying the effects of coupling on the stability of a synchronous state within the network. To account for the

effects of cytosolic buffering we can simply scale the coupling parameter τ_c by the buffering constant β_i. We will see how the coupling can be incorporated into the model when written in the form shown in equation (2.3) in Section 2.4.

The advantages of this model come from the fact that this set up allows us to find critical values for parameters of interest through linear stability analysis. The way we approach this analysis is explained in Section 2.4.

2.4 Approach To Linear Stability Analysis

One of the key advantages of the PWL model revolves around the techniques we can use to study its stability. Here, we will provide a brief overview of these techniques, whilst a more in depth look of these techniques can be found in the paper by Thul and Coombes [1]. Using some of the notation discussed in the previous section, we are able to describe the dynamics of an individual sarcomere within a network between the z and $(z+1)$th switching events as,

$$\dot{x}_z^\mu = [M_z x_z^\mu + f_z]\,\Theta\left(t - T_z^\mu\right)\Theta\left(T_{z+1}^\mu - t\right) + \sum_{k,\alpha} G_{\mu\alpha} H x_k^\alpha \Theta\left(t - T_k^\alpha\right)\Theta\left(T_{k+1}^\alpha - t\right). \quad (2.5)$$

Within equation (2.5) x is a vector containing the five variables related to sarcomere μ and the constant T_z^μ is the time at which a switching event occurs within that sarcomere. The matrix $M \in \mathbb{R}^{5\times5}$ is a matrix of constants, whilst $f \in \mathbb{R}^5$ is a time dependent vector and Θ represents the heaviside function. The matrix G describes the topology of the network and has eigenvalues λ_ν with eigenvectors contained in the matrix L. The matrix H describes the components of x that the coupling occurs through, and contains the coupling parameters. The summation is performed over switching points k and sarcomeres α.

In Figure 2.7, we see a plot of the unrecruited JSR Ca^{2+} concentration from a simulation of the system at a slow pacing period ($T_p = 0.9\ s$). Superimposed on the plot are the switching events that can occur in a single period. The order of the switching events shown here are what we would expect, but other orders can occur dependent on parameter values. We will look at what the change in order for switching events mean for our model in Section 3.2.1.

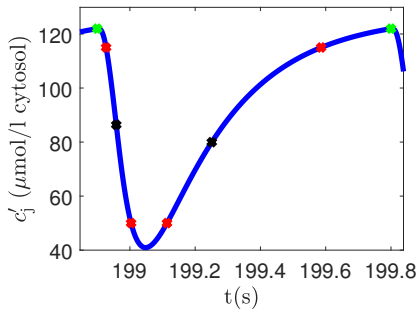

Figure 2.7: Plot of the unrecruited JSR Ca^{2+} concentration from a simulation of the system with pacing period $T_p = 0.9$ s. The green stars represent the start and end of a single pacing period. The red stars represent a switch in the load-release function. The black stars each represent a voltage dependent switch. All other parameters as in Appendix A.

The green stars in Figure 2.7 represent the start of a pacing period within the system. At this point the clamped voltage immediately depolarises to its maximal value. The red stars each represent a switch in the load-release function whilst the black stars represent the two voltage dependent piecewise currents. The first black star represents the switch in I_{CaL} whilst the second is the switch in I_{NaCa}. As we cross these switches, the form of the matrix M and/or time dependent vector f changes.

When the orbit produced by equation (2.5) is identical for all sarcomeres, the network is deemed to have a stable synchronous orbit. The synchronous state, which we denote as s will have the same orbit as the uncoupled state since coupling terms cancel out. Thus to find the synchronous state we refer to equation (2.3), subbing s in for x. By integrating this equation between switching times we can then relate the value of x at switching time $z+1$ to the value of x at switching time z as

$$s_{z+1} = e^{M_z(T_{z+1}-T_z)}s + \int_{T_z}^{T_{z+1}} e^{M_z(T_{z+1}-t)}f(t)\mathrm{d}t. \tag{2.6}$$

To build the orbit we set $T_0 = 0$ and $T_{m+1} = T_p$ where $m+1$ is the total number of switching events. We then solve equation (2.6) at each switching point z consecutively starting with $z = 0$ to find $z = 1$. For switching points in which the switching time is unknown but the value of one of the elements of s_{i+1} at the switch point is known, for example when a switching event related to the load-release function occurs, equation (2.6) must first be solved for the unknown

time with that value.

To help explain this more clearly we shall look at the McKean model [101] of the form

$$\begin{aligned} \frac{\mathrm{d}v}{\mathrm{d}t} &= p\left(v\right) - w + I\left(t\right) \\ \frac{\mathrm{d}w}{\mathrm{d}t} &= 0.6\left(v - 0.2w\right), \end{aligned} \tag{2.7}$$

where

$$p\left(v\right) = -v + \Theta\left(v - 0.25\right). \tag{2.8}$$

The model has variables v and w and the function Θ is the heaviside function. The time dependent function $I(t)$ provides an input current of value 0.6 for a duration of 0.001s to the system at the beginning of each pacing period. The pacing period for this example is $T_p = 1$s. To begin with we consider the system as a sting of switching events and thus rewrite the dynamics as

$$\dot{s}_z = \begin{pmatrix} \dot{v}_z \\ \dot{w}_z \end{pmatrix} = \left[M_z s_z + f_z\right] \Theta\left(t - T_z\right) \Theta\left(T_{z+1} - t\right). \tag{2.9}$$

In equation (2.9), M, f, Θ, z and T take the same definitions as in equation (2.6).

From simulations we know that the periodic orbit has four switching events. The first and third relate to the activation and deactivation of the heaviside function in p and thus are dependent on the value of v. Since these switches depend on v we do not know the time that they take place. The second and fourth relate to the inactivation and activation of the time dependent input current I respectively. The timing of these switches are known as I is purely time dependent. For example the dynamics between $z = 0$ and $z = 1$ can be written in the form of equation (eq:McKean Switch Dynamics Equation) with $z = 0$,

$$M_0 = \begin{pmatrix} -1 & -1 \\ 0.6 & 0.12 \end{pmatrix}, \tag{2.10}$$

and

$$f_0 = \begin{pmatrix} 0.6 \\ 0 \end{pmatrix}. \tag{2.11}$$

It is the equations like equation (2.10) that we integrate between the two consecutive switching times to relate s_z to s_{z+1}. This then allows us to progress through switching events to produce the periodic orbit of the system.

To build the orbit we begin with $s_0 = \binom{0}{0}$ and solve

$$s_1 = e^{M_0(T_1)}s_0 + \int_0^{T_1} e^{M_0(T_1-t)}f(t)\mathrm{d}t, \tag{2.12}$$

for the element in s_1 equal to 0.25, to find the value of T_1. We then use the value of T_1 to find the the unknown element in s_1. Having done this we then find s_2 which is simpler since we know $T_2 = 0.001$ as this switching event relates to the deactivation of the input current I. We then repeat the process for s_3 and $s_4 = s_{m+1}$. Although in this example we know that $s_0 = \binom{0}{0}$ and thus $s_4 = \binom{0}{0}$, in general to find periodic orbits, we set up system using the family of equations described by equation (2.6) and then solve it to find the value of s_0 such that $s_0 = s_{m+1}$.

The approach discussed above provide an alternative to the approaches used in of programs such as XPP or MATCONT. Such programs are similar to our approach in that they require a reasonable initial guess which is usually taken from a simulation. However, the approaches used by program such as XPP and MATCONT struggle to produce the periodic orbits of systems which contain functions with step like behaviour, such as the function we use in the PWL Shiferaw-Karma model to represent the voltage clamp. Our approach is advantageous in this sense as such discontinuities are used to split up the orbit and thus allows to circumnavigate them. The disadvantage of our approach is that it requires knowing the ordering of switching events and when changing parameter values for continuation such an order can change. This means that our approach to continuation required the ability to cycle through different switching event orders. To increase efficiency of continuation this meant performing simulations at multiple parameter values to understand how switching event orders can change. This then allowed us to implement a hierarchy of switching event orders to cycle through when using our approach to perform continuation. However, in systems with far more switching events this could become computationally slow due to the number of simulations needed to derive such a hierarchy. In this case it may be more advantageous to

find an approximation to system discontinuities such that programs such XPP can be used.

To study whether a period orbit is a stable synchronous state, each sarcomere is perturbed by $\delta x_z^\mu \in \Re$. By taking this perturbation of the synchronous orbit and using techniques developed by Pecora and Carroll [102], along with defining new vector variables $\delta y_z^\nu = \sum_\mu L_{\nu\mu}^{-1} \delta x_z^\mu$ and $\delta U_z^\nu = \sum_\mu L_{\nu\mu}^{-1} \delta T_z^\mu$, we are able to link the perturbations of the new variable at the $(z+1)$th switching event to the zth switching event. The equation

$$\delta y_{z+1}^\nu = e^{R_z^\nu (T_{z+1} - T_z)} \left[\delta y_z^\nu - p_z^\nu \delta U_z^\nu \right] + q_{z+1}^\nu \delta U_{z+1}^\nu, \tag{2.13}$$

shows provides the link between these perturbations. We achieve this by differentiating and linearising equation (2.5) around the synchronous orbit. The synchronous orbit is the orbit such that $\dot{x}_z^\mu = \dot{s}_z$ for all μ whilst ν is the new term used to specify which of the new variables y we are focused on. We then introduce our new variables to the differentiated form of equation (2.5) and integrate between $T_z + \delta U_z^\nu$ and $T_{z+1} + \delta U_{z+1}^\nu$. This results in equation (2.13).

In equation (2.13) $R_z^\nu = M_z + \lambda_\nu H$, $p_z^\nu = \dot{s}\left(T_z^+\right) + \lambda_\nu H s_z$ and $q_z^\nu = \dot{s}\left(T_z^-\right) + \lambda_\nu H s_z$. The positive and negative superscript symbols for T represent whether we are looking at the synchronised state before $(-)$ or after $(+)$ a switching event. By using the relationship given in equation (2.13) and using this to go from one switching event to the next, we eventually arrive at matrices S_m^ν such that $\delta y_{m+1}^\nu = S_m^\nu \delta y_0^\nu$, where $m+1$ marks the final switching event in the synchronised state.

To study the stability of the synchronous orbit we compute the eigenvalues σ_i^ν of the matrix S_m^ν for all ν. The orbit is deemed stable if for all ν and i, $|\sigma_i^\nu| < 1$, as the method is similar to that used for studying the stability of maps. We are concerned with the bifurcation point at which the orbit becomes unstable, this occurs when one $|\sigma_i^\nu| = 1$ whilst the rest still lie within the unit circle.

The advantage of this approach is that it captures the stability of the single cell case. This means that the stability of the network is partly dependent on the stability of the uncoupled dynamics. It is also worth stating that by dropping the coupling terms in equation (2.5), the same approach to the stability analysis can

be used to study the single cell case. In terms of synchronous states this means we only need to find the orbit of the uncoupled case, since the synchronous state matches the uncoupled orbit, and thus, unlike other continuation programs we do not need to input the dynamics for the whole network. We can simply find the uncoupled orbit first and then determine the effect of the coupling parameter on such an orbit.

Much like with the approach to building the periodic orbit of the synchronous state, we shall now use two coupled McKean systems to provide further explanation of how the stability approach works. The McKean systems shall be coupled by adding the coupling term $(w^2 - w^1)/\tau_w$ to the dynamics of w in the first McKean system and the term $(w^1 - w^2)/\tau_w$ to the dynamics of w in the second McKean system. The indices in these coupling terms refer to which system the variable w comes from, τ_w is a coupling parameter and the uncoupled dynamics are the same as those in equation (2.7).

Now to study the periodic orbit of our McKean system we first need to perturb equation (2.5 around the synchronised state s. This leads to the equation

$$\begin{aligned}\frac{\mathrm{d}}{\mathrm{d}t}\delta x_z^\mu = M_z \delta x_z^\mu \Theta\left(t - T_z\right)\Theta\left(T_{z+1} - t\right) \\ + \dot{s}\left[\delta T_{z+1}^\mu \theta\left(T_{z+1} - t\right) - \delta T_z^\mu \theta\left(t - T_z\right)\right] \\ + \sum_{k,\alpha} G_{k\alpha} H \left\{\delta x_k^\alpha \Theta\left(t - T_k\right)\Theta\left(T_{k+1} - t\right)\right. \\ \left. + s_k\left[\delta T_{k+1}^\alpha \theta\left(T_{z+1} - t\right) - \delta T_k^\alpha \theta\left(t - T_z\right)\right]\right\}. \quad (2.14)\end{aligned}$$

For the two coupled McKean systems, $\delta x = \begin{smallmatrix}\delta v \\ \delta w\end{smallmatrix}$, the connectivity matrix is $\left(\begin{smallmatrix}-1 & 1 \\ 1 & -1\end{smallmatrix}\right)$ whilst H has form $\left(\begin{smallmatrix}0 & 0 \\ 0 & \frac{1}{\tau_w}\end{smallmatrix}\right)$ to describe which compenents the two systems are linked through and at what coupling strength. To prevent confusion the dirac delta function is notified by θ as opposed to the traditionally used δ since δ is already being used. All other notation is still defined as previously. We note μ is equal to one or two in this case since our network only contains two McKean systems. Since the network connections can be described by one connectivity matrix G and accompanying matrix H, it is advantageous to use the master stability approach developed by Pecora and Carroll [102] to transform the equation. Such an

approach greatly improves computational efficiency and accuracy as it allows us to effectively decouple the network by using the eigenvalues of the connectivity matrix.

To do this we first find the matrix L which contains the eigenvectors of G and its inverse L^{-1}. We then multiply through equation (2.14) by L^{-1}. Then, by defining the two new variables $\delta y_z^1 = L_{1,1}^{-1}\delta x_z^1 + L_{1,2}^{-1}\delta x_z^2$ and $\delta y_z^2 = L_{2,1}^{-1}\delta x_z^1 + L_{2,2}^{-1}\delta x_z^2$ along with the new perturbed switching times $\delta U_z^1 = L_{11}^{-1}\delta T_z^1 + L_{12}^{-1}\delta T_z^2$ and $\delta U_z^2 = L_{21}^{-1}\delta T_z^1 + L_{22}^{-1}\delta T_z^2$, we rewrite the system as

$$\begin{aligned}\frac{\mathrm{d}}{\mathrm{d}t}\delta y_z^\nu = M_z\delta x_z^\nu\Theta\left(t-T_z\right)\Theta\left(T_{z+1}-t\right)\\ +\dot{s}\left[\delta U_{z+1}^\nu\theta\left(T_{z+1}-t\right)-\delta U_z^\nu\theta\left(t-T_z\right)\right]\\ +\lambda_\nu\sum_k H\left\{\delta y_k^\nu\Theta\left(t-T_k\right)\Theta\left(T_{k+1}-t\right)\right.\\ \left.+s_k\left[\delta U_{k+1}^\nu\theta\left(T_{z+1}-t\right)-\delta U_k^\nu\theta\left(t-T_z\right)\right]\right\}. \quad (2.15)\end{aligned}$$

This transformation now means that the network topology is encased in the eigenvalues λ of the connectivity matrix G. Then by integrating equation (2.15) between $T_z+\delta U_z^\nu$ and $T_{z+1}+\delta U_{z+1}^\nu$ we arrive at equation (2.13). It is this equation that we use to find the block diagonal matrix S_m whose eigenvalues inform us of the stability of the orbit. Furthermore, since S_m is block diagonal, we can find each block S_m^ν, where $\delta y_{m+1}^\nu = S_m^\nu\delta y_0^\nu$, and its eigenvalues individually. For example we shall find S_m^1 for our McKean network.

To begin with we need to find δy_1^1 using equation (2.15). First of all we note that $\delta U_0^1 = 0$ since T_0 and the time at which the pacing period starts is fixed and therefore does not perturb. This then leaves us with the equation

$$\delta y_1^1 = e^{R_0^1(T_1)}\delta y_0^1 + q_1^1\delta U_1^1. \quad (2.16)$$

Now the first switching event within the McKean model relates to when $v = 0.25$, this means that at the first switching event the value of v cannot have perturbed and therefore $[\delta y_1^1]_1 = 0$. Here the of the square brackets is to denote that we are referring to an element of δy_1^1 whilst the subscript denotes which element, in this

case the first, that we are referring to. Knowing this allows to write the equation

$$0 = \sum_{i=1}^{2} [e^{R_0^1(T_1)}]_{1,i} [\delta y_0^1]_i + [q_1^1]_1 \delta U_1^1, \tag{2.17}$$

which we can then rearrange to give

$$\delta U_1^1 = \sum_{i=1}^{2} [g_0^1]_i [\delta y_0^1]_i, \tag{2.18}$$

where $g_0^1 \in \mathbb{R}^2$ and $[g_0^1]_i = -[e^{R_0^1(T_1)}]_{1,i}/[q_1^1]_1$. Using this we can now rewrite the equation for δy_1^1 as

$$\delta y_1^1 = \left[e^{R_0^1(T_1)} + q_1^1 g_0^1 \right] \delta y_0^1. \tag{2.19}$$

Now by combining equation (2.19) with equation (2.13) we can then link δy_2^1 to δy_0^1. This in turn will allow us to link δy_3^1 to δy_0^1 and so forth eventually arriving at the equation $\delta y_{m+1}^1 = S_m^1 \delta y_0^1$. Cycling through all switching events in this is required as otherwise we are unable to consider the whole of the periodic orbit. We then repeat the process to find S_m^2. Once we have both matrices, we can then find the eigenvalues of S_m^1 and S_m^2 to inform us of the stability of the synchronous state s since the eigenvalues of the matrices S_m^ν will be the same as those of S_m. If any of the eigenvalues of these matrices lie outside the unit circle then we know that the synchronous state is unstable. It is this process that we have applied computationally throughout this thesis.

2.5 Previously Seen Behaviours

In this section, we will take a look at the behaviours previously seen in the PWL Shiferaw-Karma model. These behaviours include the single period orbit produced at slow pacing when modelling the myocyte as a single node. We then show how an increase in the pacing produces a period-double orbit.

Subsequently, we move from modelling the myocyte as a single node to a 1D network of sarcomeres, coupled purely through their bulk cytosolic components. By doing this we are able to reveal how under weak coupling and slow pacing the network follows a synchronised single-period orbit. Then we show that as we

increase the coupling this synchronised state loses stability, causing the system to produce spatial alternans.

2.5.1 Single Cell

Firstly, we show the results of two simulations of a single cell in Figures 2.8 and 2.9 at two different pacing periods. This illustrates that by decreasing the pacing period, the behaviour of the model can change. These figures reveal the trajectories for all five variables within the PWL Shiferaw-Karma model. In Figure 2.8, the length of time between each voltage depolarisation, which we shall call the pacing period (T_p) from now on, has been set to 0.9 s and the resulting trajectory of the system follows a stable single-period orbit. In terms of the biology that this model is grounded in, at a cellular level, this is the behaviour that we would expect of a healthy ventricular myocyte when the heart is beating with a consistent contraction strength.

On the other hand, in Figure 2.9 the results of the simulations reveal a stable period-doubled orbit. The only change to the model from that portrayed in Figure 2.8, has been a decrease in the the length of the pacing period from 0.9 s to 0.5 s. As we can see from Figure 2.9A and 2.9B, the peak cytosolic concentrations have different values for alternating beats but the same value for every two beats.

By performing the stability analysis described in Section 2.4, we have produced plots of the the eigenvalues (σ_i) for the single cell with $T_\mathrm{p} = 0.9$ s and $T_\mathrm{p} = 0.5$ s. These are presented in Figures 2.10A and 2.10B, respectively.

Comparisons of the eigenvalue plots in Figures 2.10A and 2.10B confirm the change of pacing period has caused one of the eigenvalues to pass out of the unit circle along the negative real axis. The other four eigenvalues still lie within the unit circle. One eigenvalue lies close to the +1 border of the unit circle, whilst the other three are grouped around zero. As we described in Section 2.4, this informs us that the single period orbit of the cell has gone from being stable to unstable. Furthermore, as this eigenvalue has passed out of the unit circle through -1, we know that the instability has occurred via a period-doubling bifurcation. Hence, our stability analysis supports the behaviour seen in Figures 2.8 and 2.9.

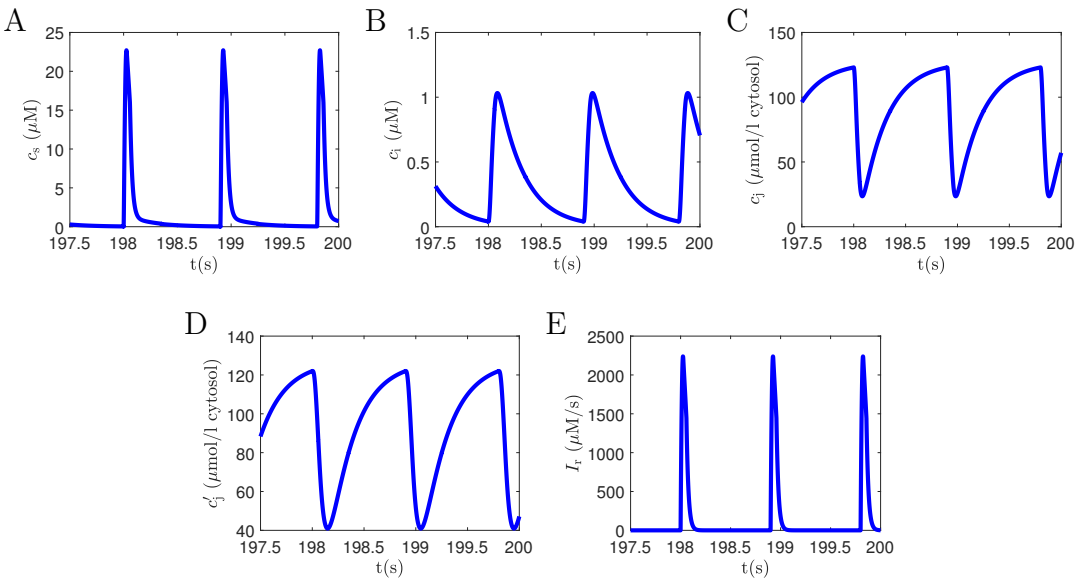

Figure 2.8: Trajectories of the five state variables for the single cell when a single period orbit is stable. $T_p = 0.9$ s and all other parameters are as in Appendix A.

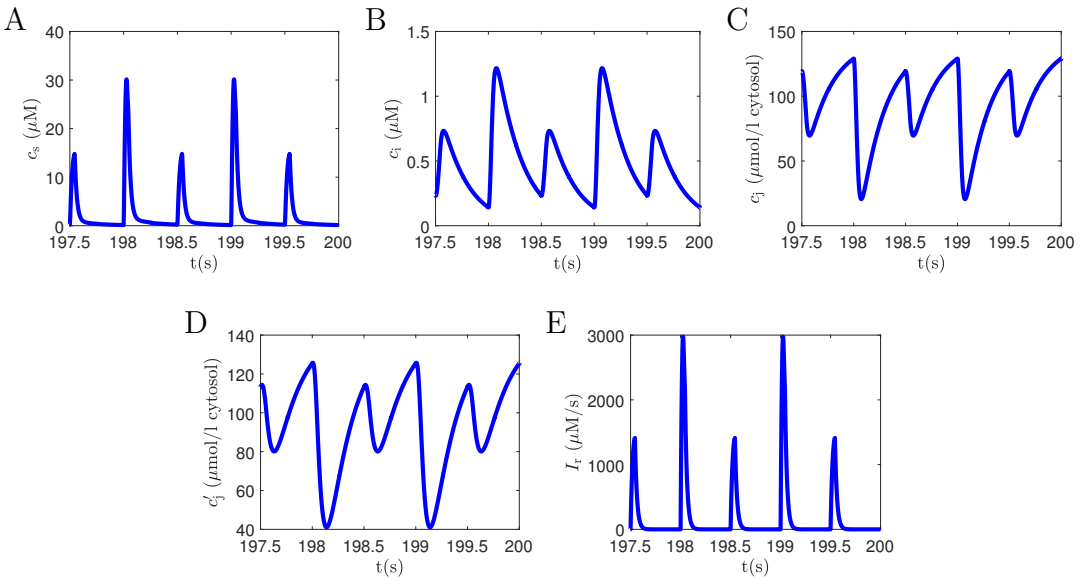

Figure 2.9: Trajectories of the five state variables for the single cell when the single period orbit has become unstable due to faster pacing. $T_p = 0.9$ s and all other parameters are as in Appendix A.

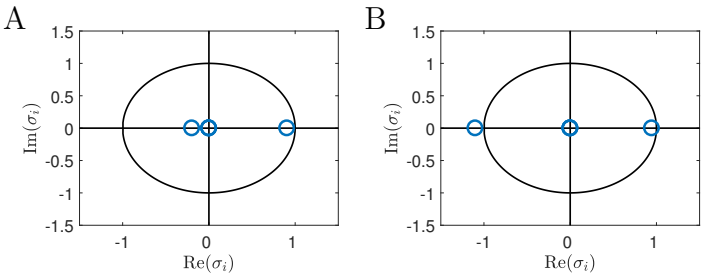

Figure 2.10: Eigenvalues for the systems studied in Figures 2.8 and 2.9. The pacing periods linked to the plots are $T_p = 0.9$ s (A) and $T_p = 0.5$ s (B). All other parameters as in Appendix A.

2.5.2 Cytosolic Coupling In An One-Dimensional Networks

Here, we perform two simulations of a network of sarcomeres, each under a different coupling strength, revealing the effect of increasing the strength of cytosolic coupling within the network. The first simulation demonstrates how the system behaves when the system is synchronised whilst the second simulation reveals what happens when this synchronisation is lost. The size of the network has been set to 75 sarcomeres. This is approximately the number of sarcomeres found in a single myofibril within a healthy human ventricular myocyte. The results of the two simulations can be seen in Figures 2.11 and 2.12. In Figures 2.11A and 2.11B, as well as Figure 2.12A and 2.12B, the solid blue plot and dashed red plot represent trajectories from two nearest neighbour sarcomeres within the network. This colour code will remain the standard for future trajectory plots derived from our simulations throughout this thesis.

Figure 2.11 portrays the system under synchronization, with each sarcomere following the same single period orbit. Furthermore, if we compare the trajectories in Figures 2.11A and 2.11B with those in Figures 2.8B and 2.8C, we find that they are, in fact, the same. This illustrates that the stable synchronised orbit of the network is the same as that of the stable single-period orbit of the uncoupled sarcomere. This is to be expected as, under synchronisation, the coupling terms cancel and thus the system equations become the same as those in the single cell case. In Figure 2.12 we find this this synchronous state has become unstable due to an increase in the coupling strength, represented by a decrease in the value of τ_c.

Figures 2.12A and 2.12B reveal how the sarcomeres within the network no longer follow a single-period orbit but, now, follow a period-doubled orbit. Moreover, we note that the two neighbouring sarcomeres described in Figures 2.12A and 2.12B are now out of phase with one another. Figure 2.12C depicts how odd indexed sarcomeres are in phase with each other, similarly with even indexed compartments, but these two groups are out of phase with each other. By out of phase we mean that one group of sarcomeres are following the part of their period-double orbit during this pacing period where they have a higher peak Ca^{2+} subsarcolemmal concentration, whilst the other group have a lower peak. During

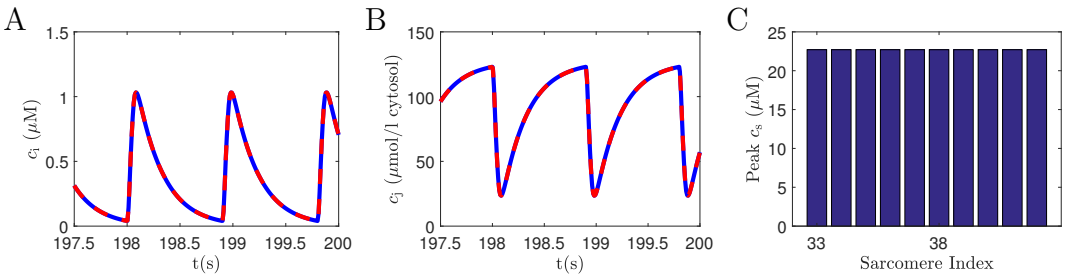

Figure 2.11: Simulation results from a network purely coupled through the cytosol such that the synchronised single period orbit is stable. The network consists of 75 sarcomeres purely coupled through the cytosol with $T_p = 0.9$ s and the coupling parameter $\tau_c = 3$ s. Plots showing the trajectories of bulk cytosolic Ca^{2+} concentration (A) and SR Ca^{2+} concentration (B) of two neighbouring sarcomeres (blue representing one sarcomere and the dashed red the other) in a 1D network. Bar plot showing the peak subsarcolemmal Ca^{2+} concentrations during one pacing period of the 10 innermost compartments within the 75 sarcomere network (C). All other parameters as in Appendix A.

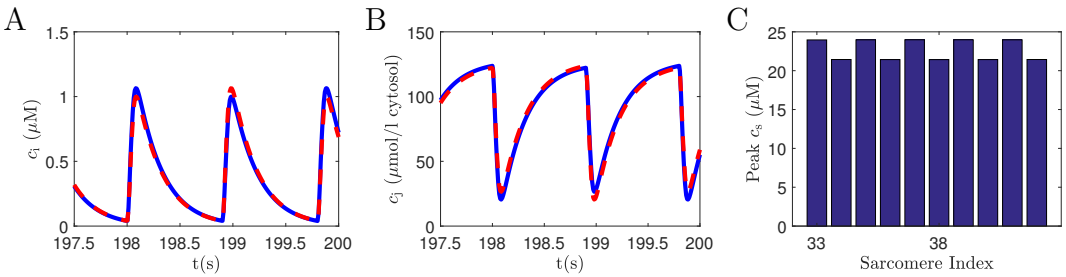

Figure 2.12: Simulation results showing the synchronised single period orbit has become unstable due to an increase of the cytosolic coupling strength compared to that used to produce Figure 2.11. The system consists of a network of 75 sarcomeres purely coupled through the cytosol with $T_p = 0.9$ s and the coupling parameter $\tau_c = 2.301$ s. Plots showing the trajectories of bulk cytosolic Ca^{2+} concentration (A) and SR Ca^{2+} concentration (B) of two neighbouring sarcomeres (blue representing one sarcomere and the dashed red the other) in a 1D network. Plot showing the peak subsarcolemmal Ca^{2+} concentrations during one pacing period of the 10 innermost sarcomeres within the 75 sarcomere network (C). All other parameters as in Appendix A.

the next pacing period these two groups then switch. We find this behaviour repeated throughout the network. This kind of behaviour has been labelled as spatial alternans. A look at the eigenvalues of these two systems, shown in Figure 2.13, reveal the form of bifurcation under which these spatial alternans form.

Comparing the eigenvalue plots in Figures 2.13A and 2.13B, we can see that by changing the value of the coupling strength the system has undergone a bifurcation, as suggested by Figures 2.11 and 2.12. Figure 2.13C is a zoom in of Figure 2.13B, revealing that the key eigenvalue has passed through the unit circle at -1.

Since we know that for $T_p = 0.9$ s the single sarcomere case follows a stable single-period orbit, we know that this behaviour has purely resulted from the increase in coupling strength. As discussed in Section 2.2, such behaviour has been seen before, by Restrepo *et al* [13]. In the Restrepo model this was due to the diffusion between sarcomeres causing a loss of synchrony between SR release due to some RyRs being activated before others. However, in our model the opening of the load-release function is already synchronized since it is clamped to I_{CaL}. This suggests the diffusion must be causing the onset of alternans through a different mechanism, perhaps involving a link with the SERCA pump, especially as diffusion within both our model, and Restrepo's model is modelled in the same manner. Having looked at some of the previously studied behaviour, in the next chapter we shall now to seek to expand upon these findings as well as introduce and study the effects of coupling through the SR.

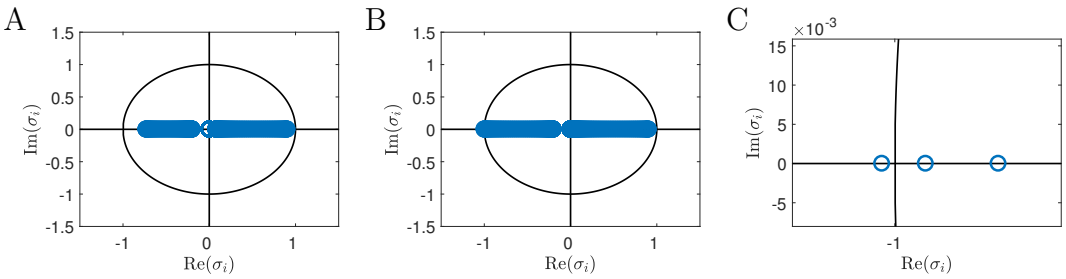

Figure 2.13: A comparison of the eigenvalues from the systems used to produce the results in Figures 2.11 and 2.12. Each eigenvalue plot relates to a system consisting of a network of 75 sarcomeres with coupling strengths of $\tau_c = 3$ s (A) and $\tau_c = 2.301$ s (B,C) and a pacing period of $T_p = 0.9$ s. All other parameters as in Appendix A.

3 The Role Of Sarcoplasmic Reticulum Ca^{2+}-ATPase Pumps and Diffusion

As discussed in Section 2.2.2 the SERCA pump has been shown to have a major influence on the appearance of calcium alternans. Computational studies have revealed that big increases or decreases in the uptake strength can repress alternans [8, 9, 11, 12]. However, these studies have tended to work at a fixed pacing period and thus only provide a limited picture. The stability approach in Section 2.4 has the advantage of allowing us to find critical values at which a bifurcation of the system takes place. In Section 3.2 we use this advantage to determine how the uptake strength (v_{up}) affects the value of the critical pacing period for a bifurcation of the system. By doing this we reveal which uptake strengths reduce the value of the critical pacing period under which alternans occur. We then perform simulations at pacing periods close to such critical pacing periods and use the results to portray how the shape of the orbit can affect the point at which alternans occur. Since SR release has also been deemed to have an important role in the onset of alternans [11], in Section 3.2 we also provide a plot illustrating how the value of the release slope (u) affects the values of the critical pacing period. We then compare the effects of the release slope against those of the SERCA pumps.

The effect of diffusion on the occurrence of alternans is far less understood. Whilst a few studies have alluded to it, as discussed in Section 2.2.2, these studies have looked at general coupling and not coupling across specific parts of the myocytes. That strong cytosolic coupling can produce nearest neighbour spatial alternans, as seen in Figure 2.12, is of great interest due to the link between small scale spatial patterns and more pathological patterns such as SDA. We are interested in finding out where these patterns come from and how they are linked to the loss of stability in the synchronised single-period orbit.

Our stability analysis can predict the behaviour of the system just after a bifurcation, without the need for arduous simulations, in terms of eigenvectors of the linearised system. This will be particularly useful where the resultant behaviour due to a bifurcation forms slowly over time. As a simple introduction to the eigenvectors of the system, in Section 3.1 we reveal the eigenvector related

to the behaviour in Figure 2.12 and explore how useful they are for predicting spatial patterning. We also use the analysis to show how the cytosolic coupling strength τ_c affects the critical pacing period in Section 3.2.2 for when a period-doubling bifurcation occurs. This informs us which pacing periods can be affected by strong cytosolic coupling and whether cytosolic coupling has more of an effect on slow or fast pacing periods.

Further to cytosolic diffusion, the other major route allowing Ca^{2+} to diffuse across the myocyte is through the SR network. As such, in Section 3.3, we introduce SR coupling to our model for a sarcomere network. By doing this we reveal how SR coupling allows the possibility of a '+1' bifurcation. This '+1' bifurcation produces a very different behaviour to the period-doubling bifurcation discussed in Section 2.5.

The networks studied in Section 3.2 and Section 3.3 are one-dimensional. This allows us to draw comparisons with previous work and helps to provide further insight on previous findings. However, the shape and layout of a myocyte means it can be easily described more realistically by increasing the dimension of the system. By altering our network to be 2D in Section 3.4 we explore the links and differences between the 1D and 2D networks. The final part of this chapter, Section 3.5, contains a summary of the chapter.

3.1 System Eigenvectors and Spatial Patterning

The stability approach discussed in Section 2.4 revealed how the eigenvalues of the system were the eigenvalues σ_i^ν of the matrices S_m^ν for all ν. The matrices S_m^ν were 5×5 matrices that describe how perturbations away from the synchronised state at the beginning of a pacing period progress across the whole pacing period. Although the matrices S_m^ν are developed for the system after it has undergone the transformation described in Section 2.4, these matrices can also be used to find the eigenvectors of the original system. To find these eigenvectors we first recognise that the matrices S_m^ν are taken from a block diagonal matrix S_m that

satisfies the following equation:

$$\delta y_{m+1} = \begin{pmatrix} \delta y^1_{m+1} \\ \delta y^2_{m+1} \\ \vdots \\ \delta y^N_{m+1} \end{pmatrix} = \begin{pmatrix} S^1_m & 0 & \cdots & \cdots & 0 \\ 0 & S^2_m & \ddots & \ddots & \vdots \\ \vdots & \ddots & \ddots & \ddots & \vdots \\ \vdots & \ddots & \ddots & S^{N-1}_m & 0 \\ 0 & \cdots & \cdots & 0 & S^N_m \end{pmatrix} \begin{pmatrix} \delta y^1_0 \\ \delta y^2_0 \\ \vdots \\ \delta y^N_0 \end{pmatrix} = S_m \delta y_0 \qquad (3.1)$$

where N is the total number of sarcomeres in the network. To find the eigenvectors of the original system we first find the eigenvectors of S_m and assign them to a matrix S_{eig}. We then take the matrix L, that contains the eigenvectors of the connectivity matrix G and, using this, we reverse the transformation used to create the vector $\delta y^\nu_z \in \mathbb{R}^5$ noting that each δy^ν_z has five eigenvectors associated with it. We recall from Section 2.4 that z defines which switching event we are focused around and ν the sarcomere chosen. Thus δy_{m+1} is a vector with $5N$ components at the $m+1$th switching event.

As we saw in Section 2.5.2, an increase in the strength of coupling through the cytosol can cause the synchronised single-period orbit within a network of sarcomeres to go unstable via a period-doubling bifurcation. Further to this, Figure 2.13C revealed that as well as the appearance of period-double orbits, the sarcomeres displayed a spatially alternating pattern. To help us understand where this may come from in Figure 3.1B we have shown a part of the eigenvector related to the eigenvalue lying outside the unit circle in Figure 3.1A. Figure 3.1C is a plot of the values of the components in the unstable eigenvector related to all the subsarcolemmal Ca^{2+} concentrations within the network. Throughout the rest of this thesis, eigenvectors related to eigenvalues lying outside the unit circle shall be referred to as unstable eigenvectors.

The eigenvector plots in Figure 3.1B and 3.1C, reveals that as the orbit is perturbed from the synchronised single-period orbit, the trajectories of neighbouring sarcomeres will grow in opposite directions to one another. Such behaviour agrees with that seen in Figure 2.13C. Thus, a comparison of the part of the eigenvector accounting for the same component across sarcomeres informs the spatial pattern we would expect to see just after the synchronised single-period orbit loses sta-

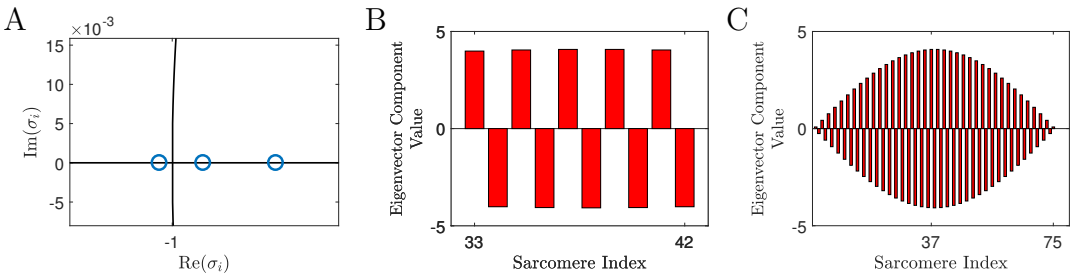

Figure 3.1: Stability analysis results for a system in which the synchronised single period orbit is unstable due to strong cytosolic coupling between sarcomeres. The system consists of a network of 75 sarcomeres purely coupled through the cytosol with $T_p = 0.9$ s and the coupling parameter $\tau_c = 2.301$ s. Eigenvalues are plotted in A and the bar plot in B contains the values of the components in the unstable eigenvector related to 10 subsarcolemmal concentrations within the network for the eigenvalue lying outside the unit circle. The bar plot in C contains the values of the components in the unstable eigenvector related to all the subsarcolemmal Ca^{2+} concentrations within the network. All other parameters as in Appendix A.

bility. Most notably these results demonstrate that our stability analysis agrees with our simulations at both the single cell and network level.

Another advantage of these eigenvectors can be illustrated when considering the behaviour of a network under stronger coupling. Whilst the simulation and analysis in Figures 2.12 and 3.1 focus on the behaviour when the synchronised single-period orbit has just lost stability, it is important to discuss what happens under even stronger coupling. On display in Figure 3.2 are the peak subsarcolemmal Ca^{2+} concentrations during a single pacing period for a network of 75 sarcomeres. Both Figures 3.2A and 3.2B contain all the sarcomeres within the network. Figure 3.2A is from a network that has the same coupling strength, $\tau_c = 2.301$ s, as seen previously in Section 2.5.2. On the other hand, Figure 3.2B is the result from a network under slightly stronger coupling, $\tau_c = 2.29$ s.

Before discussing differences between the two figures, we should discuss the overall distribution of Ca^{2+} within the network. As both Figures 3.2A and 3.2B reveal, the amplitude of the spatial alternan is greater towards the centre of the myocyte. By amplitude of the spatial alternan, we mean the difference in free intracellular Ca^{2+} concentration between neighbouring sarcomeres. Considering the make up of our network, the shape of this distribution is likely due to the interplay between the no flux boundary conditions and the strength of the coupling parameter. A simulation of the network, shown in Figure 3.3 with periodic

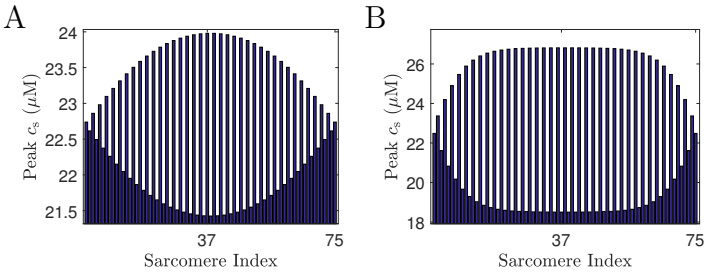

Figure 3.2: A comparison of the peak subsarcolemmal Ca^{2+} concentrations during one pacing period for two networks with different cytosolic coupling strengths. The network contains 75 sarcomeres purely coupled through the cytosol with $T_p = 0.9$ s and coupling strengths of either $\tau_c = 2.301$ s (A) or $\tau_c = 2.29$ s (B). All other parameters as in Appendix A.

boundaries supports this. As Figure 3.3A illustrates there are no variations in the alternans size across the whole network. Figures 3.3B and 3.3C confirm that this is the expected behaviour just after a bifurcation of the synchronised single-period state.

Now, comparing Figures 3.2A and 3.2B we see that the distribution in Ca^{2+} across the myocyte changes. In Figure 3.2B the size of the spatial alternans at the centre of the myocyte is greater than that in Figure 3.2A. The spatial alternans also increase in amplitude much faster moving from the edges of the myocyte towards the centre in Figure 3.2B. However, this large increase in spatial alternan amplitude is spread across fewer sarcomeres, with multiple sarcomeres now sharing similarly sized spatial alternans towards the centre. This change of behaviour appears to represent an increase in the effect of the coupling parameter over the boundary conditions.

As well as these descriptions regarding the change of behaviour under increased coupling strength, the eigenvectors can also lend some further mathematical insight. Figure 3.4 gives the results of the stability analysis performed upon the network with the increased coupling strength of $\tau_c = 2.295$ s. As we can see, the increase has caused two further eigenvalues to leave the unit circle in the negative direction along the real axis. Due to this, the network now has three eigenvectors affecting the trajectory as we perturb it from the now unstable synchronised single-period orbit. The eigenvector displayed in Figure 3.4B is qualitatively the same as we have seen in Figure 3.1C when working with a coupling strength of $\tau_c = 2.301$ s, whilst Figures 3.4C and 3.4D display the new eigenvectors.

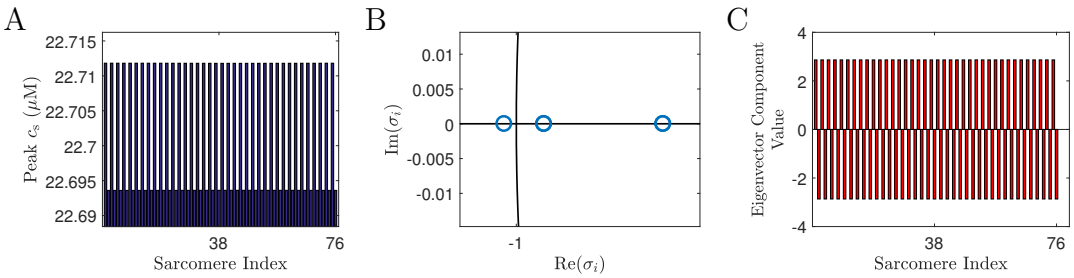

Figure 3.3: Results and stability analysis of a system with periodic boundary conditions and an unstable synchronised state due to strong cytosolic coupling between sarcomeres. The system consists of a network of 76 sarcomeres purely coupled through the cytosol with $T_p = 0.9$ s and $\tau_c = 2.301$ s. Bar plot(A) showing the peak subsarcolemmal Ca^{2+} concentrations during one pacing period. Eigenvalue plot(B) of the eigenvalue outside the unit circle with the values of the components in the unstable eigenvector related to all the subsarcolemmal Ca^{2+} concentrations within the network contained in the bar plot(C). All other parameters as in Appendix A.

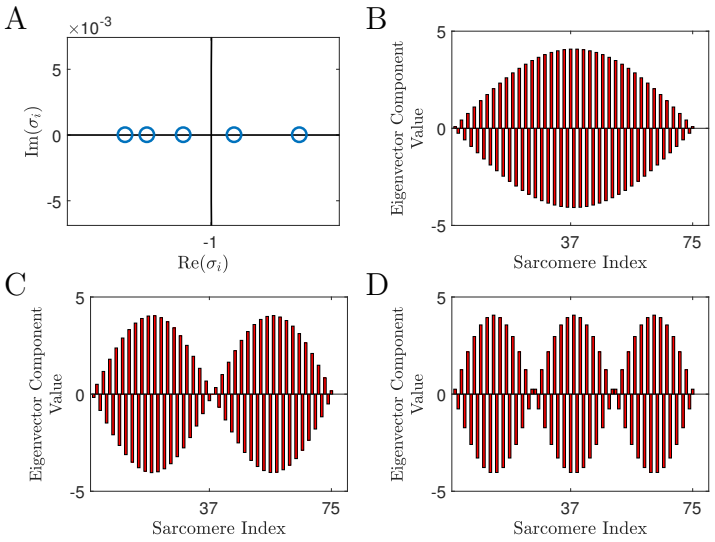

Figure 3.4: The values of the components in the unstable eigenvectors related to the the subsarcolemmal Ca^{2+} concentrations for the system used to produce Figure 3.2B. The system consists of a network of 75 sarcomeres purely coupled through the cytosol with $T_p = 0.9$ s and $\tau_c = 2.29$ s. Eigenvalue plot (A) and bar plots (B,C,D) showing the values of the components in the unstable eigenvectors related to the the subsarcolemmal Ca^{2+} concentrations. All other parameters as in Appendix A.

Comparing the eigenvectors in Figure 3.4 to the behaviour seen in Figure 3.2B, it is clear that none of the eigenvectors solely reflect the result of the system but a combination of the three does. Further still we are able to approximate the linear combination of these eigenvectors that lead to this behaviour. In Figure 3.5 we have plotted the linear combination added to the peak subsarcolemmal Ca^{2+} concentration of the uncoupled case in pale blue. We have then overlayed the plot in Figure 3.2B in grey.

Figure 3.5 illustrates that as we move further from the bifurcation point the eigenvectors predictive power lessens. This will be due to non-linear behaviour in the model that is missed through the linearisation in the stability analysis. However, Figure 3.5 reveals that our stability analysis is still able to capture some key features of the system through the eigenvectors. These features include the reduced effect of the boundary conditions depicted by the steeper increase in the alternans amplitude as we move inwards compared to the weaker coupling.

These findings inform us that an increase in the coupling strength within the network can produce new spatial patterns. These patterns are dictated by the unstable eigenvectors. This is contrary to previous studies that suggested the more complex spatial patterns were due to an increase in network size [1]. We would suggest that such theories are not in fact true since we have performed simulations with varying network sizes, including those in [1], at the point where the synchronised single-period orbit goes unstable due to purely cytosolic coupling, and the results of such simulations show behaviours qualitatively similar to that in Figure 3.2A. Thus we surmise that it is the increase in coupling strength, not an increase in network size, that alters the unstable behaviour within our network.

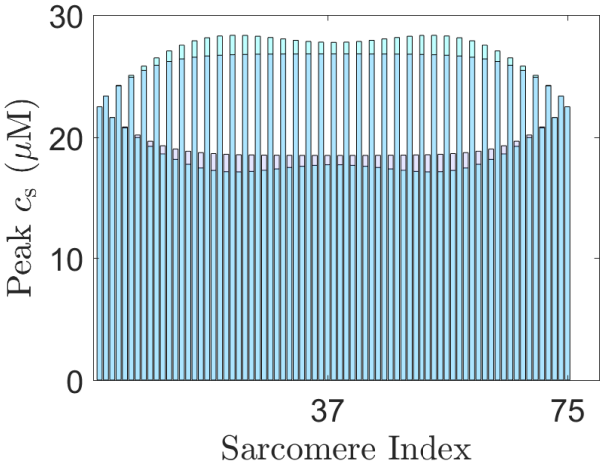

Figure 3.5: Plot comparing a linear combination of the values of the components in the unstable eigenvectors related to the the subsarcolemmal Ca^{2+} concentrations seen in Figure 3.4 against simulation results. Bar plot (pale blue) of the linear combination of the values of the components in the unstable eigenvectors related to the the subsarcolemmal Ca^{2+} concentrations added to the uncoupled peak subsarcolemmal Ca^{2+} concentrations produced by a network of 75 sarcomeres with $T_p = 0.9$ s and $\tau_c = 2.29$ s. Overlayed bar plot(grey) of peak subsarcolemmal Ca^{2+} concentrations from a simulation of same system. All other parameters as in Appendix A.

3.2 The Parameter Effects On The Critical Pacing Period

3.2.1 The Balance Between The Uptake Strength, Sarcoplasmic Reticulum Release and Critical Pacing Period

In Figures 2.8 and 2.9 we demonstrated how an increased pacing frequency caused a period-doubling bifurcation in a single myocyte. This implies that at these faster pacing rates, the Ca^{2+} levels within the SR and cytosol are unable to reach the same levels at the end of the pacing period as they were at at the start. As discussed in Section 2.2.2, if the SERCA pumps cannot fully replenish the SR Ca^{2+} concentration during a single pacing period or if too much of the SR Ca^{2+} concentration is released during a single pacing period then Ca^{2+} alternans can occur. Within the PWL Shiferaw-Karma model, such a balance between the SERCA pump activity or SR release against the pacing period can be explored using the stability approach discussed in Section 2.4. Using this approach we illustrate how the critical pacing period for a period-doubling bifurcation is affected by either changing the uptake strength (v_{up}) or the release slope (u). The results of this are shown in Figure 3.6.

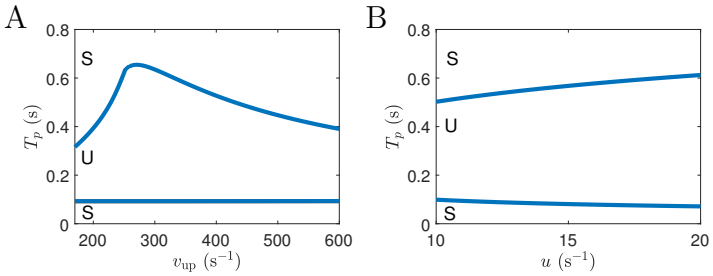

Figure 3.6: Plots showing the critical pacing period (T_p) for a period-doubling bifurcation to occur in the single cell case against either (A) the uptake strength (v_{up}) or (B) the release slope (u). In both A and B a single-period orbit is stable in the regions labelled S, whilst a single-period orbit is unstable in the region labelled U. The blue lines represent where a period-doubling bifurcation takes place. All other parameters as in Appendix A including u in A and v_{up} in B.

Figure 3.6A reveals that the relationship between v_{up} and critical pacing period is non-linear. The plot reveals that for both small and large v_{up} the possibility of alternans is decreased. Interestingly this balance is asymmetric around the uptake strength at which alternans are most likely. An increase in v_{up} from the uptake strength with the highest critical pacing period causes a gradual decrease in the critical pacing period for the onset of alternans. On the other hand, a decrease leads to a steeper decrease in the critical period.

The increase in uptake strength means the SR can be fully replenished in less time. This helps to maintain the balance between SR release and the SERCA pumps at faster pacing periods, key to preventing alternans. To understand how a decrease in uptake strength can also decrease the critical pacing period we have performed simulations of the system with different uptake strengths. Each of these simulations were performed using pacing periods close to the critical pacing period related to that uptake strength. The Ca^{2+} concentrations of the unrecruited JSR from these simulations are contained in Figures 3.7A-C along with a plot of the load-release function Q in Figure 3.7D.

In Figures 3.7A to 3.7C we have plotted the switching points, the points at which one of the system functions change form, within the system as stars. The green stars represent that start and end of a single pacing period. The red stars represent the switch in the load-release function as the unrecruited JSR Ca^{2+} concentration crosses a value of 115 μmol/l cytosol. As we can see from Figure 3.7D when concentration drops below 115 μmol/l cytosol, the gradient of release

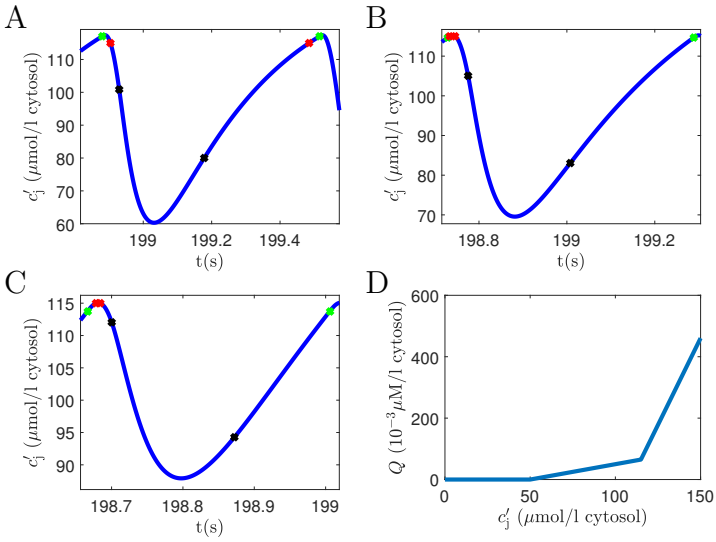

Figure 3.7: A comparison of the Ca^{2+} concentrations of the unrecruited JSR in systems with differing pacing periods and uptake strengths. Plots are for systems with $T_p = 0.6354$ s and $v_{up} = 300$ s^{-1} (A), $T_p = 0.5598$ s and $v_{up} = 240$ s^{-1} (B) and $T_p = 0.3396$ s and $v_{up} = 180$ s^{-1} (C). The green stars represent that start and end of a single pacing period. The green stars represent that start and end of a single pacing period. The red stars represent a switch in the load-release function. The black stars represents a voltage dependent switch. Plot D shows the load-release function against the unrecruited JSR Ca^{2+} concentration. All other parameters as in Appendix A.

significantly decreases. The black stars represent voltage based switches within the system. The first is the inactivation of the L-type Ca^{2+} channel and the second is a change in the shape of the NCX. Due to the clamped voltage, the order of the voltage switches does not change.

By comparing Figures 3.7A-C we can see that as we decrease the uptake strength the overall order of the switches change. As seen in Figure 3.7A, for higher values of v_{up}, the Ca^{2+} concentration in the unrecruited JSR starts above 115 μmol/l cytosol. This means that the load-release function is at its steepest from the start of the pacing period leading to a larger SR release. However as Figures 3.7B and 3.7C reveals, a large enough drop in the uptake strength leads to the scenario where the Ca^{2+} concentration in the unrecruited JSR is not above the value of 115 μmol/l cytosol from the start. It does briefly cross this switch soon after but overall the time spent in the region of steeper release is far less than for greater uptake strengths. This leads to a significantly smaller SR release and thus means the SERCA pump is able to fully replenish the SR in a shorter amount of time despite. This is able to occur even though the uptake strength is

weaker.

These insights into the effects of low level uptake strength in the SERCA pumps illustrate the importance of the shape of the load-release function when studying the SERCA pump. As we have seen, by decreasing the uptake strength enough that the Ca^{2+} concentration in the unrecruited JSR cannot be replenished to levels needed to activate steep release from the load-release function at the beginning of the pacing period, we can suppress alternans. Further still, these insights suggest that if we decrease the switch at which we move into steeper release within the load-release function we should shift the plot in Figure 3.6A towards lower uptake strengths. An example of this shift is contained within Figure 3.8.

Figure 3.8 demonstrates that, as suggested, if we decrease the value of c_j' at which the load-release functions undergoes a switch then the the peak critical pacing period shifts towards a lower uptake strength. Figure 3.8 also reveals an increase in the value of the peak critical pacing period. However, increasing or decreasing the uptake strength from the value related to the peak critical pacing period causes a steeper decline in the critical pacing period.

As discussed in Section 2.2, similar findings illustrating that alternans can be suppressed by a large reduction of the uptake strength of the SERCA pump have been found in two separate models, one by Nivala and Qu [9], the other by Huertas *et al* [12]. However, unlike in those models where such findings were based on reduced maps of the system, we have been able to study the full system stability directly. Furthermore, our direct technique has allowed us to reveal the critical pacing periods for multiple values of the SERCA pump uptake strength without the need for multiple numerical simulations. Within the context of our model, the large reduction in uptake strength appears to suppress alternans since the SR can no longer fill to a Ca^{2+} concentration level at which the load-release function has a steep release curve for a reasonable amount of time. Thus we have shown how important the balance in activity between the load-release function and the SERCA pump is in suppressing alternans.

Figure 3.6B displays that when the value of the release slope is increases, the length of the pacing period needed to still have a stable single-period orbit

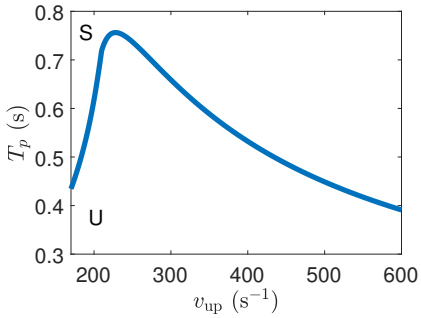

Figure 3.8: Plot showing the critical pacing period (T_p) for a period-doubling bifurcation to occur in the single cell case against the uptake strength when the switch for steeper release in the load-release function has shifted to $c_{\mathrm{j}}' = 105$ μmol/l cytosol. A single-period orbit is stable in the regions labelled S, whilst a single-period orbit is unstable in the region labelled U. The blue lines represent where a period-doubling bifurcation takes place. All other parameters as in Appendix A.

also increases. Again, in terms of the biology, this is what we would expect as the larger the amount of Ca^{2+} released from the SR into the cytosol, the more time needed by the cell to recover its SR Ca^{2+} levels. However, despite the wide spread in release slope values studied we see the changes in the critical pacing period are much smaller than when the uptake strength is varied. This suggests the balance between when steep release from the load-release function begins and the uptake strength is more important to the onset of alternans than the balance between the uptake strength and release slope. Both these relationships reveal how a mishandling of the release and uptake of Ca^{2+} by the SR in a single cell case can cause Ca^{2+} alternans.

We also note that both Figure 3.6A and Figure 3.6B reveal that if the pacing period is short enough alternans can be suppressed across all values of either the uptake strength or release slope. This agrees with the behaviour seen in the original Shiferaw-Karma model [11]. However simulations reveal that at these pacing periods the Ca^{2+} concentration in the bulk cytosol remains high throughout the whole pacing period. Such behaviour is pathological as it means the contractile machinery within the myocyte cannot relax. This illustrates the importance of studying the behaviour of the system, even when it follows a single period orbit.

3.2.2 Balance Between Coupling Strength and Critical Pacing Period

Just as we have done with the single cell case we will now study how the strength of coupling between sarcomeres through the cytosol affects the value of the critical pacing period at which a period-doubling bifurcation occurs. As with the single cell case we use the stability techniques discussed in Section 2.4 to analyse the system at the bifurcation point. The results of such analysis can be seen in Figure 3.9. Here the blue line represents the relationship between the cytosolic coupling parameter (τ_c) and the critical pacing period at which the synchronised single-period orbit undergoes a period-doubling bifurcation. In the region labelled S the synchronised single-period orbit is stable whilst it is unstable in the region labelled U. For pacing periods below the red line the uncoupled sarcomere has a stable period-double orbit as opposed to a stable single period orbit.

From Figure 3.9 we can see that when cytosolic coupling is weak, represented by larger values in τ_c, the critical pacing period required for alternans is faster. Looking at low values of τ_c reveals a steep increase in the critical pacing period for small decreases in τ_c. This informs that when coupling is strong, any small changes to the the coupling strength can significantly increase the possibility of alternans. On the other hand, as τ_c approaches infinity, the blue plot in Figure 3.9 approaches the critical pacing period for a period-doubling bifurcation to take place in the single sarcomere case. Section 4.4 will discuss whether this means cytosolic coupling can cause spatial alternans for pacing periods under which a period-doubled orbit is stable in the uncoupled case no matter the value of τ_c.

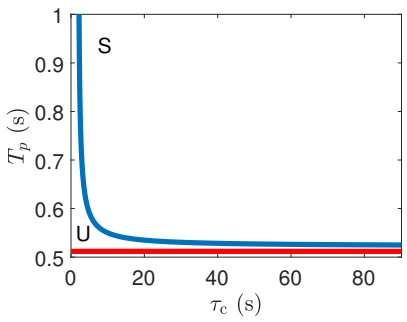

Figure 3.9: Plot showing how the cytosolic coupling strength (τ_c) affects the value of the critical pacing period (T_p) at which a period-doubling bifurcation of the synchronised single-period orbit occurs (blue line) in a 1D network containing 75 sarcomeres. The synchronised single-period orbit is stable in the region labelled S and unstable in the region labelled U. The red line marks the critical pacing period where the uncoupled case undergoes a bifurcation. All other parameters as in Appendix A.

3.3 Introduction Of Sarcoplasmic Reticulum Coupling Into A One-Dimensional Network

Although coupling through the SR has been included in many subcellular network models, the actual effects of such coupling has barely been considered in the literature. This can partly be explained by the lack of understanding in the level of Ca^{2+} diffusion within the SR. A clear example of this lack of understanding comes from comparing the results of two experimental studies [103, 104], in which the two studies disagree about the diffusion constant of Ca^{2+} by almost a factor of 10. Such disagreements are reviewed by Bers and Shannon [105].

Despite these discrepancies, it is still of great interest to study the effects of SR diffusion upon the system, particularly as cytosolic Ca^{2+} diffusion has been shown to promote instabilities [1].

3.3.1 Pure Sarcoplasmic Reticulum Coupling Within A One-Dimensional Network

Staying within the confines of the 1D network, we will now look at what behaviours the system has when subcellular sections are coupled only through the SR. As, with cytosolic coupling we first performed some simulations at different coupling strengths, results of which can be seen in Figures 3.10 and 3.11.

Figure 3.10 reveals that if the coupling is weak enough the network lies in a

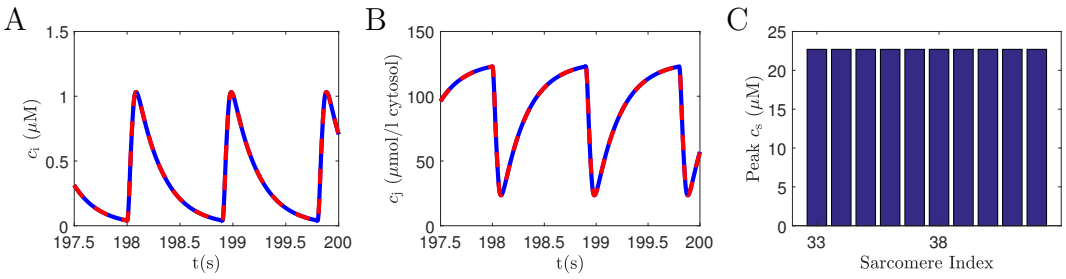

Figure 3.10: Simulation results of a network purely coupled through the SR such that the synchronised single period orbit is stable. The network consists of 75 sarcomeres purely coupled through the SR with $T_p = 0.9$ s and the coupling parameter $\tau_{\text{sr}} = 15$ s. Plots showing the trajectories of bulk cytosolic Ca^{2+} concentration (A) and SR Ca^{2+} concentration (B) of two neighbouring sarcomeres (blue representing one sarcomere and the dashed red the other) in a 1D network. Bar plot showing the peak subsarcolemmal Ca^{2+} concentrations during one pacing period of the 10 innermost compartments within the 75 sarcomere network (C). All other parameters as in Appendix A.

synchronous state. Thus the behaviour for weak coupling through the SR is the same as we have seen with coupling through the cytosol. Additionally, as with cytosolic coupling, the sarcomeres all follow the same single-period orbit as the uncoupled sarcomere in this synchronous state. However the strength of coupling purely through the SR to maintain a stable synchronous state needs to be weaker comparatively to when we couple purely through the cytosol. As we increase the coupling strength through the SR we move from the synchronous state to the behaviour displayed in Figure 3.11.

As Figure 3.11 reveals the synchronous state of the system has become unstable. However, the form this instability has taken is different to that found with cytosolic coupling. We can see from Figures 3.11A and 3.11B that two neighbouring subcellular components within the system still exhibit single-period orbits. On the other hand, the figures illustrate that these orbits are no longer identical to one another. Figure 3.11C depicts the spatial pattern between neighbouring orbits throughout a section of the network. As we can see, a high-low pattern has developed for the peak subsarcolemmal Ca^{2+} concentrations between neighbouring sarcomeres. This may appear similar to the behaviour seen in Figure 2.12C but since the orbits are not period-doubled in the SR coupled case, we do not see a reverse of the pattern from beat-to-beat. To understand how this instability has arisen, we have performed stability analysis on the two cases displayed in Figure

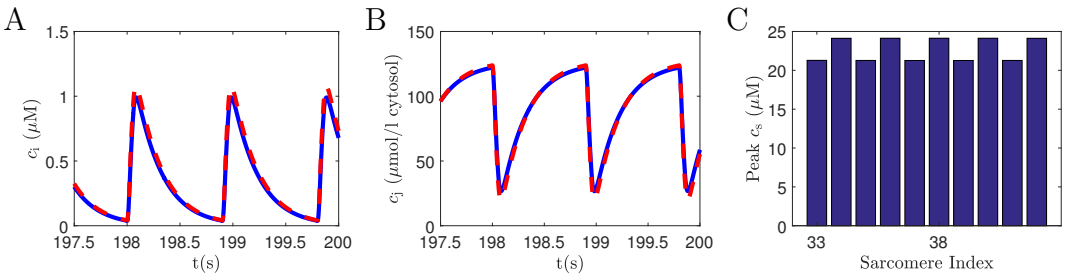

Figure 3.11: Simulation results from a network in which the synchronised single period orbit has become unstable due to an increase in the SR coupling strength compared to that used to produce Figure 3.10. The network consists of 75 sarcomeres purely coupled through the SR with $T_p = 0.9$ s and the coupling parameter $\tau_{\text{sr}} = 12.89$ s. Plots showing the trajectories of bulk cytosolic Ca^{2+} concentration (A) and SR Ca^{2+} concentration (B) of two neighbouring sarcomeres (blue representing one sarcomere and the dashed red the other) in a 1D network. Bar plot showing the peak subsarcolemmal Ca^{2+} concentrations during one pacing period of the 10 innermost compartments within the 75 sarcomere network (C). All other parameters as in Appendix A.

3.10 and Figure 3.11. Figure 3.12 portrays the results of our stability analysis.

Figures 3.12A and 3.12B are eigenvalue plots related to the behaviours shown in Figures 3.10 and 3.11 respectively. Figure 3.12C ic a closer look at the +1 boundary of the unit circle in Figure 3.12B. A comparison of these three figures reveals that coupling strongly enough through the SR causes the synchronous state to become unstable. Furthermore, the change in stability is via a '+1' bifurcation compared to the period-doubling bifurcation seen with strong cytosolic coupling. Now looking at Figure 3.12D, we can immediately tell that trajectories of neighbouring sarcomeres indeed progress away from the synchronous orbit in opposing directions. This agrees with the spatial behaviour observed in Figure 3.11C. Hence, we can say that if the system is strongly coupled purely through the SR, then the system undergoes a '+1' bifurcation where the synchronous state becomes unstable and neighbouring subcellular components approach different new single-period orbits in opposing directions.

As with the cytosolic coupling strength, we also studied how altering the strength of coupling through the SR changes the value of the critical pacing period at which an instability of the synchronous state arises. The results of this study are shown in Figure 3.13. This time the blue line represents the point at which the synchronised state undergoes a '+1' bifurcation. The red line again marks the critical pacing period for a bifurcation in the uncoupled case. As before

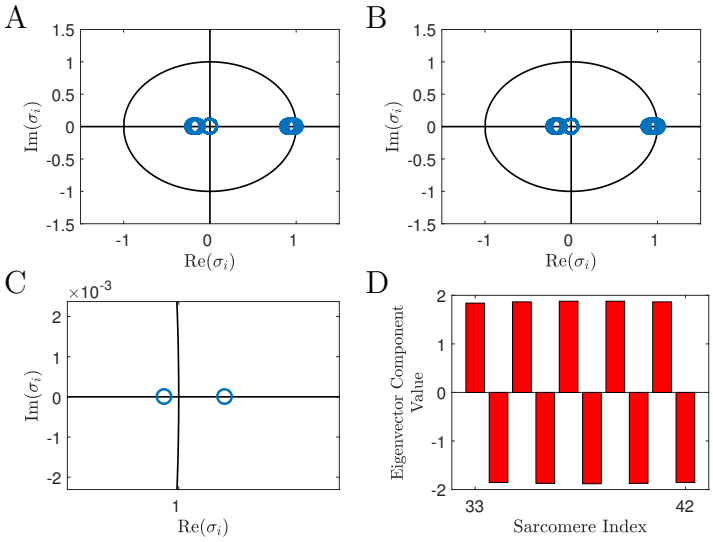

Figure 3.12: Stability analysis output for the systems used to produce the results seen in Figures 3.10 and 3.11. Each system consists of network of 75 sarcomeres purely coupled through the SR with $T_p = 0.9$ s and either $\tau_{\text{sr}} = 15$ s (A) or $\tau_{\text{sr}} = 12.89$ s (B,C,D). Plots showing the eigenvalues for coupling strengths of $\tau_{\text{sr}} = 15$ s (A) and $\tau_{\text{sr}} = 12.89$ s (B,C) along with a bar plot (D) of the values of the components in the unstable eigenvector related to 10 subsarcolemmal Ca^{2+} concentrations within the network. All other parameters as in Appendix A.

the synchronised single-period orbit is stable in the region labelled S and unstable in the region labelled U.

Figure 3.13 reveals a very different kind of relationship for SR coupling compared to that described in Figure 3.9 for cytosolic coupling. To begin with, much like with cytosolic coupling, as we weaken the coupling strength, the critical pacing period at which an instability occurs becomes shorter. However, staying above the red line, it appears that we will eventual reach a point at which the coupling becomes too weak to achieve an instability for any pacing periods. We shall take a closer look at this behaviour in Section 4.2.

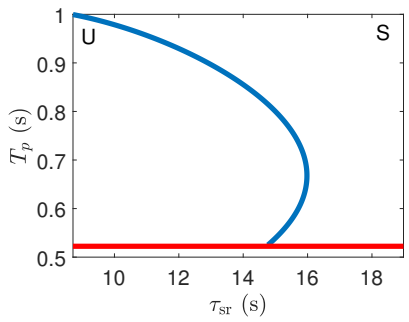

Figure 3.13: Plot showing how the SR coupling strength (τ_{sr}) affects the value of the critical pacing period (T_p) at which a '+1' bifurcation of the synchronised single-period orbit occurs (blue line) in a 1D network containing 75 sarcomeres. The synchronised single-period orbit is stable in the region labelled S and unstable in the region labelled U. The red line marks the critical pacing period where the uncoupled case undergoes a bifurcation. All other parameters as in Appendix A.

3.3.2 Joint Coupling In A One-Dimensional Network

So far we have looked at the cases where sarcomeres are either coupled through the SR or the cytosol. Biologically though, in a myocyte they would be coupled through both. We have seen that purely coupling through the cytosol strongly enough, the synchronised state undergoes a period-doubling bifurcation. On the other hand, by purely coupling through the SR strongly enough we have seen the synchronised state undergoes a '+1' bifurcation. When we combine these two forms of coupling we find that these two bifurcations remain and are dependent on which form of coupling is the most dominant. We also find that no other forms of bifurcation appear as a result of the combined coupling. Using this information we have studied the balance between the two coupling parameters and the critical pacing period at which the synchronised state undergoes either possible bifurcation. The results are best described as a contour plot, which is shown in Figure 3.14.

Figure 3.14A describes two very different looking relationships depending upon which form of bifurcation we are looking for. It reveals how, for a set pacing period, the synchronous state can become unstable when the coupling through either component becomes significantly stronger than the coupling through the other. For stronger coupling through the SR the loss of stability occurs via a '+1' bifurcation whilst for stronger coupling through the cytosol it occurs via period-doubling bifurcation. We will denote the coupling that dictates the type

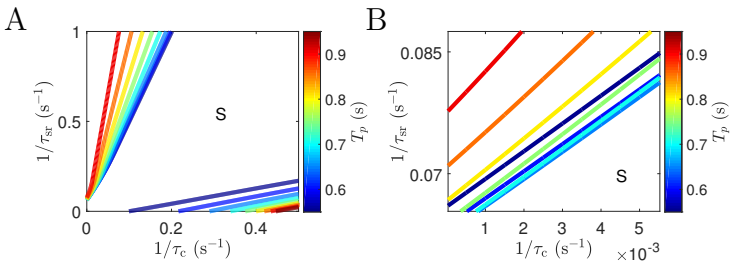

Figure 3.14: Contour plots showing the values of the critical pacing period (T_p), cytosolic coupling strength (τ_c) and SR coupling strength (τ_{sr}) that can lead to a bifurcation of the synchronised state in a 1D network containing 75 sarcomeres. Contour plot (A) shows the values for both a '+1' bifurcation (Plots stemming from the y-axis) or a period-doubling bifurcation (Plots stemming from the x-axis). The plot in 3.14B gives a closer look at Figure 3.14A, focusing on the part where the plot shows the values of $1/\tau_{sr}$ and the critical pacing period for a '+1' bifurcation when the value of $1/\tau_c$ is small. Note on the axes we have used $1/\tau_c$ and $1/\tau_{sr}$ so we can see the effect of weak coupling. S labels the region in which the synchronised state is stable. All other parameters as in Appendix A.

of bifurcation that occurs as the dominant coupling from now. For example a '+1' bifurcation can only occur when SR coupling is significantly stronger the cytosolic coupling, therefore SR coupling would be deemed the dominant form of coupling.

Figure 3.14A also reveals that as we increase the pacing period, the difference between the dominant and non-dominant coupling strengths needs to be greater for a bifurcation to take place. There is an exception to this though for a '+1' bifurcation to take place when cytosolic coupling is very weak. To understand this exception we refer to Figure 3.14B. Figure 3.14B shows the region in Figure 3.14A at which the synchronised state undergoes a '+1' bifurcation when cytosolic coupling is weak. In Section 3.3.1 we saw that as we decreased the pacing period enough, the coupling through the SR needed to increased for '+1' bifurcation to occur. As Figure 3.14B illustrates this behaviour is not just limited to pure SR coupling but can be found under dominant SR coupling in the joint case. This is most clearly seen by considering the order of the different coloured plots, which each represent a set pacing period. As we can see, some of plots for the fastest pacing periods lay closer to the y-axis compared to some for the slower pacing periods. This informs us that at these pacing periods, when cytosolic coupling is weak the SR coupling needs to be stronger creating an area of bistability. However if we turn our attention to the top of Figure 3.14A which describes the scenarios

under which a '+1' bifurcation occurs whilst cytosolic coupling is strong, we see that the colour order has altered. The colours now lay in such order that if we trace over them from left to right their respective pacing periods consistently decrease, notifying us that this area of bistability no longer exists.

Another key point to take from Figure 3.14 is that two same coloured plots, each representing one form of the two types of bifurcation for a fixed value of the critical pacing period, do not appear to ever cross. Furthermore, they appear to be moving away from each other as the coupling strengths are increased, implying that there is no point where both bifurcations can occur simultaneously. In Figure 3.14, we can see that for a set critical pacing period the balance between the two coupling strengths required for a '+1' and period-doubling bifurcation to occur is very sensitive. By sensitive, we mean that a small increase in the non-dominant coupling strength requires a significant increase in the dominant coupling strength for a bifurcation to still occur. Furthermore, as the pacing period slows this balance becomes even more sensitive, with further increases needed in the dominant coupling strength for a bifurcation to take place. This suggests for both regimes that diffusion creates such instabilities as it creates an uneven distribution between neighbouring sarcomeres, in terms of either the SR or cytosolic Ca^{2+} concentrations. These uneven distributions must then be resolved by other mechanisms, such as SERCA pumps, in the myocyte.

3.4 Two-Dimensional Networks

Having explored 1D networks we now describe what happens when we look at the cytosolic and SR coupling within a 2D network of sarcomeres. As discussed in Section 2.1 the layout of the myofibrils and z-discs in the myocyte help us to imagine the myocyte as a rectangular grid. Whilst the z-discs provide clear borders we also treat the half way point in the space between two myofibrils as a border. This space contains cytosol and SR, thus allowing us to couple the sarcomeres in the transversal direction. A visual representation of this layout can be seen in Figure 3.15.

For this section, as well as Section 4, we will be using a network containing 10 myofibrils, with each myofibril containing 25 sarcomeres.

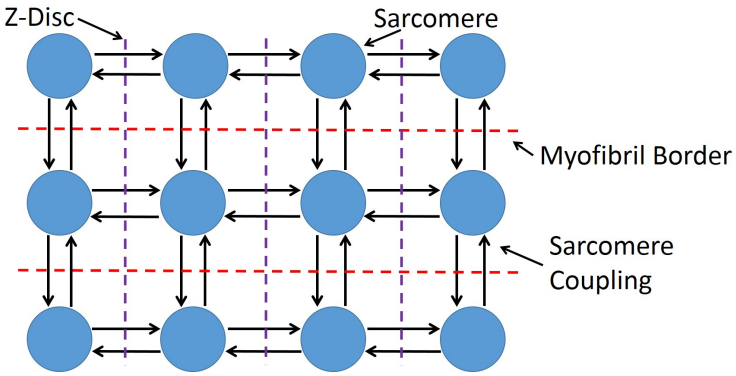

Figure 3.15: Visual example showing the kind of layout we will be using in Section 3.4. This example contains 12 sarcomeres (blue circles). The arrows show the coupling between sarcomeres whilst the red dashed lines show the divided between the myofibrils.

3.4.1 Cytosolic Coupling In A Two-Dimensional Network

We will begin by looking at purely cytosolic coupling first, then purely SR coupling before finally combining the two. The results of two simulations of networks with purely cytosolic coupling can be seen in Figure 3.16 and Figure 3.17.

As we saw with our 1D network, Figure 3.16 reveals that for weak coupling our 2D network reaches a stable synchronous state across all sarcomeres. This is most clearly demonstrated in Figure 3.16C, which represents the peak subsarcolemmal Ca^{2+} concentration during a single pacing period. Furthermore, as found in the 1D network, the orbit that all these sarcomeres take within this stable synchronous state, is the same as that of the single-period orbit for the uncoupled single sarcomere under the same pacing period. This illustrates that the shift in dimensionality of the network has no effect on the system's orbit when the system is in a synchronous state.

Moving our attention over to Figure 3.17, we can see that as we increase the strength of coupling through the cytosol, the synchronous state becomes unstable and the system undergoes a bifurcation. As Figures 3.17A and 3.17B reveals, individual sarcomeres now follow a period-doubled orbit and that neighbouring sarcomeres follow this period-double orbit out of phase with one another. Figure 3.17C demonstrates that this behaviour is repeated across the network. Furthermore, if we take a sarcomere in the network and compare it to another sarcomere two steps over in all four directions, these sarcomeres are in synchrony in terms of

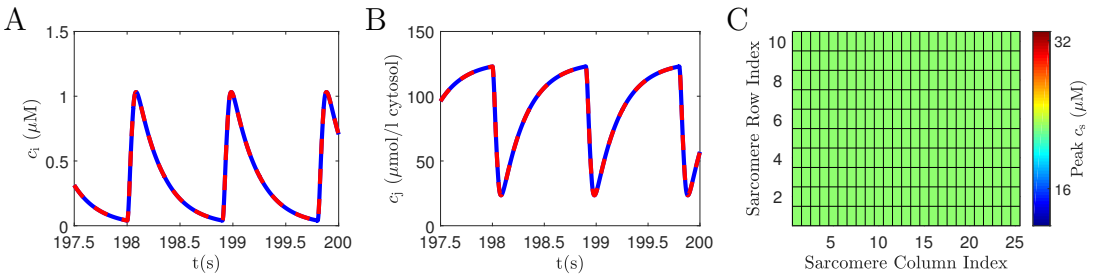

Figure 3.16: Simulation results from a network purely coupled through the cytosol such that the synchronised single period orbit is stable. The network consists of 250 sarcomeres purely coupled through the cytosol with $T_p = 0.9$ s and the coupling parameter $\tau_c = 5$ s. Plots showing the trajectories of (A) bulk cytosolic Ca^{2+} concentration and (B) SR Ca^{2+} concentration of two neighbouring sarcomeres (blue representing one sarcomere and the dashed red the other) in a 2D network. (C) Plot showing the peak subsarcolemmal Ca^{2+} concentrations during one pacing period within this 250 sarcomere network, with the plot also showing the shape of the network. All other parameters as in Appendix A.

which peak, high or low, they are reaching during their period-double orbit. This all alludes to spatial alternans arising in the system due to an increase in coupling strength through a period-doubling bifurcation in much the same way as we saw in a 1D network. Another similarity we see to that within the one-dimensional network are the effects of the boundary conditions. Again, we see closer to the borders of the myocyte that the amplitude of the spatial alternan is much smaller compared to those towards the centre of the myocyte. Thus, as with 1D systems, the resultant spatial pattern after bifurcation is dictated by the balance between the coupling strength and boundary conditions. Again, we performed stability analysis on the system, as shown in Figure 3.18, to help us support this claim.

Looking at the placement and changes in eigenvalues between Figure 3.18A and Figure 3.18B, we can see that a bifurcation has occurred. Furthermore, looking at Figure 3.18C, we can see that the single eigenvalue lying outside the unit circle in Figure 3.18B lies on the real line. This is because it has passed through the unit circle at -1, illustrating that a period-doubling bifurcation has taken place. Evidence that these are indeed spatial alternans in Figure 3.17C can be seen in the eigenvector plot in Figure 3.18D. Figure 3.18D reveals that if we perturb the orbit away from the synchronous state then the trajectories of neighbouring sarcomeres will perturb in opposing directions to one another. These opposing perturbations lead to the spatial pattern displayed in Figure

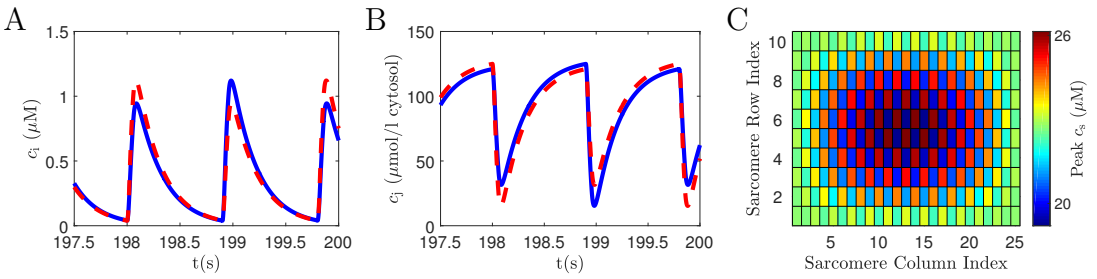

Figure 3.17: Simulation results from a network in which the synchronised single period orbit has become unstable due to an increase in the cytosolic coupling strength compared to that used to produce Figure 3.16. The network consists of 250 sarcomeres purely coupled through the cytosol with $T_p = 0.9$ s and the coupling parameter $\tau_c = 4.53$ s. Plots showing the trajectories of (A) bulk cytosolic Ca^{2+} concentration and (B) SR Ca^{2+} concentration of two neighbouring sarcomeres (blue representing one sarcomere and the dashed red the other) in a 2D network. (C) Plot showing the peak subsarcolemmal Ca^{2+} concentrations during one pacing period within this 250 sarcomere network, with the plot also showing the shape of the network. All other parameters as in Appendix A.

3.17C.

A comparison of Figures 3.17C and 3.18D reveal again how useful the stability analysis can be for the onset of spatial alternans. Figure 3.18D further demonstrates the ability of the eigenvector to predict the spatial pattern at the onset of a bifurcation to the system.

As with the 1D case we have developed a relationship linking the coupling strength and the critical pacing period at which a period-doubling bifurcation takes place leading to spatial alternans. This relationship is depicted through the plot in Figure 3.19. The colours and labels have the same representation as used in Figure 3.9. As Figure 3.19 reveals the shape of the plot is of the same form as that in Figure 3.9, and contains similar behaviours for very weak and very strong coupling. Interestingly though, it shows how for all coupling strengths the critical pacing period increases compared to the 1D network. This tells us that by simply moving from a 1D network, where the majority of sarcomeres are coupled to two other sarcomeres, to a 2D network, where the majority are now coupled to four other sarcomeres, we have decreased the strength of coupling needed within the system to cause spatial alternans. This suggests that the number of connections each sarcomere has can have an effect on the stability of the system.

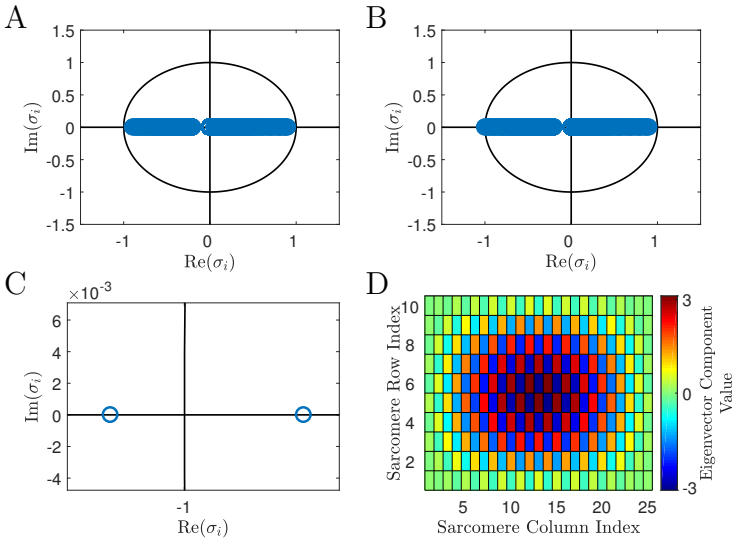

Figure 3.18: Stability analysis output for the systems the produced the results seen in Figures 3.16 and 3.17. These systems consist of a network of 250 sarcomeres purely coupled through the cytosol with $T_p = 0.9$ s and either $\tau_c = 5$ s (A) or $\tau_c = 4.53$ s (B,C,D). Plots showing the eigenvalues for coupling strengths of $\tau_c = 5$ s (A) and $\tau_c = 4.53$ s (B,C) along with a plot (D) of the values of the components in the unstable eigenvector related to the the subsarcolemmal Ca^{2+} concentrations. All other parameters as in Appendix A.

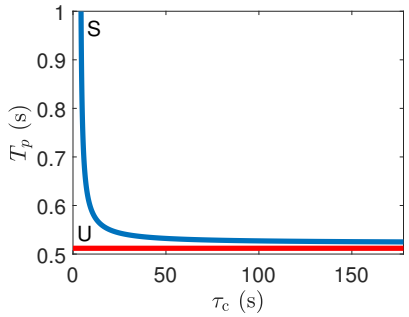

Figure 3.19: Plot showing how the cytosolic coupling strength (τ_c) affects the value of the critical pacing period (T_p) at which a period-doubling bifurcation of the synchronised single-period orbit occurs (blue line) in a 2D network containing 250 sarcomeres. The synchronised single-period orbit is stable in the region labelled S and unstable in the region labelled U. The red line marks the critical pacing period where the uncoupled case undergoes a bifurcation. All other parameters as in Appendix A.

3.4.2 Sarcoplasmic Reticulum Coupling In A Two-Dimensional Network

Moving on to coupling purely through the SR, we find the behaviour of the system similar to that of the 1D system. Figures 3.20 and 3.21 display the results of two different simulations of the system when the sarcomeres are coupled purely through the SR. It must be noted that at a 2D level some studies have suggested that diffusion in the SR may not be completely homogeneous and that diffusion in the transversal direction may be faster than in the longitudinal [103]. However for the purposes of this thesis we shall consider homogenous diffusion only, whilst the effects of inhomogeneous diffusion could be an avenue for future research.

Figure 3.20 reveals that once again the trajectories follow that of a single period orbit under weak coupling. Figure 3.20C also portrays the common theme that this trajectory is synchronous across all sarcomeres. Additionally, we once again find that the orbit that each sarcomere takes in this stable synchronous state is the same as that of the uncoupled sarcomere under the same pacing period.

Figure 3.21 illustrates the behaviour of the 2D network with just SR coupling, when the coupling is strong enough such that the synchronous single-period orbit becomes unstable. As seen in in the one-dimensional case in Figure 3.11, when the synchronous state becomes unstable, neighbouring sarcomeres follow differing single period orbits in the same phase. Furthermore, the sarcomeres appear to follow a high-low spatial pattern in terms of their peak subsarcolemmal Ca^{2+} concentration. This implies that the effects of the '+1' bifurcation in the 2D case are similar to those in the 1D case. Moreover, we find the difference in the peak subsarcolemmal Ca^{2+} concentration between neighbouring sarcomeres decreases away from the centre of the myocyte. As discussed in Section 3.4.1 this suggests the spatial behaviour is related to the balance between the coupling strength and boundary conditions. Our stability analysis for the behaviours displayed in Figure 3.20 and Figure 3.21, the results of which can be seen in Figure 3.22, supports this theory showing how a change in the coupling strength has led to an eigenvalue passing out of the unit circle, along the real axis, in the positive x-direction. A comparison of the eigenvectors shown in Figure 3.12C and 3.22C,

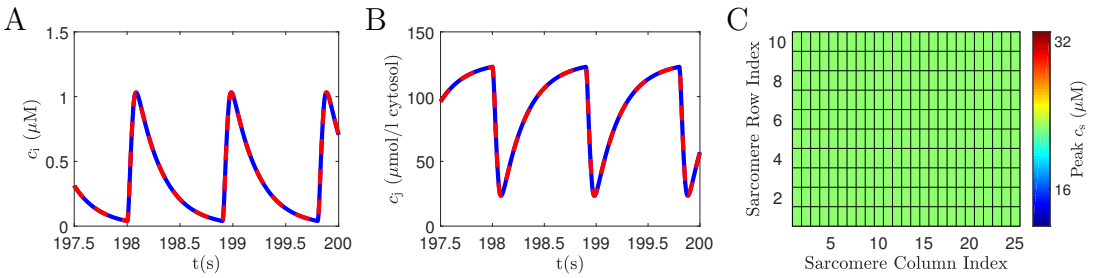

Figure 3.20: Simulation results from a network purely coupled through the SR such that the synchronised single period orbit is stable. The network consists of 250 sarcomeres purely coupled through the SR with $T_p = 0.9$ s and the coupling parameter $\tau_{\text{sr}} = 26$ s. Plots showing the trajectories of (A) bulk cytosolic Ca^{2+} concentration and (B) SR Ca^{2+} concentration of two neighbouring sarcomeres (blue representing one sarcomere and the dashed red the other) in a 2D network. (C) Plot showing the peak subsarcolemmal Ca^{2+} concentrations during one pacing period within this 250 sarcomere network, with the plot also showing the shape of the network. All other parameters as in Appendix A.

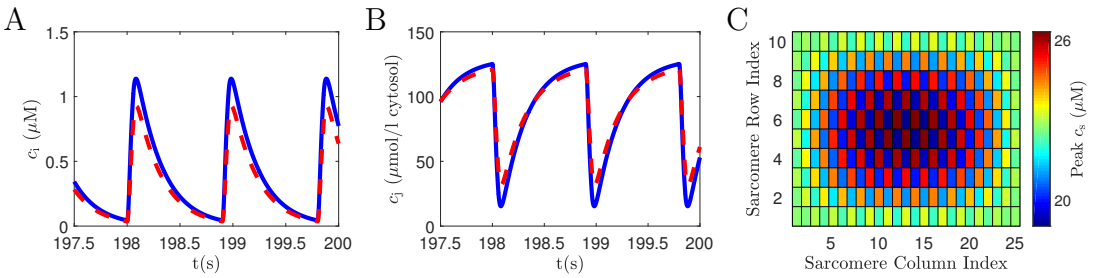

Figure 3.21: Simulation results from a network in which the synchronised single period orbit has become unstable due to an increase in the SR coupling strength compared to that used to produce Figure 3.20. The network consists of 250 sarcomeres purely coupled through the SR with $T_p = 0.9$ s and the coupling parameter $\tau_{\text{sr}} = 25.3$ s. Plots showing the trajectories of (A) bulk cytosolic Ca^{2+} concentration and (B) SR Ca^{2+} concentration of two neighbouring sarcomeres (blue representing one sarcomere and the dashed red the other) in a 2D network. (C) Plot showing the peak subsarcolemmal Ca^{2+} concentrations during one pacing period within this 250 sarcomere network, with the plot also showing the shape of the network. All other parameters as in Appendix A.

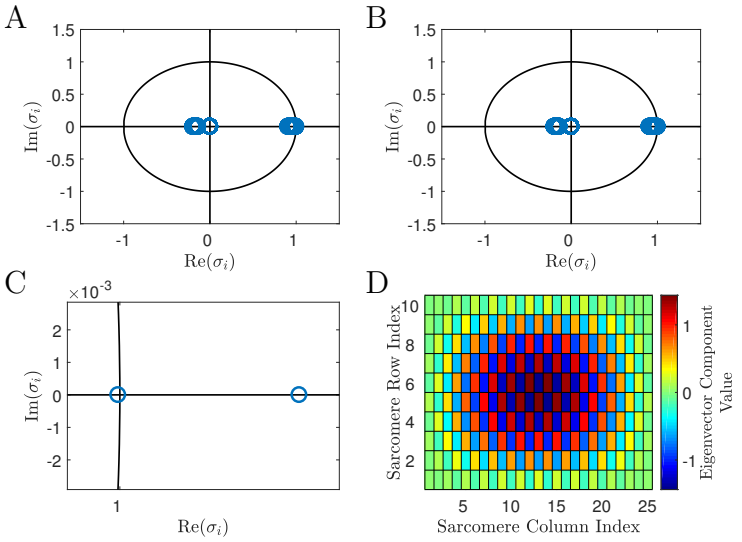

Figure 3.22: Stability analysis output for the systems the produced the results seen in Figures 3.20 and 3.21. These systems consist of a network of 250 sarcomeres purely coupled through the SR with $T_p = 0.9$ s and either $\tau_c = 26$ s (A) or $\tau_c = 25.3$ s (B,C,D). Plots showing the eigenvalues for coupling strengths of $\tau_{sr} = 26$ s (A) and $\tau_{sr} = 26.3$ s (B,C) along with a plot (D) of the values of the components in the unstable eigenvector related to the the subsarcolemmal Ca^{2+} concentrations. All other parameters as in Appendix A.

further shows the form of bifurcation is the same in both 1D and 2D networks.

Following on from this, we develop a plot to show how the critical pacing period at which a bifurcation takes place within the system is affected by the strength of the coupling through the SR. The result of this can be seen in Figure 3.23. The blue line, red line and letters S and U represent the same parts as used for Figure 3.13.We previously saw that moving from a 1D network to 2D network for cytosolic coupling the shape of the plot linking the coupling strength and critical pacing period remained similar. Similarly, the general shape of the plot in Figure 3.23 linking the SR coupling strength and critical pacing period remains similar to its 1D counterpart. Furthermore, as we saw in the cytosolic case, by increasing the number of connections between the majority of sarcomeres, an instability can occur for weaker coupling strengths. We can see this by comparing the values for the coupling strength and critical pacing period on which the bifurcation plot lies compared to those in Figure 3.13.

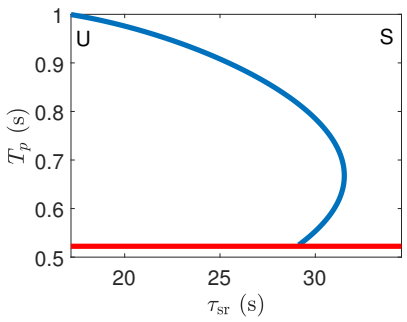

Figure 3.23: Plot showing how the SR coupling strength (τ_{sr}) affects the value of the critical pacing period (T_p) at which a '+1' bifurcation of the synchronised single-period orbit occurs (blue line) in a 2D network containing 250 sarcomeres. The synchronised single-period orbit is stable in the region labelled S and unstable in the region labelled U. The red line marks the critical pacing period where the uncoupled case undergoes a bifurcation. All other parameters as in Appendix A.

3.4.3 Joint Coupling In A Two-Dimensional Network

As in Section 3.3.2, we developed a contour plot between the both coupling strengths and the critical pacing period for a bifurcation of the synchronised single-period orbit. This is depicted in Figure 3.24. Once again, no new forms of bifurcations occur, just the two already discussed. As with the 1D network the type of bifurcation under which the synchronised single-period orbit loses stability is dictated by the dominant form of coupling. Moreover, as in the 1D case a region of stability, labelled S in Figure 3.24, lies between the two different form of bifurcation.

The plots in Figure 3.24 depict similar patterns to their 1D counterparts. This includes a carry over of the behaviour looked at in Figure 3.14B for a '+1' bifurcation to occur when cytosolic coupling is weak. The key difference comes in the range of the coupling strengths. As with the purely SR and cytosolic coupled case, the plots for a '+1' bifurcation and a period-doubling bifurcation under joint coupling reveal that an increase in the number of coupling connections has decreased the coupling strengths needed to cause a bifurcation.

Now comparing Figure 3.24 with Figure 3.14, we see small differences between the 1D and 2D case for both bifurcations to occur. As in the one-dimensional case where the cytosolic coupling is weak, for all pacing periods shown the SR coupling can be weak. Furthermore, for weak cytosolic coupling the SR coupling strength needed can be weaker for a +1 bifurcation to occur in the 2D case.

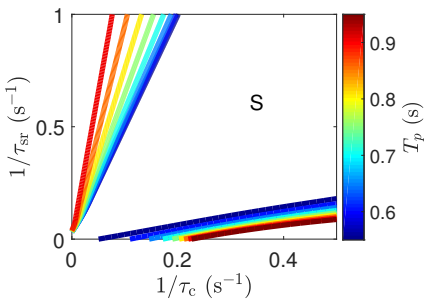

Figure 3.24: Contour plot showing the values of the critical pacing period (T_p), cytosolic coupling strength (τ_c) and SR coupling strength (τ_{sr}) that can lead to a bifurcation of the synchronised state in a 2D network containing 250 sarcomeres. The plot shows the values for both a '+1' bifurcation (Plots stemming from the y-axis) or a period-doubling bifurcation (Plots stemming from the x-axis). Note on the axes we have used $1/\tau_c$ and $1/\tau_{sr}$ so we can see the effect of weak coupling. S labels the region in which the synchronised state is stable. All other parameters as in Appendix A.

On the other hand, as we begin to increase the cytosolic coupling strength, the increase needed in the SR coupling strength to maintain the '+1' bifurcation is proportionally much greater. As we reach strong cytosolic coupling strengths the shape of the contours for a '+1' bifurcation appears to align with that of the one-dimensional case.

Combining our findings across both 1D and 2D networks it is clear that diffusion between sarcomeres can cause a bifurcation to the synchronised single-period orbit. We have seen that the type of bifurcation that occurs is dictated by which form of coupling is dominant. Furthermore we have found that by increasing the strength of the non-dominant coupling, a proportionally steeper increase in the dominant coupling strength is needed to maintain the bifurcation. In the case of a '+1' bifurcation, we have seen a more nuanced role of the pacing period. Our studies have revealed that when SR coupling is dominant and both coupling strengths are weak, we have a region of bistability where some of the fastest pacing periods require stronger coupling through the SR for a '+1' bifurcation compared to some slower pacing periods. However, when both coupling strengths are increased this area of bistability is lost and an increase in pacing period will consistently need an increase in the SR coupling strength for a '+1' bifurcation to occur.

As we saw in Section 3.2, a large decrease in uptake strength could lead to a

change in the order of the switches within the orbit. Since such changes could have a drastic change to the effect of the system at network level we have devised another contour plot similar to that in Figure 3.24, but with a reduced uptake strength of $v_{\text{up}} = 250\ \text{s}^{-1}$.

The first key thing to note is that both forms of bifurcation still occur under the new switching regime produced by the reduced uptake strength. Figure 3.25 also shows that these two bifurcations still do not coincide and that the region where the synchronised single-period orbit, labelled S, still lies between these two bifurcations. In the case of period-doubling bifurcations due to dominant cytosolic coupling we find that the reduced uptake strength has altered the dynamic between two coupling strengths and critical pacing period quite drastically. By comparing fixed values of SR coupling in Figures 3.25 and 3.24, we can that an increase in the cytosolic coupling leads a much smaller increase in the value of the critical pacing period when the uptake strength is lower.

The changes based around the onset of a '+1' bifurcation are even greater. The most notable difference is the range of pacing periods under which a '+1' bifurcation can occurs has drastically decreased. Such a decrease suggests that a '+1' bifurcation can only occur for a range of pacing periods, a possibility alluded to in Sections 3.3.1 and 3.4.2.

Another point of interest, is the behaviour found for pacing periods close to the critical pacing period for the uncoupled case when SR coupling is dominant and both forms of coupling are weak. In Figures 3.14 and 3.24, we saw that these faster pacing periods could suppress a '+1' bifurcation compared to some slower pacing periods. However, this behaviour has now been lost and the faster pacing periods promote a '+1' bifurcation when both coupling strengths are weak, as well as when they are strong. The dynamic between the uptake strength and the '+1' bifurcation shall be researched further in Section 4.2.

These findings reveal that the role of the SERCA pump in promoting instabilities is not just important at the single cell/sarcomere level. Through these comparisons of the relationships between pacing period and coupling strength for the onset of an instability to the synchronous single period state, we see that a largely reduced uptake strength not only reduces the chance of alternans in

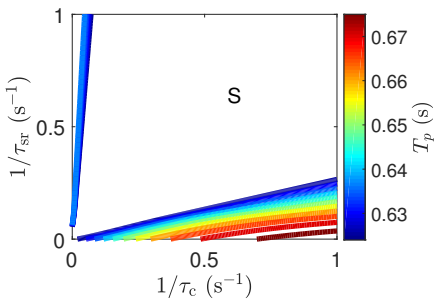

Figure 3.25: Contour plot showing the values of the critical pacing period (T_p), cytosolic coupling strength (τ_c) and SR coupling strength (τ_{sr}) that can lead to a bifurcation in a 2D network containing 250 sarcomeres and a reduced uptake strength, $v_{up} = 250$ s^{-1}. The plot shows the values for both a '+1' bifurcation (Plots stemming from the y-axis) or a period-doubling bifurcation (Plots stemming from the x-axis). Note on the axes we have used $1/\tau_c$ and $1/\tau_{sr}$ so we can see the effect of weak coupling. S labels the region in which the synchronised state is stable. All other parameters as in Appendix A.

a single sarcomere/cell but also at the network level. Thus medically reducing SERCA activity may be one avenue to help prevent cardiac alternans.

3.5 Summary

The main focus of this chapter has been around the balance between pacing period and coupling strengths. We have built upon previous work [1], on how increasing the cytosolic coupling strength can produce a period-doubling bifurcation. Furthermore, we have introduced SR coupling to the PWL Shiferaw-Karma model and revealed that when strong enough this coupling can cause a '+1' bifurcation to the synchronised single-period orbit. This '+1' bifurcation leads to new single-period orbits that vary spatially across sarcomeres.

Within this section we have seen how the stability approach described in Section 2.4 can be used to provide meaningful insights into the PWL Shiferaw-Karma model. In section 3.1 we revealed that the spatial pattern at the onset of a bifurcation due to the cytosolic coupling strength can be predicted by the eigenvector related to the eigenvalue lying outside the unit circle. Throughout the rest of Section 3 we demonstrated this predictive power for both cytosolic and SR coupling in 1D and 2D networks.

Further to this, in Section 3.1, we illustrated that these eigenvectors provided some mathematical insight into how a networks spatial pattern alters beyond

the point of bifurcation. We showed that as the cytosolic coupling strength is increased further, more eigenvalues are pushed outside the unit circle. This in turn brings further eigenvectors into play, each affecting the spatial pattern of the alternans in the network.

Another advantage of the stability approach we have exploited in this chapter, is the ability to create plots for the value of the critical pacing period at which a bifurcation occurs against the values of some parameter within the system. In the uncoupled case these plots revealed that an increase in the release slope leads to an increase in the critical pacing period whilst the balance between the uptake strength and critical pacing period was much more dynamic. We found both a very high and very low uptake strength could suppress alternans. In Section 3.2.1 we discussed that when the uptake strength is low enough it limited steep calcium release from the SR by keeping the SR Ca^{2+} concentration low. It is this mechanism that allows low uptake strength to suppress alternans. On the other hand, a large enough uptake strength allowed the SR Ca^{2+} concentration to be fully replenished at faster pacing periods despite steep calcium release.

In networks of sarcomeres, the relationships developed between the critical pacing periods and each form of coupling were very different. The relationship between the cytosolic coupling strength and length of the critical pacing period was proportional. Also, in general, an increase in the SR coupling strength meant an increase in the critical pacing period length. However, unlike with cytosolic coupling, we found that if we weaken the SR coupling strength enough we found there was no critical pacing period at which a '+1' bifurcation would occur. Moreover we found that if we increase the SR coupling strength from the earliest point at which this occurs, the critical pacing period would also decrease as well as increase suggesting a form of bistability. Finally, we found that the area of bistability could be reduced or lost by either increasing the cytosolic coupling strength when the network was jointly coupled or decreasing the uptake strength. We seek to understand the role of diffusive coupling in a network of sarcomeres further in the following chapter.

4 New Spatial Patterns After Bifurcation

In Section 3 we established that an increase in the SR coupling strength can cause the network's synchronous orbit to become unstable through a '+1' bifurcation. As seen in Figures 3.11 and 3.21, this '+1' bifurcation causes neighbouring sarcomeres to follow different single period orbits. The plots between the SR coupling strength and critical pacing period for this bifurcation shown in Figures 3.13 and 3.23 also revealed a bistability for some weaker coupling strengths. These plots, along with the contour plot in Figure 3.25, suggested that at slow enough pacing periods such a bifurcation may not occur. In Section 4.1 we study the area of bistability and try to understand why it exists. In Section 4.2 we extend the plot in Figure 3.23 across stronger SR coupling strengths to confirm whether there is a maximum critical pacing period at which a '+1' bifurcation takes place. Furthermore, we consider whether the behaviour of the system once the '+1' bifurcation occurs remains the same as that seen in Section 3.4.2 for these stronger coupling strengths.

Calcium alternans have been shown to display a varied number of spatial patterns within myocytes, with some patterns such as SDA having stronger links to pathological conditions than others [106, 107]. In Section 4.3 we extend our studies on networks with coupling through both the SR and cytosol. Through these studies we find new types of spatial patterns at the point of bifurcation due to changes in the values of both coupling strengths. We also expand on the balance between the values of the two coupling strengths and the critical pacing period at which both a '+1' and '-1' bifurcations take place. This informs us whether there are limits to the coupling strengths that allow for these bifurcations to occur.

SDA and other regional mismatches in calcium alternans at the subcellular level have been deemed potentially arrhythmogenic as opposed to SCA [15]. This means that should SCA already exist, it is important to understand any mechanism that could cause SCA to transform into a more spatially varied spatial pattern. In Section 4.4 we study networks at pacing periods such that the uncoupled system has a period-doubled orbit. We study both the case when cytosolic Ca^{2+} diffusion is dominant and when SR Ca^{2+} diffusion is dominant, using the same

approaches we have used at pacing-periods where the synchronised single-period orbit was stable under balanced coupling. We use the term balanced coupling to refer to the situation where the two forms of coupling, SR and cytosolic, have coupling strengths such that the system has a synchronised state.

Section 4.5 contains a study of the behaviours discussed in this chapter and in Section 3 within the context of the original Shiferaw-Karma model. By doing this we aim to understand how the switch between a smooth and PWL approach may alter the onset of a bifurcation. Furthermore we briefly discuss how buffering may have the potential to alter the onset of a '+1' bifurcation. Section 4.6 contains a summary of this chapter.

4.1 The Critical Pacing Period Against Weaker Coupling Strengths

One of the key features of the plot seen in Figures 3.13 and 3.23 is that for some pacing periods the coupling strength through the SR needed to be increased for a bifurcation to occur when compared to some other, slower pacing periods. In turn this created an area of bistability. Here we shall seek to try and understand this behaviour in more detail. To begin with we will consider how the orbit of a 2D network of sarcomeres purely coupled through the SR with fixed coupling strength changes as we increase the pacing period.

Figure 4.1A is a scatter plot of the largest and smallest values of the peak subsarcolemmal Ca^{2+} concentrations from the orbits of sarcomeres in a 2D network against the pacing period. Figure 4.1B contains the critical pacing periods at which a '+1' bifurcation occurs against the values of the SR coupling strength from Figure 3.23 that we are currently considering. The arrow in Figure 4.1B lies across the pacing periods we investigate at the value of the fixed coupled strength $\tau_{\text{sr}} = 31.519$ s and defines the direction in which we changed the pacing periods.

A comparison of Figures 4.1A and 4.1B illustrates the region where the synchronised single-period orbit is stable and the peak subsarcolemmal Ca^{2+} concentrations across the network are equal. This is demonstrated in Figure 4.1A by how the difference between the largest and smallest peak subsarcolemmal Ca^{2+} concentrations change with the pacing period. As we can see these two values

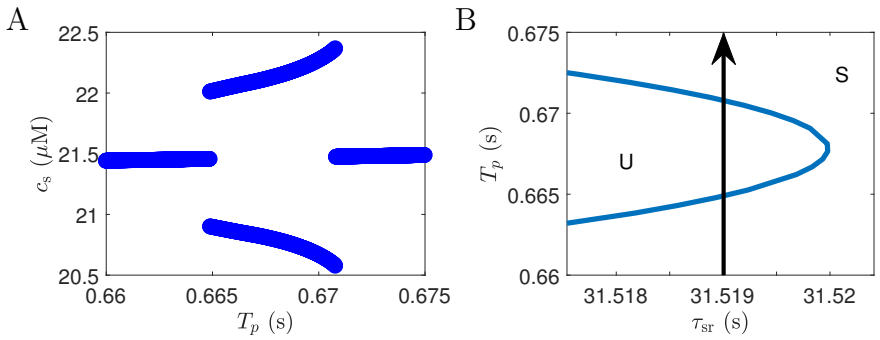

Figure 4.1: Plots studying the region of bistability originally seen in Figure 3.23. Scatter plot (A) of the largest and smallest peak values of all the sarcomeres subsarcolemmal Ca^{2+} concentrations against the pacing period (T_p) from simulations based on a network of 250 sarcomeres coupled purely through the SR with coupling strength $\tau_{sr} = 31.519$ s. (B) Plot of the values of the critical pacing period T_p for which a '+1' bifurcation occurs against the coupling strength τ_{sr}. The region labelled by S is where the synchronised single-period orbit is stable whilst it is unstable in the region labelled as U. The arrow marks the direction we vary the pacing periods in. All other parameters as in Appendix A.

are equal for pacing periods where the synchronised single-period orbit is stable. However, in the region where the synchronised single-period orbit is unstable new single-period orbits form which vary between sarcomeres. This is shown in Figure 4.1A as the largest and smallest peak subsarcolemmal Ca^{2+} concentrations quickly diverge when we enter the region where the synchronised single-period orbit becomes unstable. Furthermore, as we increase the length of the pacing period, Figure 4.1A reveals that the difference between the largest and smallest synchronised single-period orbit also increases. Then these two values sharply equalise as we cross back into the region where the synchronised single-period orbit is stable again.

Figure 4.1A also demonstrates that as we increase the pacing period when the synchronised single-period orbit is stable, the peak subsarcolemmal Ca^{2+} concentration also marginally increases. As we saw in Section 3.2.1 the shape of the trajectories depend heavily on the uptake strength. Combining this information along with the changing peak values in 4.1A suggests that the shape of the trajectory could have an affect on the observed bistability. To test this we have generated further plots to compare how the values of the SR coupling strength and critical pacing period for a '+1' bifurcation alter as we vary the uptake strength, the results of which can be seen in Figure 4.2.

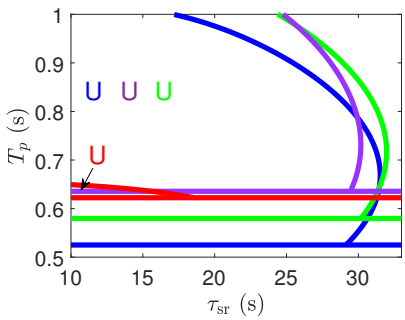

Figure 4.2: Comparison of how the SR coupling strength (τ_{sr}) and uptake strength (v_{up}) affects the critical pacing period (T_p) for a '+1' bifurcation of the synchronised state in 2D networks. The uptake strengths are $v_{up} = 405$ s^{-1} (blue plots and U), $v_{up} = 350$ s^{-1} (green plots and U), $v_{up} = 300$ s^{-1} (purple plots and U) and $v_{up} = 250$ s^{-1} (red plots and U). The horizontal plots represent the pacing period at which the uncoupled case undergoes a bifurcation. The letter U marks the region where the synchronised state is unstable due to a '+1' bifurcation. All other parameters as in Appendix A.

In Figure 4.2 we plot the values of the critical pacing period at which a '+1' bifurcation occurs against the coupling strength τ_{sr} for a variety of uptake strengths. A comparison of the plots for the uptake strengths $v_{up} = 405$ s^{-1} (blue) and $v_{up} = 350$ s^{-1} (green) shows little qualitative difference in the shape of the plots, whilst the plot for the uptake strength $v_{up} = 300$ s^{-1} (purple) depicts a small decrease in the area of bistability. On the other hand the plot for the uptake strength $v_{up} = 250$ s^{-1} (red) demonstrates that the area of bistability has been lost. We already know that a decrease in the uptake strength leads to a decrease in the maximum concentration of Ca^{2+} in the SR. Furthermore, as discussed in Section 3.2.1, when the uptake strength is decreased enough, steep release from the load-release function does not occur at the beginning of the pacing period due to a significant decrease in the SR Ca^{2+} concentration. Thus the plot related to the uptake strength $v_{up} = 250$ s^{-1} implies that for a region of bistability to exist, steep release must occur at the start of the pacing period. Combining these observations suggests that the area of bistability is linked to both the behaviour of the SERCA pump and load-release function. This link includes a particularly influential role from the amount and timing of steep release from the load-release function.

4.2 Extending The Relationship Between Pacing Period And The Sarcoplasmic Reticulum Coupling Strength

As we saw from the plots in Figures 3.13 and 3.23 the relationship between the critical pacing period and the coupling strength τ_{sr} for a '+1' bifurcation suggests that there comes a point where the voltage is paced slowly enough that no such bifurcation can take place, no matter the strength of the SR coupling. Further evidence comes from the plots of the values of the critical pacing period and the strength of both forms of coupling at which a '+1' bifurcation occurs shown in Figure 3.25. Figure 3.25 revealed that only a limited number of pacing periods appear to allow for a '+1' bifurcation. Now we developed the plot between the values of the critical pacing period and the strength of both forms of coupling at which a '+1' bifurcation occurs in Figure 3.25 such that the synchronous orbit's switching events had the same order as those seen in Figure 3.7B. On the other hand, the plot in Figure 3.23 was based around a synchronous orbit with switching events in the same order as those in Figure 3.7A. To see whether the order of switching events seen in Figure 3.7A also limits the number of pacing periods that allow a '+1' bifurcation, we have extended Figure 3.23 to cover stronger coupling strengths through the SR. The extension covers stronger SR coupling and can be seen in Figure 4.3.

Figure 4.3A reveals that there are pacing periods slow enough such that a '+1' bifurcation cannot be caused by pure SR coupling. In turn, we know this means there are pacing periods where '+1' bifurcations cannot occur under joint coupling with dominant SR coupling either. We can infer this as our studies into joint coupling have shown that all the contour plots showing when a '+1' bifurcation occurs due to dominant SR coupling stem from the values at which a '+1' bifurcation occurs in a network purely coupled through the SR. A further revelation from Figure 4.3B is that under exceptionally strong SR coupling the synchronous single-period orbit is stable. Simulations at such strong coupling strengths confirm such behaviour. This agrees with a study by Picht *et al* [108] in which they find that fast Ca^{2+} SR diffusion helps to maintain a homogenous Ca^{2+} SR concentration distribution by minimising the difference in gradient between the network SR concentration and JSR concentration. In terms of our model,

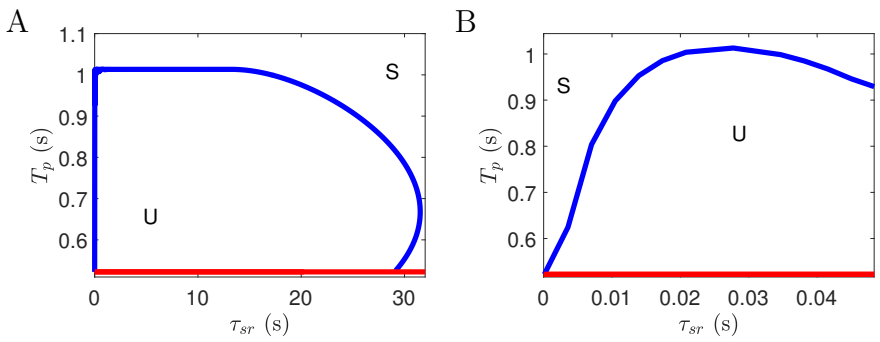

Figure 4.3: An extension of the plot in Figure 3.23. (A) Plot covering all values of the coupling parameter τ_{sr} that allow for a '+1' bifurcation. (B) A closer look at the left hand side of plot (A). The synchronised single-period orbit is stable in the region labelled S and unstable in the region labelled U. The red line marks the critical pacing period where the uncoupled case undergoes a bifurcation. The network contains 250 sarcomeres and all other parameters as in Appendix A.

by minimising this difference the release from the load-release function remains consistent across sarcomeres. This prevents spatial variation in the cytosolic concentrations that could lead to the behaviour associated with a '+1' bifurcation.

From our findings here, along with those in Section 3.4.3, it is apparent that the uptake strength has an effect on the range of pacing periods that the synchronous single-period orbit can undergo a '+1' bifurcation. By finding the maximum critical pacing period at which a '+1' bifurcation of the synchronous single-period orbit occurs we can develop an understanding on how the uptake strength value affects the size of the range of critical pacing periods at which a '+1' bifurcation can take place. A plot showing this can be seen in Figure 4.4.

Looking at the plot in Figure 4.4 for uptake strengths approximately above 330 s^{-1} we see that the width of the range of critical pacing periods slowly decreases as the uptake strength increases. This suggests that the onset of a '+1' bifurcation has a link to how quickly the SR Ca^{2+} concentration can be refilled since increased uptake strength decreases the period of time needed for the steady state to be reached. On the other hand, when considering values of uptake strength below 330 s^{-1} we see that this range sharply decreases. This is likely due to the now highly restricted amount of steep release in the load-release function which in turn means the SR can be replenished quickly despite the lower uptake strengths. Furthermore, we see that as the uptake strength reaches values where steep release from the load-release function no longer occurs at the beginning of

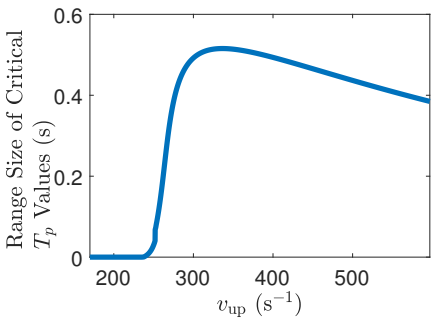

Figure 4.4: A plot showing the width of the range of pacing periods that allow for a '+1' bifurcation as a function of the uptake strength v_{up} in a network of 250 sarcomeres purely coupled through the SR. All other parameters as in Appendix A.

the pacing period, the width of the range approaches zero showing the importance of immediate SR release to a '+1' bifurcation. In fact we found that a '+1' bifurcation did not occur when steep release from the load-release function did not occur. This happens when both the value of the uptake strength is low and the pacing period slow. These findings reveal how a '+1' bifurcation is closely tied to the balance between SR release, SERCA pump activity and the length of the pacing period.

Now we move our attention back to the shape of the plot between the critical pacing period and the coupling strength τ_{sr} for a '+1' bifurcation illustrated in Figure 4.3. A look around the slowest pacing period at which a '+1' bifurcation takes place suggests this pacing period is fixed for a range of SR coupling strengths. However, Figure 4.5, which takes a close look at these slower pacing periods, tells a very different story. It focuses on the slower critical pacing periods and the coupling strength τ_{sr} for a '+1' bifurcation at both ends of the apparent horizontal line in Figure 4.3. As we can see, this line is not horizontal at all but a string of varying sized bumps. These bumps occur for the length of what originally appeared to be a horizontal line for coupling strengths lying between those displayed in Figures 4.5A and 4.5B.

These bumps reveal a very intricate relationship between the slower pacing periods and the coupling strength. They imply that at some fixed pacing period a '+1' bifurcation may not occur for a specific SR coupling strength but either an increase or decrease of the SR coupling strength could cause a '+1' bifurcation. Simulations ran between these bumps agree with the stability analysis that the

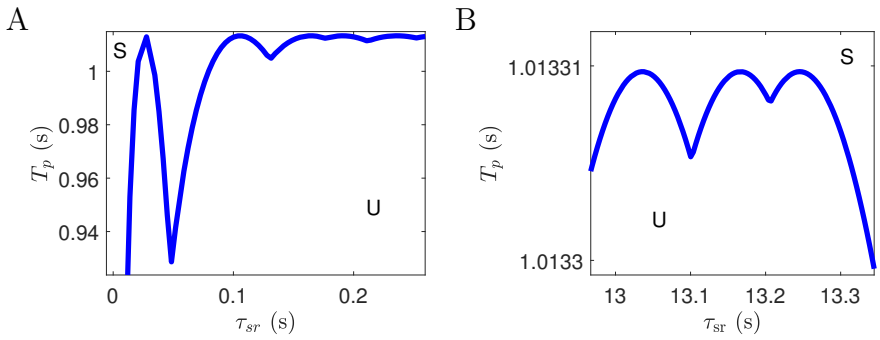

Figure 4.5: Plots revealing bumps along the top of the plot seen in Figure 4.3. A closer look towards the left hand side (A) and right hand side (B) of the plot in Figure 4.3 revealing the complexities of the balance between the values of the coupling strength τ_{sr} and the slower critical pacing periods (T_p) that leads to a '+1' bifurcation. All other parameters as in Appendix A.

synchronous single-period orbit is stable in these regions. On the other hand, simulations ran just inside these bumps reveal varying spatial patterns. We will discuss the behaviour within these bump in more detail within Section 4.2.1.

Whilst the size of these bumps remains small, such as those seen in Figure 4.5B, Figure 4.5A reveals an outlier. The area between the two bumps for the strongest coupling strengths at which a '+1' bifurcation takes place is significantly larger than any of the other gaps between the bumps and simulations performed within this show agreement with theory.

4.2.1 Changes In The Leading Eigenvector

As seen in Figure 4.5, the shape of the plot describing the values of the critical pacing period and τ_{sr} at which a '+1' bifurcation occurs is quite complex. We have already discussed that in the gaps between these bumps the synchronous single-period orbit is stable. However, the behaviours that emerge as the system is pushed into these bumps are even more interesting. To illustrate this, in Figures 4.6, 4.7 and 4.8 are the results of stability analysis and simulations of three different system set-ups. Each system set-up uses a pacing period and coupling strength that lies just within a bump in Figure 4.5. The set-ups differ such that each simulation relates to a different bump.

Our first example, displayed in Figure 4.6, focuses on the middle bump shown in Figure 4.5B. For context, the bump to the right of this relates to the behaviour seen in Figure 3.21. As Figure 4.6A and Figure 4.6B demonstrate, the stability

analysis shows that a '+1' bifurcation has occurred but the resulting spatial pattern is different to that observed previously. The simulation result in Figure 4.6C shows behaviour consistent with theoretical predictions.

The behaviour portrayed in Figure 4.6C is similar to that seen in 3.21C with neighbouring sarcomeres having different peak subsarcolemmal Ca^{2+} concentrations. Studies of individual trajectories within the system show they still have single-period orbits as before but that the placement of these trajectories in relation to one another has changed. Whilst the pattern we have seen before had the difference in peak subsarcolemmal Ca^{2+} concentration between neighbouring sarcomeres largest at the cell centre, we now have two separate locations where this largest difference occurs away from the centre. This behaviour further changes as we study the next bump. This results of this study are combined in Figure 4.7.

The stability analysis and simulation behaviour seen in Figure 4.7 relates to the case where we move from the region when the synchronous single period orbit is stable into the left most bump seen in Figure 4.5B. As revealed the behaviour has once again slightly changed, with the locations of the biggest differences increasing to three and slightly shifting once more compared to Figure 4.6. Despite these changes in spatial patterning, the individual sarcomere behaviour once the synchronised single-period orbit goes unstable is always that of a new single-period orbits. We find this to be the case for all the bumps suggesting that, despite the changes in spatial patterning, a '+1' bifurcation of the synchronous single-period orbit always produces a network containing multiple single-period orbits. The changes in spatial patterning reveal how alterations in the strength of SR coupling can produce more complex patterns. This is made even clearer when looking at the behaviour in Figure 4.8. This behaviour relates to the furthest left bump seen in Figure 4.5A.

Whilst Figures 3.21, 4.6 and 4.7 seem to suggest a developing pattern in how the spatial behaviour at the onset of the '+1' bifurcation can be slightly altered by the strength of coupling, Figure 4.8 shows a marked difference. Instead of a pattern centred around points in the myocyte where neighbouring sarcomeres have the biggest difference in peak subsarcolemmal Ca^{2+} concentration, the

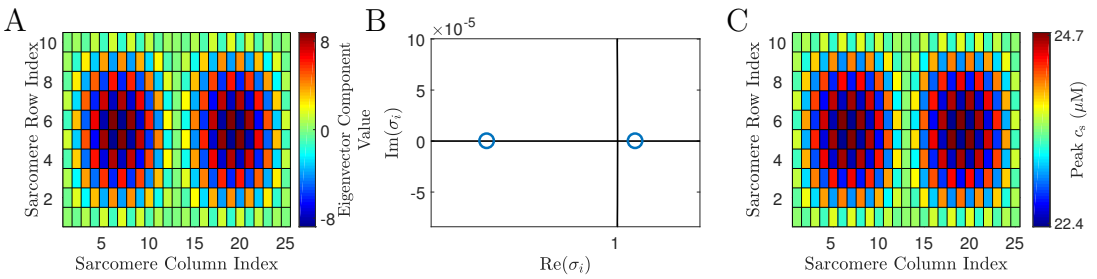

Figure 4.6: Simulation and stability analysis of a system with values of the pacing period and SR coupling strength contained within the central bump of Figure 4.5B. The systems consists of a network of 250 sarcomeres. Plots of the values of the components in the unstable eigenvector related to the the subsarcolemmal Ca^{2+} concentrations in each sarcomere(A), eigenvalues of the system close to the boundary of interest (B) and the peak Ca^{2+} subsarcolemmal concentrations during a single pacing period from a simulation (C). Key parameter values are a pacing period $T_p = 1.013309$ s and a coupling parameter of $\tau_{\text{sr}} = 13.18$ s. All other parameters as in Appendix A.

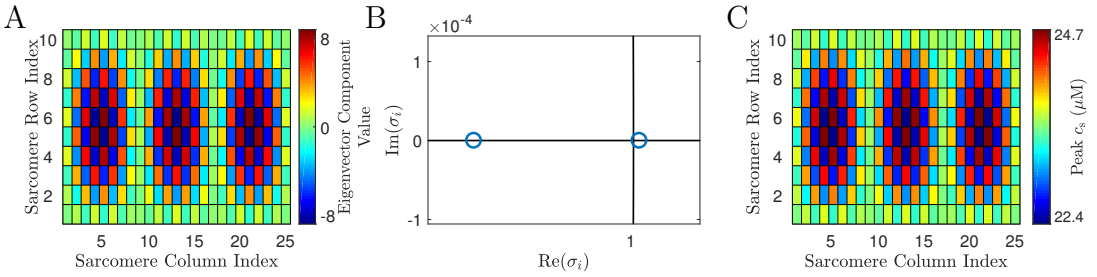

Figure 4.7: Simulation and stability analysis of a system with values of the pacing period and SR coupling strength contained within the left hand bump of Figure 4.5B. The systems consists of a network of 250 sarcomeres. Plots of the values of the components in the unstable eigenvector related to the the subsarcolemmal Ca^{2+} concentrations in each sarcomere(A), eigenvalues close to the either side of the boundary of interest (B) and the peak Ca^{2+} subsarcolemmal concentrations during a single pacing period from a simulation (C). Key parameter values are a pacing period $T_p = 1.013309$ s and a coupling parameter of $\tau_{\text{sr}} = 13.05$ s. All other parameters as in Appendix A.

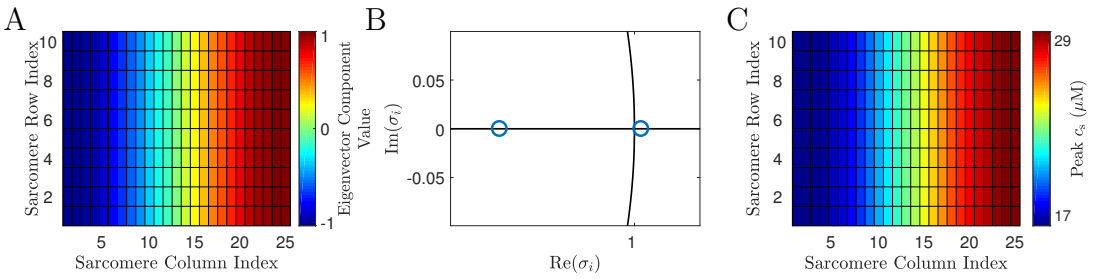

Figure 4.8: Simulation and stability analysis of a system with values of the pacing period and SR coupling strength contained within the left hand bump of Figure 4.5A. The systems consists of a network of 250 sarcomeres. Plots of the values of the components in the unstable eigenvector related to the the subsarcolemmal Ca^{2+} concentrations in each sarcomere(A), eigenvalues close to the either side of the boundary of interest (B) and the peak Ca^{2+} subsarcolemmal concentrations during a single pacing period from a simulation (C). Key parameter values are a pacing period $T_p = 0.9$ s and a coupling parameter of $\tau_{\text{sr}} = 0.0108$ s. All other parameters as in Appendix A.

biggest difference now comes from comparing the two far edges of the cell. By comparing each change in the behaviour at the onset of the '+1' bifurcation, it becomes apparent that this is not the result of a gradual change in the leading eigenvector, but a more drastic one when going from bump to bump. As we move across all the bumps we find small groups with similar patterns such as those in Figures 3.21, 4.6 and 4.7. However, every once in a while there will be a much more dramatic shift in the pattern. One of these major changes is portrayed in Figure 4.9. Both Figures 4.9A and 4.9B inform us that these spatial patterns can change drastically due to small changes in the coupling strength but, thanks to the PWL approach, we are able to predict such drastic changes.

These changes beg the question whether at a macroscopic level certain groups of patterns can be more heavily linked to pathological conditions, compared to others, particularly as the overall calcium concentrations within the myocyte appear unaffected. In both experimental and modelling studies [109, 110] higher concentrations of Ca^{2+} in the SR have been linked to spontaneous calcium release. Spontaneous release has been linked to DADs which can lead to arrhythmic behaviours [111]. A study by Schlotthauer and Bers [86] revealed that for these DADs to be strong enough to potentially cause arrhythmic conditions, multiple regions of the myocyte need to have spontaneous synchronous Ca^{2+} release. Our findings reveal that changes in the strength of Ca^{2+} diffusion in the SR lead to

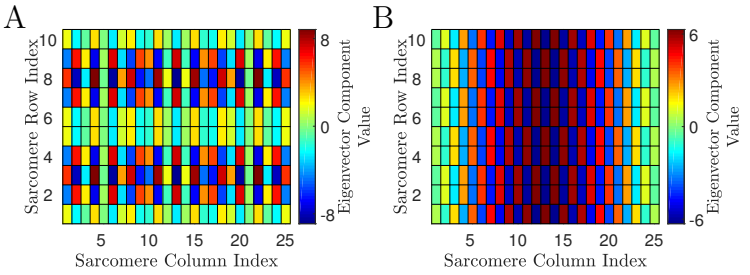

Figure 4.9: A comparison of the single unstable eigenvector from two systems, each consisting of a network of sarcomeres purely coupled through the SR with a slightly different coupling strength. Plots of the values of the components in the unstable eigenvector related to the the subsarcolemmal Ca^{2+} concentrations in each sarcomere with $T_p = 1.013309$ s and a coupling parameter of $\tau_{sr} = 10.08$ s (A) and $\tau_{sr} = 10.04$ s (B). The network contains 250 sarcomeres and all other parameters as in Appendix A.

such regional distributions in high Ca^{2+} concentrations which could potentially cause spontaneous synchronous Ca^{2+} release.

Although in general the behaviour at the onset of instability within the synchronised single-period orbit can be predicted due to a single eigenvalue leaving the unit circle, there are behaviours that can be linked to degenerate eigenvalues lying outside the unit circle. Figure 4.10 depicts the results of a simulation that has apparent degeneracy. As we can see from Figure 4.10A the synchronous single-period orbit has lost stability producing a new spatial pattern. This spatial pattern is due to a '+1' bifurcation, confirmed in the eigenvalue plot in Figure 4.10B, that has produced new single-period orbits that vary between sarcomeres. However, the eigenvalue plot in Figure 4.10B does not show a single eigenvalue lying outside the unit circle but two equal valued eigenvalues, implying degeneracy. We note that to find this case of degeneracy we have changed the network size to 100 sarcomeres in a square layout. We shall discuss the reasons behind this after discussing the eigenvectors displayed in Figure 4.11.

Now since we have degeneracy the system has two eigenvectors related to the eigenvalues lying outside the unit circle. These two eigenvectors are displayed in Figures 4.11A and 4.11B. Comparing these with the behaviour seen in Figure 4.10A, neither of these eigenvectors have a sole influence on the behaviour of the system after the bifurcation. On the other hand, we are able to linearly combine these two vectors in such a way that the resultant pattern, illustrated in Figure 4.11C, looks qualitatively similar to that in Figure 4.10A. This reveals that

although degeneracy makes it impossible to predict the exact spatial behaviour after a bifurcation from the eigenvectors, we know it must be some form of linear combination and therefore can deduce the sort of spatial pattern that may occur after bifurcation. Furthermore, as previously mentioned, to provide this example of degeneracy we have changed the shape of the network to that of a square. We have done this as we have found that examples of degeneracy appear to occur more regularly in networks that have a similar number of sarcomeres in both the longitudinal and transversal direction. This suggests that the shape of the network can have an influence on the spatial behaviours that occur at the onset of a bifurcation of the synchronised state.

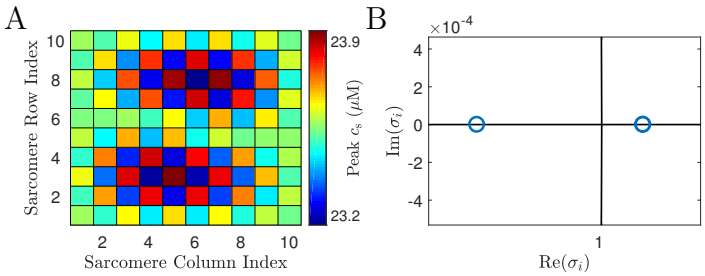

Figure 4.10: Simulation and stability analysis results of a system with a degenerate eigenvalue lying outside the unit circle. The system consists of a network of 100 sarcomeres in a 10 by 10 grid. Plot of the peak subsarcolemmal Ca^{2+} concentrations (A) during a single pacing period and the eigenvalue plot (B) of the system producing Figure 4.10A. The eigenvalue lying outside the unit circle is degenerate. Key parameter values are a pacing period $T_p = 1.01326$ s and a coupling parameter of $\tau_{\text{sr}} = 12.5$ s. All other parameters as in Appendix A.

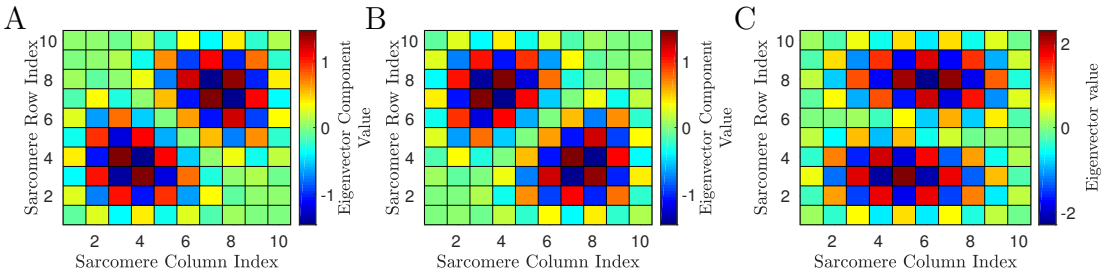

Figure 4.11: The values of the components in the unstable eigenvectors related to the the subsarcolemmal Ca^{2+} concentrations and their linear combination linked to the system used to produce Figure 4.10. The system consists of a network of 100 sarcomeres in a 10 by 10 grid. Plots of the components in the unstable eigenvector related to the subsarcolemmal Ca^{2+} concentrations (A,B) related to the eigenvalues lying outside the unit circle in Figure 4.10B and the linear combination of these eigenvectors(C) that leads to the behaviour seen in Figure 4.10A. Key parameter values are a pacing period $T_p = 1.01326$ s and a coupling parameter of $\tau_{\text{sr}} = 12.5$ s. All other parameters as in Appendix A.

4.3 Expansion Of Joint Coupling

Given the revelations found by extending the plot showing the values of the critical pacing period against τ_{sr} under which a '+1' bifurcation occurs in a network purely coupled through the SR, it stands to reason to also extend the plots between the two coupling strengths and the critical pacing period for both a '+1' and '-1' bifurcation seen in Figure 3.24. Within this section we will focus on three different pacing periods. We have picked $T_p = 0.6$ s which is the critical pacing period for 2 values of τ_{sr} in the purely SR coupled case, $T_p = 0.95$ s which relates to 4 values and $T_p = 1.012$ s which relates to many values. Since our choices are based on the purely SR case, we begin by looking at SR dominant coupling. As has been seen throughout this thesis, the bifurcation tied to this relationship is a '+1' bifurcation.

The results of extending the plots of the two coupling strength values at these fixed pacing periods under which a '+1' bifurcation occurs can be seen in Figures 4.12A-4.12D. Figure 4.12A relates to $T_p = 0.6$ s, Figure 4.12B to $T_p = 0.95$ s and both Figures 4.12C and 4.12D to $T_p = 1.012$ s. In all four of these figures the blue line marks the point at which a '+1' bifurcation occurs with the synchronised single-period orbit stable in the region labelled S and unstable in the region labelled U. The red line marks the point at which the synchronised single-period orbit undergoes a period-doubling bifurcation. Note that, despite appearances, the blue and red lines do not merge in Figure 4.12A.

Figures 4.12A-4.12D illustrate how the plot for coupling purely through the SR informs the plot for dominant SR coupling since all the blue lines stem directly from the y-axis. Further to this, in Figures 4.12C and 4.12D, we see the formation of new bumps revealing that even under joint coupling the shape of the plot related to a '+1' bifurcation is very intricate. A comparison of the plots in Figure 4.12 also reveals the effect of increasing the pacing period on the possibility of a '+1' bifurcation occurring. As the pacing period is slowed, the range of cytosolic coupling strengths under which a '+1' bifurcation can occur decreases. Therefore a '+1' bifurcation is more likely to occur at faster pacing periods, as long as the pacing period is not too close to the value of the critical pacing period in the uncoupled case.

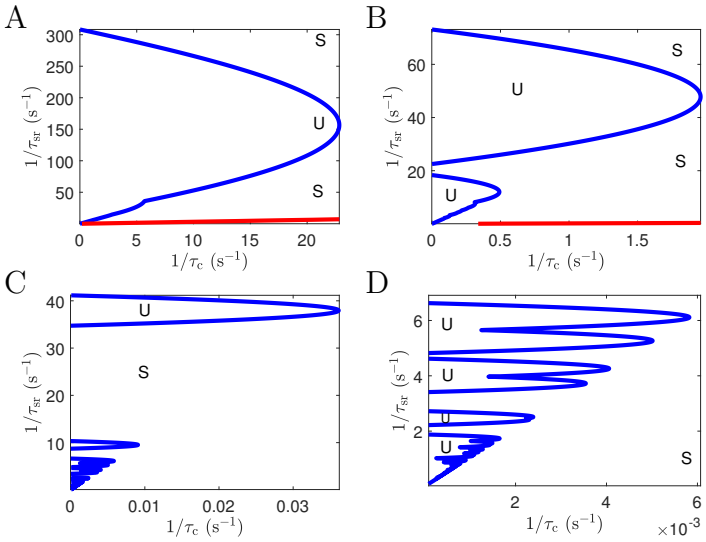

Figure 4.12: A comparison of the coupling strengths that allow a '+1' bifurcation of the synchronised state to occur at different pacing periods for a network with both SR and cytosolic coupling. Pacing periods considered are $T_p = 0.6$ s (A), $T_p = 0.95$ s (B) and $T_p = 1.012$ s (C,D) for a network of 250 sarcomeres. In regions labelled S the synchronised state is stable, whilst it is unstable in regions labelled U. The blue line marks the values for a '+1' bifurcation and the red line is for a period-doubling bifurcation. All other parameters as in Appendix A.

As with the purely SR coupled case, when we move from one bump to another we find spatial pattern at the onset of the '+1' bifurcation changes. Moreover, we find that as we move along the blue line a change in the spatial behaviour may occur without switching between two distinct bumps. This is most pronounced whilst moving along the plot for the values of both coupling strengths a which a '+1' bifurcation occurs in Figure 4.12A which appears smooth barring one small kink. However, whilst this kink does also allude to a change in the onset, it is not the only point at which a change occurs. Furthermore, as with the purely coupled case, the changes in pattern are not always small. Three examples of the different spatial patterns that can be seen at the onset of a '+1' bifurcation under dominant SR coupling are shown in Figure 4.13.

Since we have seen that the spatial pattern at the onset of a '+1' bifurcation can change for a fixed pacing period in the joint coupling case, it stands to reason the same may occur for a period-doubling bifurcation. As such we have also extended the plots based around the point at which a period-doubling bifurcation occurs in the joint coupling case. The extended plots are displayed in Figures 4.14A-4.14C. The labelling and colour scheme are the same as those used in Figure

4.12.

Unlike the plots showing the balance between two coupling strengths for a '+1' bifurcation to occur at a fixed pacing period, the plots focused on a period-doubling bifurcation appear to be much more linear in shape. Furthermore, a comparison of Figures 4.14A-4.14C reveals that the shape of the plots is much less varied between pacing periods. The only notable change we see is that the gradient of the plot decreases as we increase the pacing period.

A smaller difference between the three plots in Figure 4.14 is the placement of small bends within the plot describing when a period-doubling bifurcation takes place. These bends, much like the bumps in Figure 4.12, mark points where the spatial pattern at the onset of the bifurcation changes. However, as with a '+1' bifurcation, the spatial pattern can also change without a bend occurring in the plot. In Figure 4.15 we present two of the spatial changes that occur as we vary the coupling strengths, such that we move along the plot in Figure 4.14 related to the critical pacing period $T_p = 0.6$ s. Figures 4.15A and 4.15D show the peak subsarcolemmal Ca^{2+} concentrations from one pacing period whilst Figures 4.15B and 4.15E show the peak concentrations from the following pacing period.

Figure 4.15 portray two very different spatial patterns. As with purely cytosolic coupling, we find we still have a period-doubling bifurcation and the eigenvectors, shown in Figures 4.15C and 4.15F, related to the eigenvalue lying outside the unit circle predicts the spatial pattern at the onset. The key difference is that these spatial patterns change dependent on the values of both coupling strengths. The spatial pattern in Figures 4.15A and 4.15B contains small pockets of what could be described as SDA. These small pockets are then separated by sarcomeres that have period-doubled orbits with very low amplitude alternans.

On the other hand, in Figures 4.15D and 4.15E, the SDA is on a much larger scale. These larger scales are the forms of spatial alternans that have been linked to conditions such as ventricular arrythmia [112]. Interestingly, these spatially discordant patterns increase in regional scale as the two coupling strengths are increased such that a period-doubling bifurcation still occurs. This appears to contradict recent findings that suggest an increase in coupling strength suppresses spatial discordance in subcellular alternans [113]. However, in that case the

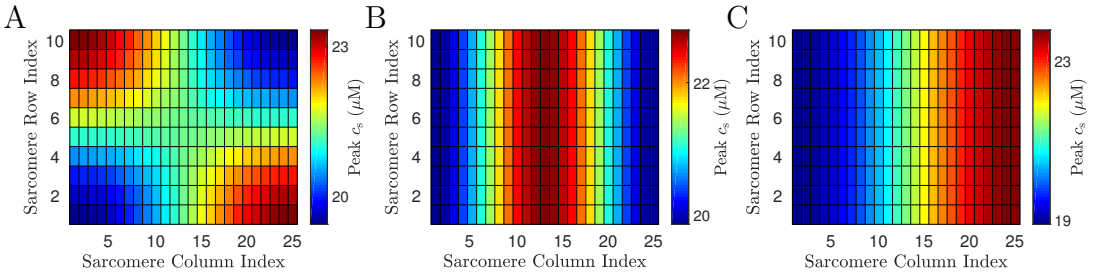

Figure 4.13: A comparison of spatial behaviours just after a bifurcation of the synchronised state, as we move along the blue plot in Figure 4.12A. The plots show the peak subsarcolemmal Ca^{2+} concentrations and from a single pacing period in a network of 250 sarcomeres with pacing period $T_p = 0.6$ s. The coupling parameters are $\tau_{sr} = 20/203$ s and $\tau_c = 0.5$ s (A), $\tau_{sr} = 25/676$ s and $\tau_c = 0.2$ s (B), $\tau_{sr} = 0.0131$ s and $\tau_c = 1/15$ s (C). All other parameters as in Appendix A.

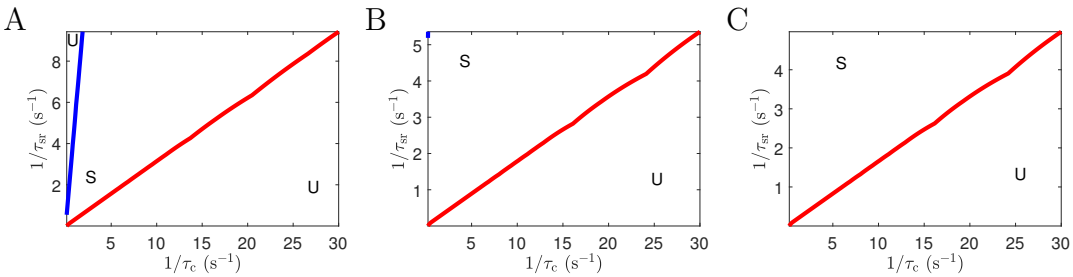

Figure 4.14: A comparison of the coupling strengths that allow a period-doubling bifurcation of the synchronised state to occur at different pacing periods for a network with both SR and cytosolic coupling. Pacing periods considered are $T_p = 0.6$ s (A), $T_p = 0.95$ s (B) and $T_p = 1.012$ s (C) for a network of 250 sarcomeres. In regions labelled S the synchronised state is stable, whilst it is unstable in regions labelled U. The blue line marks the values that leads to a '+1' bifurcation and the red line leads to a period-doubling bifurcation. All other parameters as in Appendix A.

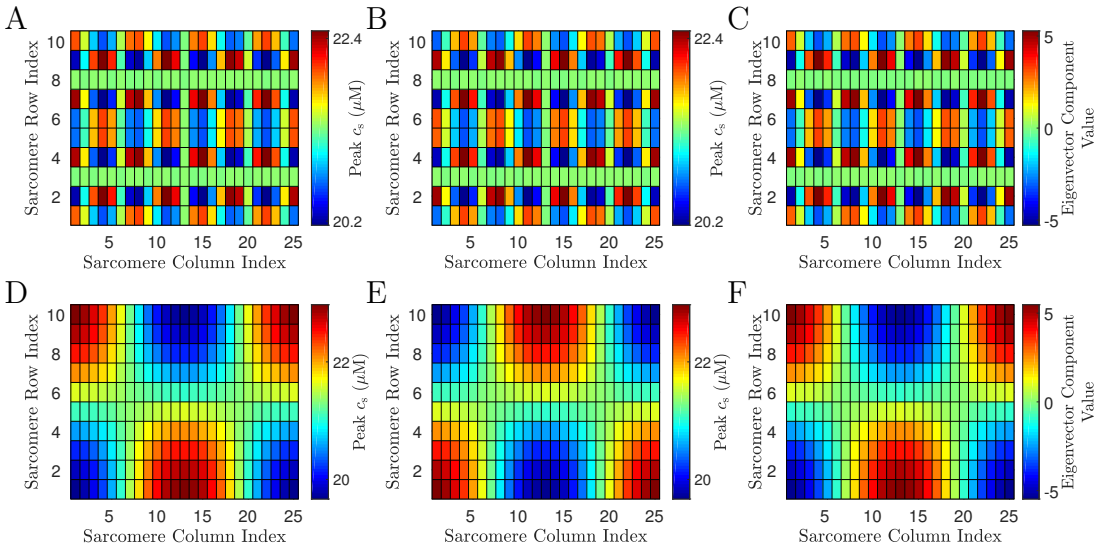

Figure 4.15: A comparison of spatial behaviours just after a bifurcation of the synchronised state, as we move along the red plot in Figure 4.14A. The plots show the peak subsarcolemmal Ca^{2+} concentration from two simulations of a 250 sarcomere network across two successive pacing periods. A and C represent the first pacing periods whilst B and D represent the second pacing period. For both these simulations $T_p = 0.6$ s. In A and B $\tau_c = 5/6$ s and $\tau_{sr} = 0.37745$ s. In C and D $\tau_c = 1/25$ s and $\tau_{sr} = 50/393$ s. The values of the components in the unstable eigenvector related to all the subsarcolemmal Ca^{2+} concentrations for A and B is in plot C whilst the same values for D and E are contained in plot F. All other parameters as in Appendix A.

increase in coupling strength was based solely on cytosolic coupling, whereas in our case we have increased both. An increase in just the cytosolic coupling also appears to sometimes produce regionally larger SDA as well but not always. This is due to the introduction of further unstable eigenvectors and thus increases or decreases of the regional scale of SDA depend on which linear combination of the unstable eigenvectors dictates the resultant behaviour of the system.

The spatial pattern that occurs as we reach very strong coupling in both the cytosol and SR can be seen in Figure 4.16. The behaviour seen in Figure 4.16 is traditionally what we think of when we talk of SDA. This type of SDA has been shown to occur experimentally under voltage clamp conditions due to experimentally induced intracellular Ca^{2+} waves [114] or heterogeneities between sarcomeres [15]. However, there appears to be little to no examples of SDA forming purely due to the balance of coupling strengths within a system with homogenous sarcomere dynamics in either experimental or modelling studies. We shall discuss these findings in more depth in Section 4.5.3.

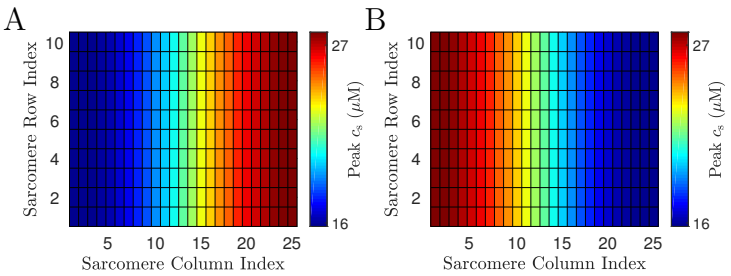

Figure 4.16: Example of SDA under voltage clamp conditions in a homogenous network. Plots of the peak subsarcolemmal Ca^{2+} concentration from two simulations of a 250 sarcomere network across two successive pacing periods. For these simulations $T_p = 0.6$ s, $\tau_c = 1/140$ s and $\tau_{sr} = 1/37$ s. All other parameters as in Appendix A.

4.4 Effects Of Diffusion At Fast Pacing Periods

In Section 2.5.1 we saw that, when paced fast enough, the uncoupled PWL system could undergo a period-doubling bifurcation. As we have discussed previously, the behaviour of the uncoupled case carries over into the network case depending on the strength of the coupling. This implies that a subcellular network of sarcomeres under both fast pacing and balanced coupling should follow a synchronised period-doubled orbit. Such a pattern can be regarded as SCA. However, in Sections 3.2.2 and 3.4.1, we stated that the plots showing how the value of the critical pacing period at which a period-doubling bifurcation occurs against the cytosolic coupling strength suggested that spatial alternans would occur no matter the coupling strength at fast pacing periods. As such we first confirm whether or not SCA is a stable state of the system when coupling between the SR and cytosol is reasonably balanced.

Figure 4.17 confirms that SCA is a stable state of the system. Figure 4.17A shows that individual sarcomeres follow period-doubled orbits. Furthermore, it illustrates that two neighbouring sarcomeres follow the same orbit in synchrony. Such behaviour occurs throughout the entire network as can seen in Figures 4.17C and 4.17D. The period-doubled orbit for every sarcomere is the same as that seen in Figure 2.9A for the uncoupled case. Such behaviour is what we describe as SCA and its stability is confirmed by the plot of the eigenvalues in Figure 4.17B. This means that the behaviour of the uncoupled case carries over to the network under the guise of SCA. Moreover, this informs us that spatial alternans do not necessarily occur with the introduction of cytosolic coupling.

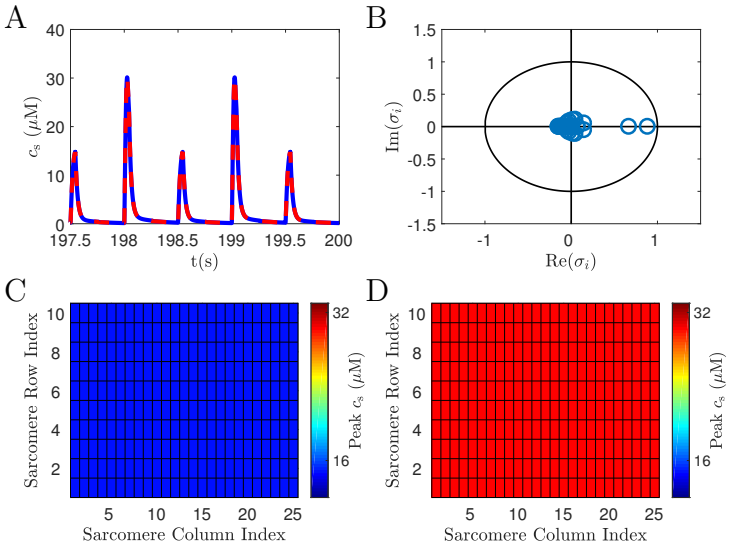

Figure 4.17: Simulation and stability analysis results illustrating SCA is stable synchronous state under balanced coupling at fast pacing periods. Trajectories from two neighbouring sarcomeres (blue representing one sarcomere and the dashed red the other) of the subsarcolemmal Ca^{2+} concentration (A). Plot of the eigenvalues of the system (B). Plots of the peak subsarcolemmal Ca^{2+} concentration across two successive pacing periods (C & D). The network contains 250 sarcomeres with coupling strengths $\tau_{ci} = 0.08$ s, $\tau_{sr} = 0.2$ s and is simulated with pacing period $T_p = 0.5$ s. All other parameters as in Appendix A.

4.4.1 Dominant Cytosolic Coupling

Since SCA is a attractor of the system where each sarcomere follows a period-double orbit in synchrony, our approach to the studying the stability of the system is still valid. Since we have shown that when a form of coupling is dominant enough it can cause a bifurcation when a synchronised single-period orbit is the attractor, we will now consider whether the same can happen when SCA is the attractor of the system. To begin with we consider what happens if we increase the dominance of the cytosolic coupling strength. The results of one such simulation can be seen in Figure 4.18.

The results of these simulations reveal that under dominant cytosolic coupling the system undergoes another period-doubling bifurcation. Thus, the system now has period-four orbits. Figures 4.18A-4.18D give an example of one of these period-4 orbits. If we compare the placement of the regions of larger and smaller peak subsarcolemmal Ca^{2+} concentrations we see that that these regions switch each beat as they do in SDA. However if we also compare the values of these largest and smallest peak concentrations we find they all decrease as we go from

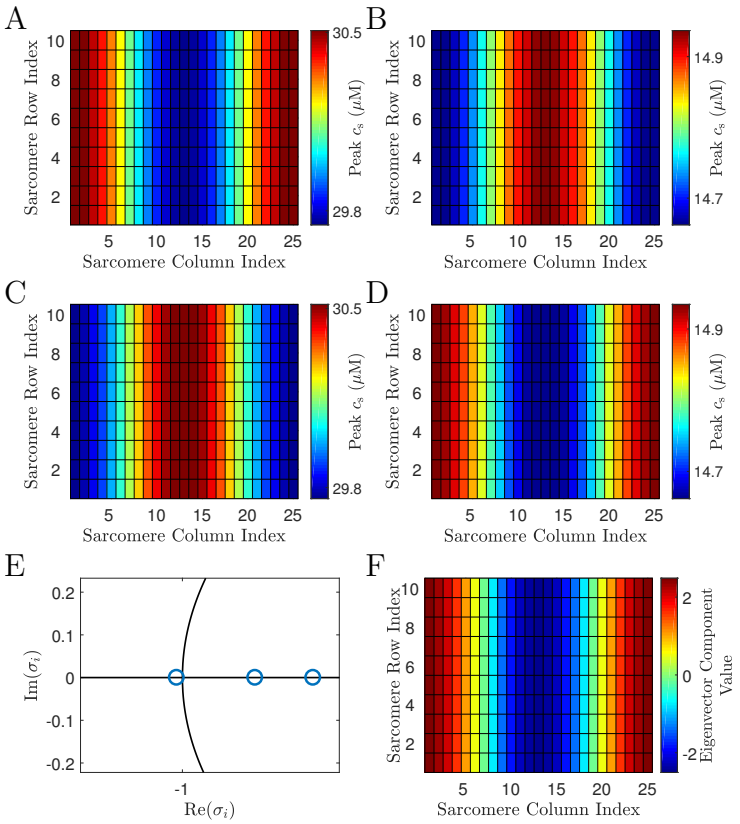

Figure 4.18: Simulation and stability analysis results demonstrating that dominant cytosolic coupling can cause SCA to undergo a period-doubling bifurcation. Peak subsarcolemmal Ca^{2+} concentration from 4 consecutive pacing periods (A,D) of a network containing 250 sarcomeres with coupling strengths $\tau_{ci} = 0.012$ s, $\tau_{sr} = 1.3$ s and simulated at a pacing period $T_p = 0.5$ s. Also plotted are the key eigenvalue (E) and the values of the components in the unstable eigenvector related to all the subsarcolemmal Ca^{2+} concentrations within the network (F). All other parameters as in Appendix A.

Figure 4.18A to Figure 4.18B before then all increasing in Figure 4.18C and then finally decreasing again in Figure 4.18D. This can be seen clearest by considering the scale on the colour bar. Further to this, Figures 4.18E and 4.18F reveal that our stability approach can be used to predict the onset of these period-4 patterns. The eigenvalue passing out of the unit circle in Figure 4.18E confirms that a period-doubling bifurcation of the SCA state has occurred, causing period-4 trajectories. The related eigenvector in Figure 4.18F then gives an indication of the spatial pattern associated with this bifurcation.

Our findings here demonstrate how spatially discordant period-4 behaviour can arise due to an increased dominance in cytosolic coupling. Whilst period-4 orbits in calcium have been seen before [11] and linked to other parameters, this is the first evidence for a role of subcellular diffusion. While there have been studies into tracking for more complex spatial patterning [91], these have focused on cellular and tissue networks. By showing that these patterns can occur on the subcellular scale, in much the same way as SDA, we provide evidence of a possible underlying mechanism to these patterns at tissue scales. Whether this is the case needs further research involving models including voltage dynamics since instabilities in the voltage at tissue levels are what drive pathological conditions. Thus this would allow us to see if subcellular period-four spatial alternans have any direct links to pathological conditions due to the bidirectional coupling between the calcium dynamics and voltage dynamics within the heart.

Whilst we have already determined that at a fixed pacing period, changes in the intracellular diffusion rates can cause bifurcations to a state of SCA, it is key to also understand how a change in pacing period can also have an affect. To do this we have included plots for the values of the coupling strengths that cause a period-doubling bifurcation of SCA at three different pacing periods in Figure 4.19.

A comparison of Figures 4.19A and 4.19B reveals that a decrease in the pacing period from 0.5 s to 0.4 s means that the dominance in cytosolic coupling for a bifurcation to take place can be decreased. The clearest representation of this is the increase in the gradient between the two curves in 4.19A to 4.19B. However this effect is diminished as we decrease the pacing period further, as a comparison

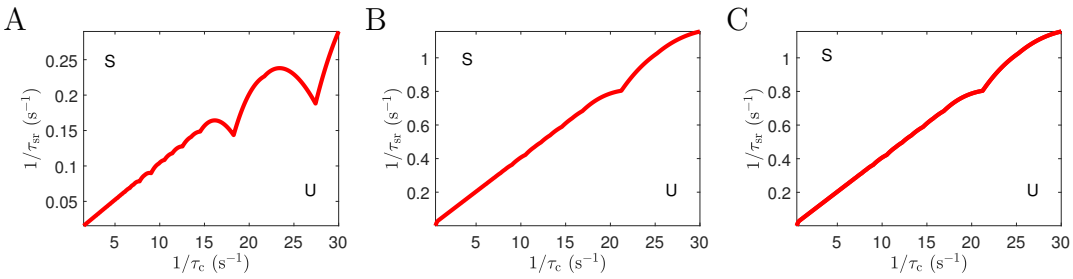

Figure 4.19: A comparison of the coupling strengths that allow a period-doubling bifurcation of SCA at different pacing periods for a network with both SR and cytosolic coupling. The network contains 250 sarcomeres paced and we consider pacing periods $T_p = 0.5$ s (A), $T_p = 0.4$ s (B) and $T_p = 0.3$ s (C). S marks the region where SCA is stable whilst U marks the region where it is unstable. All other parameters as in Appendix A.

of Figures 4.19B and 4.19C illustrates. Comparing the gradients of these two curves it is clear that they are very similar. This is possibly due to the fact that at very short pacing periods, there is very little time for a significant imbalance in the cytosolic concentration between neighbouring sarcomeres to form due to diffusion. Thus for such an imbalance to form that leads to an instability a certain level of coupling strength is needed. Such a possibility could be an avenue for further research. However, we shall now turn our attention to dominant SR coupling.

4.4.2 Dominant Sarcoplasmic Reticulum Coupling

The behaviours resulting from when the SR coupling is dominant enough to cause SCA to undergo a bifurcation are very similar to those in the synchronised single-period orbit case at slower pacing periods. An example of these behaviours is on display in Figure 4.20. We find that the form of bifurcation is again a '+1' bifurcation as revealed by the eigenvalue plot in Figure 4.20C.

Figures 4.20A and 4.20B give an indication of how a '+1' bifurcation of the SCA state affects the system. The peak concentrations in these figures demonstrate that we still have period-doubled orbits. However these period-doubled orbits vary between sarcomeres. The pattern in which these orbits vary stays constant between pacing periods and is well predicted by the eigenvector, given in Figure 4.20D, related to the eigenvalue lying outside the unit circle. In general the behavioural changes due to a '+1' bifurcation are similar to those we saw at

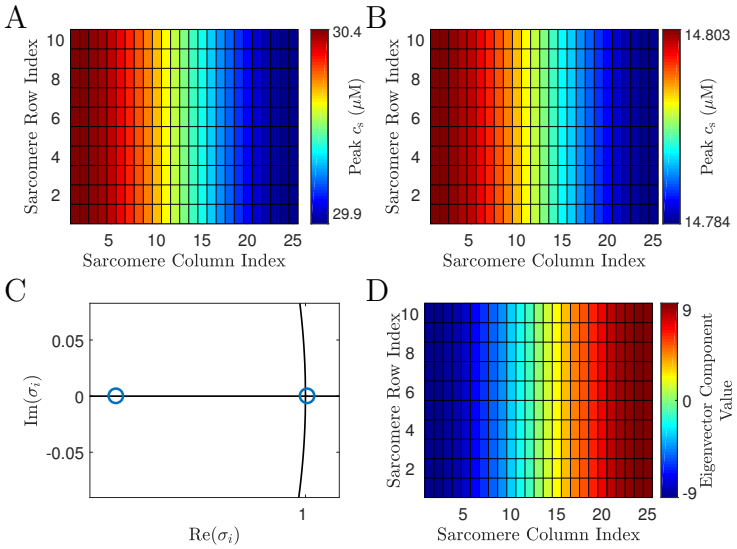

Figure 4.20: Simulation and stability analysis results demonstrating that dominant SR coupling can cause SCA to undergo a '+1' bifurcation. Peak subsarcolemmal Ca^{2+} concentration from 2 consecutive pacing periods (A,B) of a network containing 250 sarcomeres with coupling strengths $\tau_{ci} = 0.4$ s, $\tau_{sr} = 0.031$ s and simulated at a pacing period $T_p = 0.5$ s. Also plotted are the key eigenvalue (C) and the values of the components in the unstable eigenvector related to all the subsarcolemmal Ca^{2+} concentrations within the network (D). All other parameters as in Appendix A.

lower pacing periods, the key difference stems from the synchronised state pre-bifurcation. This suggests that the reasons behind such a bifurcation are to be the same as those discussed in Section 4.2.1.

As with dominant cytosolic coupling we have generated some plots showing the values of the two coupling strengths τ_c and τ_{sr} needed to invoke a '+1' bifurcation of SCA at specific pacing periods. Three of these plots are displayed in Figure 4.21. Much like with with the dominant cytosolic coupling, Figures 4.21A and 4.21B show that SR coupling does not need to be as dominant for a '+1' bifurcation to occur when $T_p = 0.4$ s compared to $T_p = 0.5$ s. However once again as the pacing period is reduced further to 0.3 s the plot in Figure 4.21C barely alters compared to 4.21B. Again this implies there is a minimum coupling strength required to destabilise the system at faster pacing periods, as with dominant cytosolic coupling.

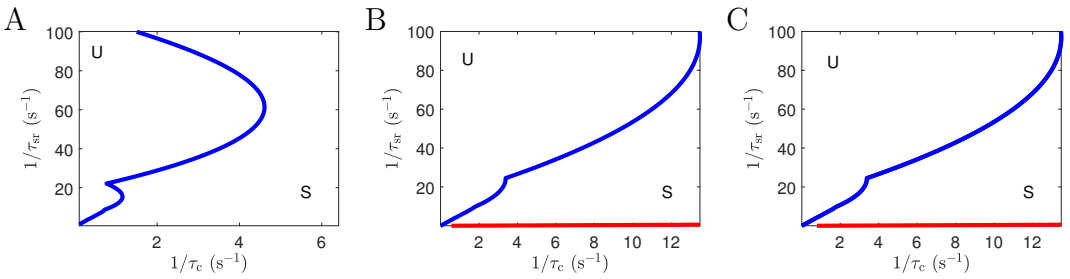

Figure 4.21: A comparison of the coupling strengths that allow a '+1' bifurcation of SCA at different pacing periods for a network with both SR and cytosolic coupling. The network contains 250 sarcomeres paced at $T_p = 0.5$ s (A), $T_p = 0.4$ s (B) and $T_p = 0.3$ s (C). S marks the region where SCA is stable whilst U marks the region where it is unstable. The red line represents the values of the coupling strengths related to a period-doubling bifurcation. All other parameters as in Appendix A.

4.5 Confirmation Of Behaviours In The Shiferaw-Karma Model

A key aspect of our findings involves understanding how they translate back into the original Shiferaw-Karma model and whether certain modelling changes, such as turning I_{CaL} into a piecewise constant function, can affect the behaviours we have discussed throughout Chapters 3 and 4. This involves studying the effect of some parameters in the Shiferaw-Karma model that have been removed under the transformation, such as those involved in the buffer Troponin C. The version of the Shiferaw Karma model considered in this section is that where the buffer Troponin C is treated as a variable and the other two cytosolic buffers are under the rapid approximation protocol [115].

4.5.1 Lowering The Uptake Strength Further Suppresses Alternans

In the plot showing the value of critical pacing period at which a period-doubling bifurcation against the uptake strength, shown in Figure 3.6A, we saw that for some pacing periods either large enough increase or decrease in uptake strength suppressed calcium alternans. Although the suppressing effect of increasing the uptake strength was discussed by Shiferaw and Karma, they did not find the same for the decreasing effect. Figure 4.22 reveals that such an effect does indeed occur in the original Shiferaw and Karma model.

A comparison of Figure 4.22A and 4.22B illustrate that a decrease of the

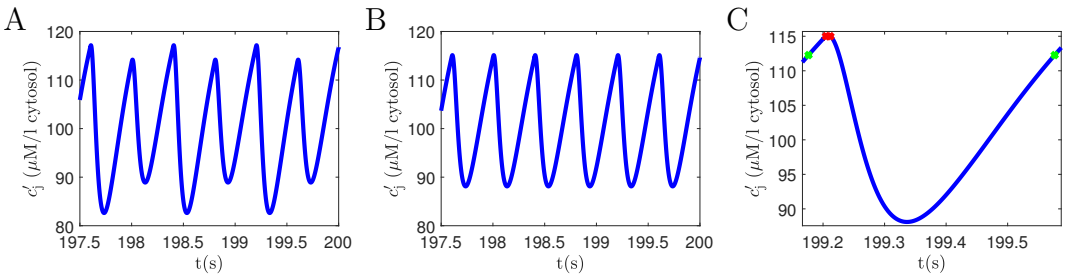

Figure 4.22: Confirmation that lowering the uptake strength enough can suppress alternans in the Shiferaw-Karma model. Unrecruited JSR Ca^{2+} concentrations from simulations of the original Shiferaw-Karma model with uptake strengths $v_{\text{up}} = 250$ s^{-1} (A) and $v_{\text{up}} = 218$ s^{-1} (B,C). In plot C the green stars represent the start and end of the voltage clamp and the red stars represent the switches in load-release function Q. Both simulations have been performed at a pacing period of $T_p = 0.4$ s. All other parameters as in Appendix A.

uptake strength within the Shiferaw-Karma model can suppress alternans, as suggested by our studies based on the PWL version. Further still, the simulation leading to Figure 4.22B reveals a shift in the switch timings for the load-release function, as seen in Figure 4.22C. This links to the discussion in Section 3.2.1 and supports the idea that a low enough uptake strength can suppress alternans. Furthermore, in the original Shiferaw-Karma model I_{CaL} is not a piece-constant function but a continuous function. Now referring back to equation (2.1), the SR release is dependent upon the product of the load-release function Q and I_{CaL}. As usual the largest values of I_{CaL} occur at the start of the pacing period but when the uptake strength is significantly lowered the steep release from Q is delayed. Thus this prevents the steep release happening in tandem with the peak flow through the L-type Ca^{2+} channel. This in turns decreases the product of these functions and causes a depleted release from the SR. Hence, despite the weaker uptake strength, the SERCA pumps can replenish the SR Ca^{2+} concentration in a much shorter time. This prevents a mishandling of the calcium and suppresses the occurrence of alternans.

4.5.2 Sarcoplasmic Reticulum Coupling Introduces A New Bifurcation

Another major finding revealed in this chapter is that of the '+1' bifurcation due to dominant SR coupling. Our simulations of the PWL model have revealed that under strong enough SR coupling, the synchronous state can become unstable

leading to the creation of new single period orbits.

Figure 4.23 reveals that the original Shiferaw-Karma model does exhibit the behaviour illustrated in Figure 3.21, when purely coupled through the SR at a strong enough coupling strength. As in the PWL model, this behaviours includes the creation of new single-period orbits that vary across sarcomeres creating the spatial pattern seen in Figure 4.23C. Interestingly, we found that the behaviour appeared to require a much stronger coupling strength within the original Shiferaw-Karma model than that found in the PWL model. As discussed in both Section 4.1 and 4.2 the '+1' bifurcation appears to be strongly associated with the SERCA pump behaviour and timing of the steep release from the load-release function. Whilst the load-release function remains the same in the original Shiferaw-Karma model, the SERCA pump is modelled as a Hill function as opposed to the linear function used in the PWL model. This means the SERCA pump is not replenishing the SR Ca^{2+} concentration in the same way, particularly when the cytosolic concentration is low or high. Since we see the need for even stronger coupling through the SR for a '+1' bifurcation to take place, this suggests the way the SERCA pump behaves throughout the pacing period has a key role in the onset of a '+1' bifurcation.

Having established that the '+1' bifurcation and its associated behaviour occurs in the Shiferaw-Karma model, in a network of sarcomeres purely coupled through the SR we now turn our attention to a network with coupling through the SR and cytosol. In Figure 4.24 are the results from four simulations with different coupling strengths. Figure 4.24A provides an example of a '+1' bifurcation due to dominant SR coupling which as we can see now has a new spatial pattern. This confirms that changes of spatial pattern at the point of bifurcation occur in the Shiferaw-Karma model for a '+1' bifurcation. Furthermore, Figure 4.24B confirms that when the SR coupling is exceptionally strong the system reverts back to a synchronous single-period orbit. In both these cases the coupling strength values are much more alike to the ones in the PWL model for the displayed behaviours. This is likely due to the fact that the coupling is now very strong and therefore has a much more dominant role in the occurrence of '+1' bifurcation compared to the behaviour of the SERCA pumps.

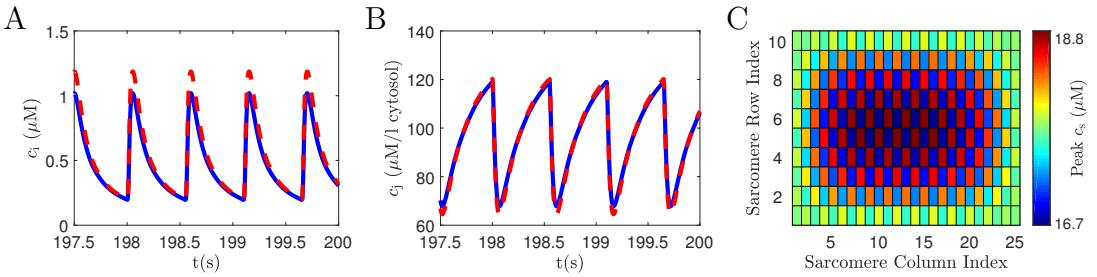

Figure 4.23: Confirmation that the '+1' bifurcation of the synchronised state can occur in the Shiferaw-Karma model due to strong SR coupling. Results of a simulation of the original Shiferaw-Karma model in a purely SR coupled two-dimensional network of 250 sarcomeres with coupling parameter $\tau_{\mathrm{sr}} = 6.9$ s and the system ran at a pacing period of $T_p = 0.55$ s with uptake strength $v_{\mathrm{up}} = 330\ \mathrm{s}^{-1}$. All other parameters as in Appendix A.

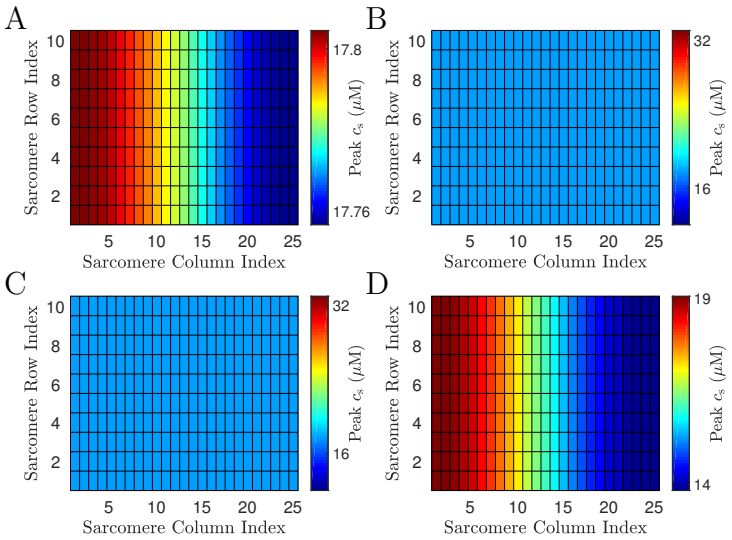

Figure 4.24: A comparison of how altering the total concentration of Troponin C can affect the occurrence of a '+1' bifurcation of the synchronised state in the Shiferaw-Karma model. Peak subsarcolemmal Ca^{2+} concentrations from a single pacing period in network of 250 sarcomeres with coupling strengths $\tau_{sr} = 0.01$ s, $\tau_{ci} = 0.08$ s (A), $\tau_{sr} = 0.001$ s, $\tau_{ci} = 2$ s (B), $\tau_{sr} = 0.01$ s, $\tau_{ci} = 0.04$ s (C) and $\tau_{sr} = 0.01$ s, $\tau_{ci} = 0.04$ s (D). In D the total concentration of Troponin C $B_{\mathrm{T}} = 100$ μmol/l cytosol whilst $B_{\mathrm{T}} = 70$ μmol/l cytosol as usual in all other simulations. All simulations ran at a pacing period of $T_p = 0.55$ s with uptake strength $v_{\mathrm{up}} = 330\ \mathrm{s}^{-1}$. All other parameters as in Appendix A.

One of the key changes from moving between the PWL model and the original Shiferaw-Karma model is how the buffering is modelled. In the PWL model the buffering is modelled as a constant whilst in the Shiferaw-Karma model the buffering to SR membrane and calmodulin binding sites are done using the rapid buffering approximation [115] whilst the amount of Ca^{2+} bound to Troponin C is modelled as a variable. The total concentration of Troponin C has been shown to vary between $56 - 150$ μmol/l cytosol [116, 117]. Through an increase in this value within our model we have been able to induce a '+1' bifurcation for coupling strengths where the synchronised single-period orbit was originally stable. An example of this can be seen by comparing Figures 4.24C and 4.24D. In these two simulations the values for the two coupling strengths remain the same but in the case of Figure 4.24D the total concentration of Troponin C has been increased.

4.5.3 Spatially Discordant Alternans

In Section 4.3 we saw SDA could form when cytosolic coupling is dominant and both forms of coupling are strong at the point of bifurcation. This form of alternans in the Shiferaw-Karma model has been studied before [94] but not under voltage clamp conditions. To confirm this is not an artefact of making the model PWL we have provided an example of this behaviour from the original Shiferaw-Karma model with clamped voltage in Figure 4.25.

As discussed in Section 2.2.3, SDA has been reported in a version of the Shiferaw-Karma model including voltage dynamics [94]. Moreover, it has been shown that the calcium dynamics are the leading cause of this but the voltage dynamics were still deemed to have a role [96]. However, as Figure 4.25 confirms, the voltage dynamics are in fact not a necessity for SDA to appear. This demonstrates that not only are the calcium dynamics the most likely cause of alternans but they can also drive the spatial pattern of these alternans at a subcellular level. This is a key point as the spatial patterning of subcellular alternans is believed to be linked to the behaviour of alternans at a tissue scale. Thus, by understanding what drives these patterns, we can hope to develop treatments that can prevent patterns strongly linked to pathological behaviour.

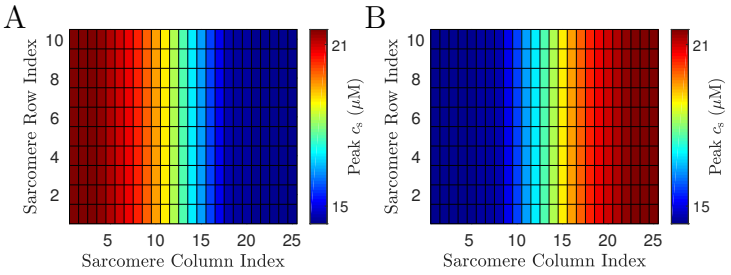

Figure 4.25: Example of SDA in the Shiferaw-Karma model. Plots of the peak subsarcolemmal Ca^{2+} concentration from a simulation of a 250 sarcomere network across two successive pacing periods. For these simulations $T_p = 0.6$ s, $\tau_c = 1/14000$ s and $\tau_{sr} = 1/37$ s along with uptake strength of $v_{up} = 330$ s^{-1}. All other parameters as in Appendix A.

4.6 Summary

The main focus of this chapter has been based upon how changes in the coupling strengths can vary the spatial patterns seen at the onset of a bifurcation. Furthermore, as made clear in Section 4.3, it is only the spatial aspect that alters. If the cytosolic coupling is dominant the bifurcation remains a period-doubling one, if the SR coupling is dominant it is still a '+1' bifurcation. Moreover, we have seen that these spatial patterns can alter quite drastically with very little change to the coupling strengths.

In Sections 4.2 and 4.3 we have illustrated that, on occasion, the point at which a new spatial pattern may appear at the onset of a '+1' bifurcation can be obtained from the plot of the values of critical pacing period for a '+1' bifurcation against the values of the coupling strength. This can be done by finding bumps in the plot such as those seen in Figures 4.5 and 4.12. These plots also demonstrated that the range of cytosolic coupling strengths that allow for a '+1' bifurcation to occur decreases at slower pacing periods.

In Section 4.1 we developed our understanding around a region of bistability for weaker coupling strengths first alluded to in Section 3. We discussed how this behaviour appears related to the balance between SERCA pump activity at the end of the pacing period and the length of the pacing period overall. We also noted that steep release from the load-release function at the start of the next pacing period is essential to the occurrence of bistability. In Section 4.2 we built upon this, revealing how the range of pacing periods that allowed for a '+1' bifurcation was tightly linked to the balance between steep release from the

load-release function and the uptake strength. This includes the realisation that without steep release from the load-release function, a '+1' bifurcation cannot occur.

In Section 4.4 we turned our attention to pacing periods at which the uncoupled case follows a period-doubled orbit. In this section we demonstrated the when neither form of coupling is truly dominant SCA is a stable state of the system. Furthermore, we revealed that the types of bifurcation that occur when a form of coupling is dominant enough are the same as those seen when a synchronised single-period orbit is stable. This meant that when cytosolic coupling was dominant we had a variety of period-four orbits across the network whilst when SR was dominant we had a variety of period-doubled orbits. Again this variety was due to the loss of synchronisation leading to spatial patterns that would change with the values of the coupling strength. As with the synchronous single-period state, the eigenvector linked to the eigenvalue lying outside the unit circle could be used to predict the spatial pattern the would appear when SCA lost stability.

Throughout Sections 4.2 to 4.4 we have seen further examples of the power of our stability analysis. In each of these sections we saw how the eigenvectors of the system could be used to accurately predict the spatial behaviour at the onset on a bifurcation, whether the synchronous state involved a single-period orbit or was SCA. However, in Section 4.2 we gave a small caveat through an example of a system that had degenerate eigenvalues. In this case the power of prediction was diminished as the spatial behaviour at the onset of bifurcation is no longer defined by a single eigenvector. On the other hand, since the behaviour can be described as a linear combination of the multiple eigenvectors related to the degenerate eigenvalues, we still have an idea of what kind of spatial patterning we can expect at the onset of a bifurcation. We suggested these degenerate eigenvalues were more likely to occur in networks that had a similar number of sarcomeres in both the longitudinal and transversal directions.

In Section 4.5 we turned our attention back to the original Shiferaw-Karma model and confirmed that our findings were not an artifact of making the model PWL. In Section 4.5.1 we illustrated that lowering the uptake strength enough

does suppress alternans. We pointed out that this was due to a delay in steep release from the load-release function which prevented the steep release occurring in tandem with peak flow through the L-Type Ca^{2+} channel.

We then moved onto studying our findings involving networks and coupling strengths within the context of the original Shiferaw-Karma model. In Section 4.5.2 we demonstrated that both purely and dominant SR coupled networks could undergo a '+1' bifurcation if the coupling was strong enough. We revealed that the SR coupling needed to be notably stronger in the purely coupled case when compared to the PWL model due to the changes in the model for the SERCA pump. On the other hand, as we moved to dominant SR coupling when both coupling strengths are strong the difference between the PWL and Shiferaw-Karma model diminished since these coupling strengths are now strong enough to counter the changes in the SERCA pump model. Moreover, as with the PWL model, we showed that when SR coupling was very strong the system has a stable synchronised single-period orbit.

In the joint coupling case we also confirmed that by changing both coupling strengths, whilst keeping SR coupling dominant, the spatial pattern at the onset of bifurcation also changes. We then demonstrated that an increase in the total concentration of Troponin C can induce a '+1' bifurcation for coupling strengths that originally had a stable synchronised single-period orbit. Along a similar thread, in Section 4.5.3 we demonstrated that the original Shiferaw-Karma model could demonstrate SDA without the need for voltage dynamics contrary to the suggestions from previous studies [94, 96].

5 A Network Of Subcellular Networks

In the previous two chapters we primarily focused on a single myocyte modelled as a network of sarcomeres. Within both chapters we demonstrated how both Ca^{2+} diffusion through the cytosol and SR can cause the synchronous state of the system to undergo a period-doubling or a '+1' bifurcation. In this chapter we will provide some understanding on how these bifurcations and the behaviour related to them may affect a network of cells. By doing this we hope to provide some insight into how subcellular behaviours may develop into the larger scaled patterns linked to pathological conditions. To create these networks, we introduce gap junctions to link a rectangular network of 6 cells, in which each cell contains 147 sarcomeres in a rectangular layout. The reduction in sarcomeres per cell is purely for computational purposes; this decrease in network size does not cause any notable qualitative changes to our previous findings. These gap junctions link the cells through the bulk cytosol and allow Ca^{2+} to diffuse between neighbouring cells. As discussed in Section 2.1.3, studies such as [31] have shown that gap junctions are usually found in greater numbers at the ends of the cells, a trait which will be reflected in our model. As stated in Section 2.1.3 it is still up for debate whether such diffusion occurs but whilst this is still deemed possible it is worth studying.

To begin, in Section 5.1 we describe how we have had to adapt our stability approach since not every sarcomere contains a gap junction. We then use this in Section 5.2 to study whether gap junctions, with strong enough coupling, can cause an instability when the internal coupling is balanced. Furthermore we consider whether the number of gap junctions has an affect on the gap junction coupling strength needed to produce an instability. We also make the same consideration around the placement of these gap junctions. Here, the bifurcation occurs purely due to the strength of coupling. In Section 5.3 the roles are reversed, with coupling through gap junctions kept weak to begin with, whilst the internal coupling has values such that the synchronous single-period orbit is unstable. Within this section we look at the case where the cells all have dominant cytosolic or all have dominant SR coupling as well as the case where there is a mix. When studying the case of a network with a mix of cells with different forms of internal

coupling forms, we consider how the number of cells with a certain type of internal coupling affects the overall behaviour of the network. Section 5.4 is an extension of these studies about the mix of dominant forms of internal coupling but with the addition of cells that contain balanced internal coupling. The final section contains a summary of the chapter.

5.1 Stability Approach

For the relevant sarcomeres gap junctions will be modelled by adding the term $\sum_{\kappa \in gc}({c_i}^{\kappa} - {c_i}^{\mu})/\tau_{\text{gap}}$ to the ODEs in equation (2.4), that describe the bulk cytosolic Ca^{2+} concentration in each sarcomere. Here μ represents the sarcomere we are currently focused on whilst $\kappa \in gc$ represent the sarcomeres which are connected to sarcomere μ by gap junctions. Within this thesis for each μ the set gc will only contain one sarcomere as we only connect two sarcomeres to each other by gap junctions. Any sarcomeres connected by gap junctions will only be found at either the longitudinal or transversal borders of the myocyte. The sarcomeres chosen will vary as we study different scenarios to see how the number and distribution of gap junctions affects the behaviour of the system. The strength of coupling through the gap junctions is represented by τ_{gap}. As with our internal coupling, lower values of τ_{gap} equate to stronger coupling.

Previously, we have been able to transform our system such that perturbations of the systems orbit could be described by equation (3.1). Such a transformation was computationally advantageous due to the block diagonal nature of the matrix from which we found the eigenvalues and eigenvectors of the system. However, this advantage relied on the fact that all the sarcomeres in the system had the same form of coupling and, without this property, such an approach cannot be done outside of special cases [118]. Therefore, by introducing gap junctions to our network, we cannot apply the transformation described in Section 2.4. Thus we must derive the matrix that describes how perturbations of the system progress

from the equation,

$$\dot{x}_z^\mu = [M_z x_z^\mu + f_z]\,\Theta\left(t - T_z^\mu\right)\Theta\left(T_{z+1}^\mu - t\right) + \sum_{k,\alpha} G_{k\alpha}^{\text{int}} H^{\text{int}} x_k^\alpha \Theta\left(t - T_k^\alpha\right)\Theta\left(T_{k+1}^\alpha - t\right) + \sum_{k,\alpha} G_{k\alpha}^{\text{gap}} H^{\text{gap}} x_k^\alpha \Theta\left(t - T_k^\alpha\right)\Theta\left(T_{k+1}^\alpha - t\right). \quad (5.1)$$

Equation (5.1) has similar form to equation (2.5) with the addition of the third term relating to the gap junction connections. G^{int} and G^{gap} are the connectivity matrices for the internal coupling and gap junctional coupling respectively, whilst H^{int} and H^{gap} describe which parts of the sarcomeres the connections occur through. Included in H^{int} and H^{gap} are the coupling strengths. The term used to describe gap junctions mentioned at the beginning of this section is absorbed into the matrices G^{gap} and H^{gap}. For other notation used within equation (5.1) we refer the reader to Sections 2.3 and 2.4. As with our subcellular networks we will be studying the stability of a synchronised state in which all the sarcomeres follow the same single-period orbit. Thus by perturbing around the synchronised state s, we derive the equation:

$$\begin{aligned}\frac{\mathrm{d}}{\mathrm{d}t}\delta x_z^\mu = {} & M_z \delta x_z^\mu \Theta\left(t - T_z\right)\Theta\left(T_{z+1} - t\right) \\ & + \dot{s}\left[\delta T_{z+1}^\mu \theta\left(T_{z+1} - t\right) - \delta T_z^\mu \theta\left(t - T_z\right)\right] \\ & + \sum_{k,\alpha} G_{k\alpha}^{\text{int}} H^{\text{int}} \left\{\delta x_k^\alpha \Theta\left(t - T_k\right)\Theta\left(T_{k+1} - t\right)\right. \\ & \left. + s_k\left[\delta T_{k+1}^\alpha \theta\left(T_{z+1} - t\right) - \delta T_k^\alpha \theta\left(t - T_z\right)\right]\right\} \\ & + \sum_{k,\alpha} G_{k\alpha}^{\text{gap}} H^{\text{gap}} \left\{\delta x_k^\alpha \Theta\left(t - T_k\right)\Theta\left(T_{k+1} - t\right)\right. \\ & \left. + s_k\left[\delta T_{k+1}^\alpha \theta\left(T_{z+1} - t\right) - \delta T_k^\alpha \theta\left(t - T_z\right)\right]\right\}. \quad (5.2)\end{aligned}$$

Note that switching times are identical across all sarcomeres in a synchronised state s and θ represents the Dirac-delta function. Hence, these have been rewritten as T_z and T_{z+1} in equation (5.2). Then by integrating equation (5.2) between $T_z + \delta T_z^\mu$ and $T_{z+1} + \delta T_{z+1}^\mu$ we are able to find the following equation that describes

the next perturbation in terms of the current perturbation for the entire network:

$$\begin{aligned}\delta x_{z+1} = \exp\left(M_z \otimes I_N + G^{\text{int}}_{k\alpha} \otimes H^{\text{int}} + G^{\text{gap}}_{k\alpha} \otimes H^{\text{gap}}\right)(T_{z+1} - T_z) \\ \times \left[\delta x_z - \left\{\dot{s}\left(T_z^+\right) + \left(G^{\text{int}}_{k\alpha} \otimes H^{\text{int}} + G^{\text{gap}}_{k\alpha} \otimes H^{\text{gap}}\right) s_z\right\} \delta T_z\right] \\ + \left\{\dot{s}\left(T_{z+1}^-\right) + \left(G^{\text{int}}_{k\alpha} \otimes H^{\text{int}} + G^{\text{gap}}_{k\alpha} \otimes H^{\text{gap}}\right) s_z\right\} \delta T_{z+1}. \quad (5.3)\end{aligned}$$

In equation (5.3) δx_z is a vector containing all the perturbations of the system at switching event z, I_N is the identity matrix of size $N \times N$ where N is the total number of sarcomeres within the entire network and $\otimes$ represents the Kronecker product. By starting at switch event $z = 0$ we are able to use equation (5.3) to build up the matrix S_m which describes how perturbations grow throughout a whole pacing period. This is similar to the approach using equation 3.1, the key difference is that with the introduction of gap junctions, S_m is no longer block diagonal. As in previous chapters, the eigenvalues of S_m inform us if the synchronous state is stable and the eigenvectors of S_m can be used to help understand the behaviour of the system when the synchronous state is unstable.

5.2 How The Number Of Gap Junctions Affects The Onset Of A Period-Doubling Bifurcation

To begin with we consider a network where the internal coupling has such strengths that, if there were no gap junctions, the cells would all follow a synchronised single-period orbit. We then introduce gap junctions in both the transversal and longitudinal directions. For the purposes of this thesis we shall fix the number of transversal gap junction to one per neighbouring myocytes and only vary the number of longitudinal gap junctions. We focus on the longitudinal direction since this is usually where most gap junctions are found [31]. Figure 5.1 shows the results of three different simulations of a network of 6 cells with a varying number of gap junctions. The placement of the gap junctions is marked by the colour white in the cell boundaries that are otherwise marked by magenta. This colour coding will be used throughout the whole of this chapter. The white parts of the boundary between the first and second cell in the top row of Figure 5.1 are an example of gap junctions lying in the longitudinal direction. The white

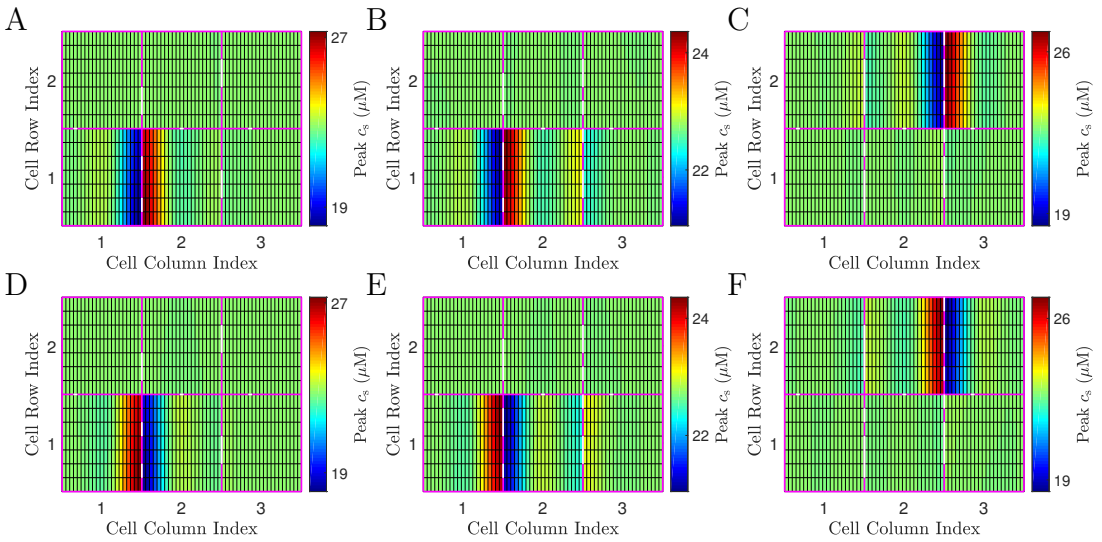

Figure 5.1: A comparison on how the number of longitudinal gap junctions effects the onset of a period-doubling bifurcation. Peak subsarcolemmal Ca^{2+} concentrations from two consecutive pacing periods for a network of 6 cells each containing 147 sarcomeres each connected by either 2 (A,D), 3 (B,E) or 4 (C,F) gap junctions in the longitudinal direction and 1 gap junction in the transversal direction. The strength of coupling through these gap junctions is either $\tau_{\text{gap}} = 0.032$ s (A,D), $\tau_{\text{gap}} = 0.0611$ s (B,E) or $\tau_{\text{gap}} = 0.0925$ s (C,F). These strengths were chosen so we are close to the point of bifurcation in each of these systems. The internal coupling strengths are $\tau_{\text{c}} = 0.05$ s and $\tau_{\text{sr}} = 0.1$ s with pacing period $T_p = 0.9$ s in all cases. Cell boundaries are in magenta with gap junctions in white. All other parameters as in Appendix A.

parts of the boundary between the cells in the top and bottom rows are examples of gap junctions lying in the transversal direction.

The coupling strengths used to create the plots in Figure 5.1 are chosen so that only one eigenvalue is outside of the unit circle. Each plot in Figure 5.1 relates to a different coupling strength since each time an extra gap junction is introduced between cells, the coupling strength needed to induce a bifurcation reduces. This reduction equates to an increase in the value of τ_{gap}. In all cases the type of bifurcation that occurs due to the introduction of the gap junctions, with a strong enough coupling parameter, is a period-doubling bifurcation.

In all three simulations the alternans produced by a period-doubling bifurcation have greatest amplitude across a single cell boundary. This can be seen by comparing any of the two consecutive pacing periods in Figure 5.1. For example, looking at Figure 5.1A we can see that the larger peak concentrations of Ca^{2+} in the subsarcolemmal space lie on the right hand side of the gap junctions between

the first and second cell in row 1, whilst the lower concentrations lie to the left. Then during the following pacing period, this distribution between higher and lower concentrations flips across the boundary between the two cells, as illustrated by Figure 5.1D. A look at the eigenvectors presented in Figure 5.2 confirms that the stability analysis agrees with this. However, a comparison of the spatial patterns presented in Figure 5.1 and the eigenvector patterns in Figure 5.2 reveal that the eigenvectors do not predict the behaviour close to the point of bifurcation as well as they did for subcellular networks.

This reduced predictive power could result from an increase in the possibility of numerical error due to a couple of factors. Both these factor stem from the fact we cannot use the master stability approach discussed at the beginning in Section 2.4. Due to this we are now performing matrix multiplication on matrices of the size 4410×4410 to create the matrix S_m, from which we derive our eigenvalues and eigenvectors. In previous chapters S_m was block diagonal, so we only needed to work with 5×5 matrices which reduced the chance of numerical error. Matrix multiplication on this new, much larger scale is likely to produce greater numerical error than we see when working with smaller matrices. Whilst we could have modelled the myocytes as one dimensional sarcomere networks to lessen this issue, we would have lost the ability to vary the number and placement of gap junctions in the longitudinal direction. The second factor relates to the fact that the parts of S_m related to the gap junctional coupling are sparse, this further lessens our ability to compute the eigenvectors accurately. However, despite this drop in eigenvector predictive power, Figure 5.2 still demonstrates that the eigenvectors provide some insight into how the network is going to behave. Figure 5.2 provides clear indications of the boundary at which the alternans amplitude will be is greatest. Furthermore, the eigenvectors give a good indication of the differences in the amplitude of the alternans when comparing boundaries. For example, the eigenvector in Figure 5.2B informs us that the amplitude of the spatial alternans is greater between the two cells in the bottom left of the network, compared with the two in the bottom right. This agrees with the results of the simulations seen in Figures 5.1B and 5.1E.

One of the more interesting results in Figure 5.1 is the change in boundary at

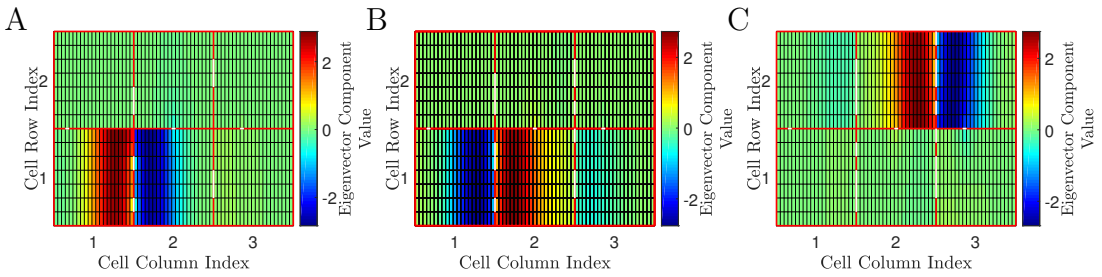

Figure 5.2: The values of the components in the unstable eigenvector related to all the subsarcolemmal Ca^{2+} concentrations within the network for the simulations shown in Figures 5.1A and 5.1D (A), Figures 5.1B and 5.1E (B) and Figures 5.1C and 5.1F (C).

which the amplitude of the alternans is greatest. In Figures 5.1A and 5.1D we see that the onset of the spatial alternans appears heavily based on the boundary of the the first two cells in the bottom row. In Figures 5.1B and 5.1E we see that the onset of the spatial alternans appears mainly based on the boundary of the the first two cells in the first row but also reveals some spatial alternans with notable amplitude between the second and third cells in the bottom row. On the other hand, the main boundary at which the spatial alternans occur shifts to the second and third cells in the top row in Figures 5.1C and 5.1F. This suggests that the placement of the gap junctions has an effect on the boundary at which the spatial alternans form.

To study if the placement of the gap junctions does affect the boundary at which the alternans have greatest amplitude, we have simulated a network with fixed coupling strengths but varied the placement of the longitudinal gap junctions. Results from three of these simulations can be seen in Figure 5.3. In this figure neighbouring cells are coupled by three gap junctions in the longitudinal direction and one gap junction in the transversal direction. In all three of these simulations the same four configurations for the longitudinal gap junctions are used, the only difference has been the placement of these configurations. By configuration, we refer to the sarcomeres within the myocytes that the gap junctions are placed within.

A comparison of the three different behaviours on display in Figure 5.3 demonstrates how the spread of gap junctions across each cell boundary appears to dictate the boundary at where spatial alternans have the greatest amplitude. In all three plots the boundary with this greatest amplitude appears to occur where

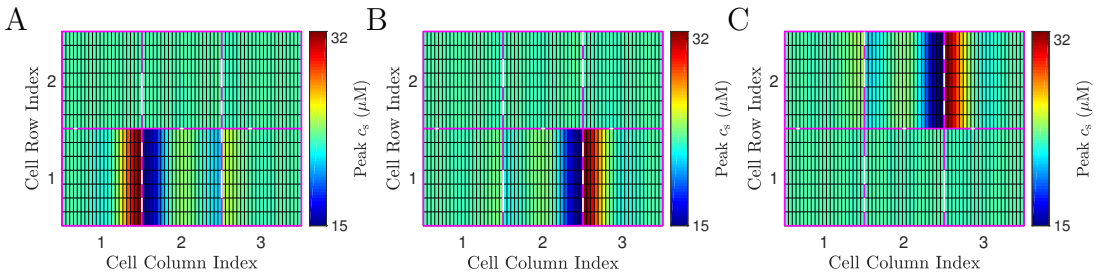

Figure 5.3: A comparison of how the spread of gap junctions along the cell boundaries in the longitudinal direction effects the spatial behaviour of alternans. Peak subsarcolemmal Ca^{2+} concentrations from a single pacing period in a network of 6 cells each containing 141 sarcomeres each connected by 3 gap junctions in the longitudinal direction and 1 gap junction in the transversal direction. The strength of coupling through these gap junctions is $\tau_{\text{gap}} = 0.0611$ s. The internal coupling strengths are $\tau_{\text{c}} = 0.05$ s and $\tau_{\text{sr}} = 0.1$ s with pacing period $T_p = 0.9$ s in all cases. Cell boundaries are in magenta with gap junctions in white. All other parameters as in Appendix A.

the gap junctions are most spread out. Such a notion appears to be supported by Figures 5.1A and 5.1C. Considering that three of the boundaries in Figure 5.1B have the largest spread of gap junctions, this suggest that when this occurs the transversal placement of gap junctions may also have a role in the amplitude of alternans at each boundary. Since the spatial alternans around the boundary between the second and third myocyte in the top row are the smallest this suggests that if multiple boundaries have the same spread of gap junctions, then the neighbouring boundary in the longitudinal direction may also have an affect.

The results of two simulations that support this theory are depicted in Figure 5.4. In Figure 5.4A the transversal gap junctions have been redistributed so that they are symmetrically placed in the longitudinal direction across the whole network. In terms of the longitudinal gap junctions we have swapped the placement of these between rows in comparison to Figure 5.1B. In Figure 5.4B we have used the same gap junction placement as used to create Figure 5.4A with the exception of shifting the gap junctions between the second and third cells in the top row down by one sarcomere.

Figure 5.4A supports the idea that the spread of the gap junction distribution in the neighbouring longitudinal cell boundary helps to dictate which boundary the alternans focus around. We say this, as despite the fact the transversal gap junctions are now even, the alternans are still focused around one of the

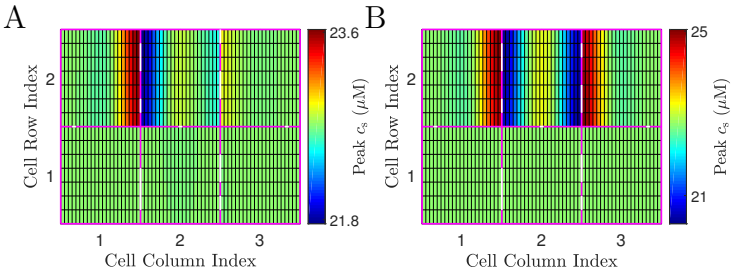

Figure 5.4: A comparison of how the spread of gap junctions along the cell boundaries in the longitudinal direction effects the spatial behaviour of alternans when the transversal gap junctions are evenly distributed. Peak subsarcolemmal Ca^{2+} concentrations from a single pacing period in a network of 6 cells each containing 141 sarcomeres each connected by 3 gap junctions in the longitudinal direction and 1 gap junction in the transversal direction. A and B are from two different simulations. The strength of coupling through these gap junctions is $\tau_{\text{gap}} = 0.0611$ s. The internal coupling strengths are $\tau_{\text{c}} = 0.05$ s and $\tau_{\text{sr}} = 0.1$ s with pacing period $T_p = 0.9$ s in all cases. Cell boundaries are in magenta with gap junctions in white. All other parameters as in Appendix A.

boundaries of the two neighbouring boundaries with the same spread of gap junctions. However, these two boundaries are still not symmetrical in terms of the amplitude of the alternans across each boundary. On the other hand, in Figure 5.4B the two boundaries are now much more similar in terms of the amplitude of the alternans across the boundary. This suggests that the placement of the longitudinal gap junctions on the boundary, as well as the spread, has much more of an effect of where we find the spatial alternans compared to the placement of the transversal gap junctions.

5.3 The Effect Of Gap Junctions In A Network Of Unstable Cells

Now we have some understanding on the role gap junctions have in a network where each myocyte's internal coupling is balanced, we turn our attention to a network in which all the myocyte's internal coupling has a form of dominant coupling. We consider three different scenarios, the case where all the cells have dominant cytosolic coupling, dominant SR coupling and the case where the form of dominant coupling varies between cells. These terms for the forms of the internal coupling carry over Chapters 3 and 4. Balanced coupling refers to internal coupling strengths that allow the sarcomeres to follow a synchronised single-period

orbit when gap junctional coupling is not involved. Dominant cytosolic coupling refers to the scenario when the cytosolic coupling is strong enough compared to the SR coupling such that the synchronised state is unstable due to a period-doubling bifurcation. Dominant SR coupling refers to when the SR coupling is strong enough compared to the cytosolic coupling such that the synchronised state is unstable due to a '+1' bifurcation.

5.3.1 A Network Of Cells With Dominant Internal Cytosolic Coupling

Since gap junctions can allow cytosolic coupling, we begin by considering the effect of introducing them to a network of cells which all internally have dominant cytosolic coupling. To begin with we wish to understand if the simple introduction of gap junctions has any major influence. Hence our first simulation, the results of which are shown in Figure 5.5, include gap junctions with very weak coupling strengths.

As expected Figure 5.5 confirms the formation of SDA due to the internally dominant cytosolic coupling. The regional distribution of the SDA agrees with the case excluding no gap junctions. Furthermore, there is no evidence of alternans forming around the gap junctions as seen in Section 5.2. However this does not mean that the introduction of gap junctions does not alter the behaviour. A comparison of the SDA between each cell reveals variations in the amplitude of the SDA. The term amplitude of the SDA refers to the difference between the lowest and highest peak subsarcolemmal Ca^{2+} concentration within a cell with SDA. For example, we can see that the amplitude of SDA is greater for the cell in the top row compared to that of the cell in the bottom row. The unstable eigenvectors of the system depicted in Figure 5.6 provide some insight into why this is the case, particularly when we consider the eigenvectors of the system when there are no gap junctions.

From Figure 5.5 we can see that no single eigenvector dictates the behaviour of the system but looking at the differences between each eigenvector and considering the resultant behaviour of the system, we can make the assumption that a linear combination of some or all of these eigenvectors drives the system. Furthermore, these six eigenvectors are the result of introducing gap junctions and without the

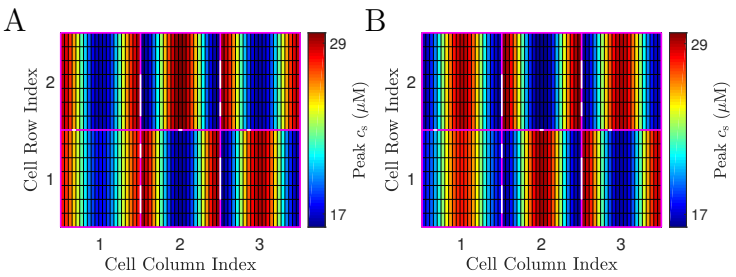

Figure 5.5: Simulation results from a network of cells with dominant internal cytosolic coupling connected by gap junctions with a weak coupling strength. Peak subsarcolemmal Ca^{2+} concentrations from two consecutive pacing periods (A and B) in a network of 6 cells each containing 141 sarcomeres each connected by 3 gap junctions in the longitudinal direction and 1 gap junction in the transversal direction. The strength of coupling through these gap junctions is $\tau_{\text{gap}} = 10$ s. The internal coupling strengths are $\tau_{\text{c}} = 0.0261$ s and $\tau_{\text{sr}} = 0.15$ s with pacing period $T_p = 0.9$ s in all cases. Cell boundaries are in magenta with gap junctions in white. All other parameters as in Appendix A.

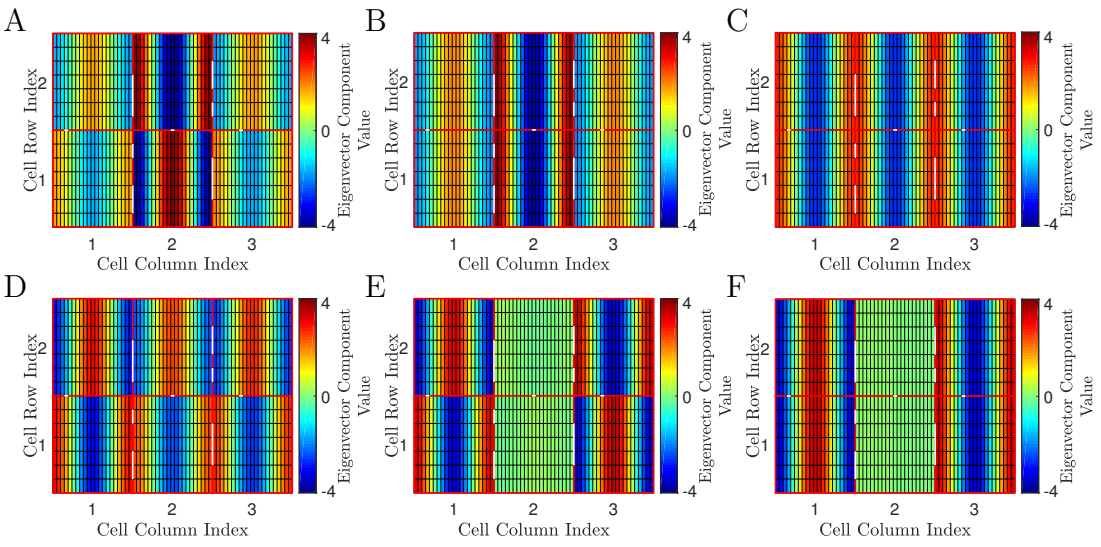

Figure 5.6: The values of the components in the unstable eigenvectors related to all the subsarcolemmal Ca^{2+} concentrations within the network for the simulations shown in Figure 5.5.

gap junctions present we obtain a family of six eigenvectors similar to the one in Figure 5.7. This informs us that, by introducing gap junctions, we effectively create six new unstable eigenvectors that appear to be linear combinations of the eigenvectors for the system without gap junctions. Combining this with what we see in Figure 5.5 demonstrates how, without affecting the stability of the system, the introduction of gap junctions has had a major influence on the spatial patterns we find within a network when all the cells have internal dominant cytosolic coupling with identical coupling strengths.

Now as we increase the strength of coupling through the gap junctions, we find the gap junctions have a greater role in dictating the behaviour of the system. Results of a simulation with strong coupling are shown in Figure 5.8. Looking at Figure 5.8 closely we see that the symmetry of the SDA shown in Figure 5.5 begins to disappear due to the increase in the gap junctional strength. The patterns within each cell, whilst still resembling the behaviour already seen, are much more influenced by the placement of the gap junctions. For example, if we look at the third cell in the first row of Figure 5.8 we see that the shade of the red area on the left hand side of the myocyte is darker than that found on the right hand side of the myocyte. This signifies that the subsarcolemmal Ca^{2+} concentration is greater on the left hand side, during this pacing period, compared to the right hand side.

As discussed in previous chapters, there is evidence that SDA between larger regions of the myocyte may be more pathological [15]. From Figure 5.8 we find that an increased gap junction coupling strength begins to decrease the size and number of the regions in which the largest amplitude alternans are found. This suggests that when cytosolic coupling is dominant in all the myocytes, in terms of the internal coupling, then the increased coupling through gap junctions may be beneficial, particularly when the internal coupling produces SDA.

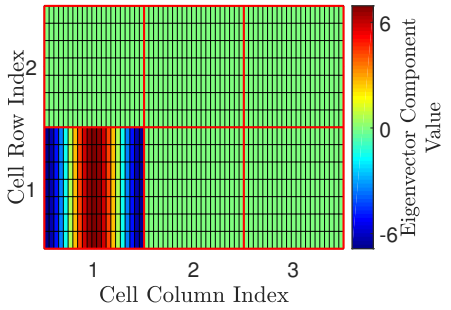

Figure 5.7: The values of the components from one of the six unstable eigenvectors related to all the subsarcolemmal Ca^{2+} concentrations for a network of 6 unconnected cells each containing 141 sarcomeres. The internal coupling strengths are $\tau_c = 0.0261$ s and $\tau_{sr} = 0.15$ s with pacing period $T_p = 0.9$ s in all cases. Cell boundaries are in magenta. All other parameters as in Appendix A.

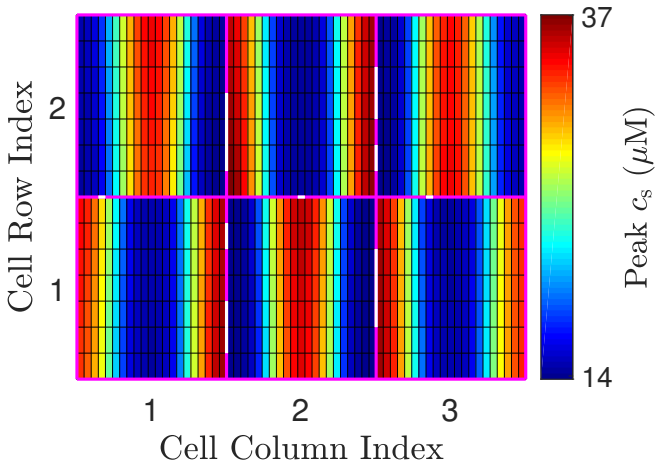

Figure 5.8: Simulation results from a network of cells with dominant internal cytosolic coupling connected by gap junctions under with a stronger coupling strength than that used to create Figure 5.5. Peak subsarcolemmal Ca^{2+} concentrations from a single pacing period in a network of 6 cells each containing 141 sarcomeres each connected by 3 gap junctions in the longitudinal direction and 1 gap junction in the transversal direction. The strength of coupling through these gap junctions is $\tau_{gap} = 0.3$ s. The internal coupling strengths are $\tau_c = 0.0261$ s and $\tau_{sr} = 0.15$ s with pacing period $T_p = 0.9$ s in all cases. Cell boundaries are in magenta with gap junctions in white. All other parameters as in Appendix A.

5.3.2 A Network Of Cells With Dominant Internal Sarcoplasmic Reticulum Coupling

Having looked at the case when cytosolic coupling is internally dominant in all the myocytes, we now consider a network of myocytes where the internal coupling is SR dominant. Our first example, seen in Figure 5.9, considers the case where the coupling through the gap junctions is weak. Each cell has a slight variation on the spatial pattern that is driven by the internal coupling strengths. This suggests that the presence of gap junctions has little effect on the behaviour of the system.

However, as with internal dominant cytosolic, the eigenvectors shown in Figure 5.10 reveal a small role for the gap junctions in driving the spatial behaviour. It is this small role that explains the variance we see in the range of peak subsarcolemmal Ca^{2+} concentrations between myocytes. Again, when there are no gap junctions, the network has a similar family of six eigenvectors to that seen in Figure 5.7. However, as seen in Figure 5.10, the eigenvectors of this system are not like those seen in Figure 5.7. This demonstrates that, much like with dominant cytosolic coupling, the introduction of gap junctions introduces different unstable eigenvectors. Furthermore, comparing the simulation results in Figure 5.9 to the eigenvectors in Figure 5.10 we see that the behaviour is not influenced by just a single eigenvector but most likely a linear combination of some of them. Thus, as with the case where all the myocytes have internal dominant cytosolic coupling, the introduction of gap junctions appears to lessen the ability to use linear stability analysis to predict the behaviour of the system.

In Section 5.3.1 we found that as the coupling strength through the gap junctions increased, so did its influence over the eigenvectors. By doing the same with the case of all myocytes having dominant SR coupling internally, we find again that the gap junctions have a major influence, but not in the same way. The results from two simulation with stronger coupling through the gap junctions, along with the eigenvectors of the system simulated, are depicted in Figures 5.11 and 5.12.

The results displayed in Figure 5.11 are from a network where the strength of coupling through the gap junctions is $\tau_{\text{gap}} = 10$. This is the same strength

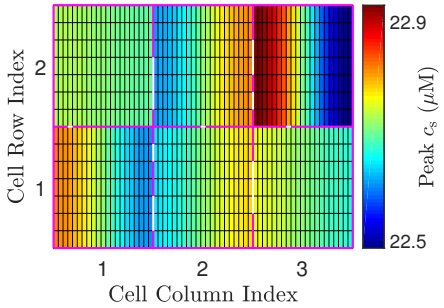

Figure 5.9: Simulation results from a network of cells with dominant internal SR coupling connected by gap junctions with a weak coupling strength. Peak subsarcolemmal Ca^{2+} concentrations from a single pacing period in a network of 6 cells each containing 141 sarcomeres each connected by 3 gap junctions in the longitudinal direction and 1 gap junction in the transversal direction. The strength of coupling through these gap junctions is $\tau_{\text{gap}} = 100$ s. The internal coupling strengths are $\tau_{\text{c}} = 1$ s and $\tau_{\text{sr}} = 0.05$ s with pacing period $T_p = 0.9$ s in all cases. Cell boundaries are in magenta with gap junctions in white. All other parameters as in Appendix A.

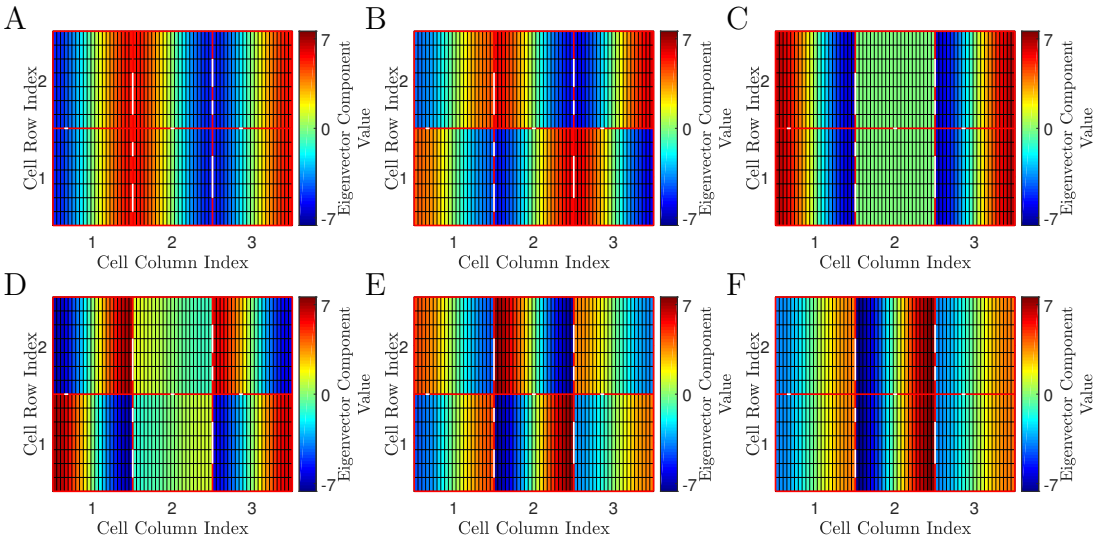

Figure 5.10: The values of the components in the unstable eigenvectors related to all the subsarcolemmal Ca^{2+} concentrations within the network for the simulations shown in Figure 5.9.

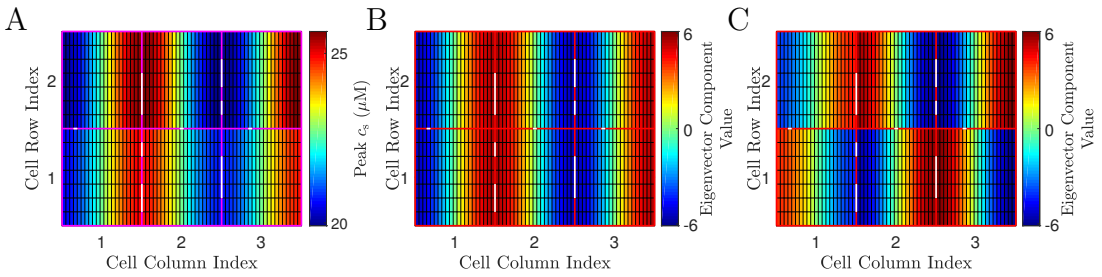

Figure 5.11: Simulation and stability analysis results for a system consisting of network of cells with dominant internal SR coupling connected by gap junctions with a stronger coupling strength than that used to create Figure 5.9. Peak subsarcolemmal Ca^{2+} concentrations from a single pacing period (A) and the unstable eigenvectors (B,C) from a network of 6 cells each containing 141 sarcomeres each connected by 3 gap junctions in the longitudinal direction and 1 gap junction in the transversal direction. The strength of coupling through these gap junctions is $\tau_{\text{gap}} = 10$ s. The internal coupling strengths are $\tau_{\text{c}} = 1$ s and $\tau_{\text{sr}} = 0.05$ s with pacing period $T_p = 0.9$ s in all cases. Cell boundaries are in magenta with gap junctions in white. All other parameters as in Appendix A.

as used to produce Figure 5.5, but unlike Figure 5.5 the number of unstable eigenvectors that dictate the behaviour of the system is now just two. This means that the strength of coupling through the gap junctions has a very different effect on systems in which SR coupling is the dominant form of internal coupling than those with dominant cytosolic coupling. Furthermore, coupling through the gap junctions is still relatively weak, illustrating that the unstable behaviour for networks of myocytes whose internal coupling is SR dominant are highly sensitive to coupling through gap junctions. An interesting effect of this reduction in the number of unstable eigenvectors, relates to the difference in the largest and smallest peak subsarcolemmal Ca^{2+} concentrations in Figure 5.11A compared to Figure 5.9A. As we can see in Figure 5.11A this difference is much greater, particularly in the top row of myocytes. This can be understood when we considering the two eigenvectors in Figures 5.11B and 5.11C in which the spatial patterns of the eigenvectors are the same for the top row but different for the bottom. Due to such similarities in these two eigenvectors they make the behaviour of a simulation more predictable. This suggests that increasing the strength of coupling through the gap junctions may have an advantage in networks of myocytes with internal SR dominant coupling in terms of our ability to predict the systems behaviour through the unstable eigenvectors.

Figure 5.12 reveals that when we increase the gap junction coupling strength

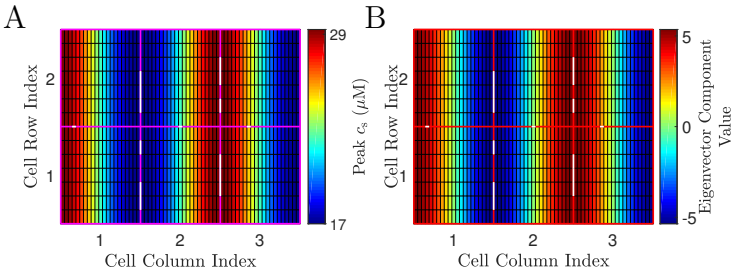

Figure 5.12: Simulation and stability analysis results for a system consisting of network of cells with dominant internal SR coupling connected by gap junctions with a stronger coupling strength than that used to create Figure 5.11. Peak subsarcolemmal Ca^{2+} concentrations from a single pacing period (A) and the values of the components in the unstable eigenvector related to all the subsarcolemmal Ca^{2+} concentrations (B) from a network of 6 cells each containing 141 sarcomeres each connected by 3 gap junctions in the longitudinal direction and 1 gap junction in the transversal direction. The strength of coupling through these gap junctions is $\tau_{\text{gap}} = 5 \times 10^{-7}$ s. The internal coupling strengths are $\tau_{\text{c}} = 1$ s and $\tau_{\text{sr}} = 0.05$ s with pacing period $T_p = 0.9$ s in all cases. Cell boundaries are in magenta with gap junctions in white. All other parameters as in Appendix A.

even further, we find the unstable behaviour of the system is now dominated by just one eigenvector. Interestingly this single unstable eigenvector appears to remain even under very strong coupling. For example, the coupling strength used in Figure 5.12 is $\tau_{\text{gap}} = 5 \times 10^{-7}$ s. This is far stronger than the coupling strength used in Section 5.2 for the gap junctions alone to drive a period-doubling orbit. Thus, it appears that when all the myocytes have internally dominant SR coupling the gap junctions cannot eliminate behaviour related to dominant SR coupling or introduce alternans. However, when the coupling through the gap junctions is strong enough it does mean that the system's behaviour can be predicted by looking at a single eigenvector. Comparing the spatial patterning in Figures 5.12A and 5.12B gives an example of this. Hence, stronger gap junctional coupling could be deemed advantageous in a system where all the myocytes have SR dominant internal coupling.

5.3.3 A Network Of Cells With A Mixture Of Cells With Either Cytosolic Or Sarcoplasmic Reticulum Coupling Dominating

In this section we consider networks with a mixture of myocytes with internal coupling that is either dominant cytosolic or dominant SR. We begin by focusing on networks with an even split with three cells that have dominant cytosolic

internal coupling and three cell that have dominant SR internal coupling. We will consider three different layouts: a row of each type stacked in the transversal direction, each type focused around a corner of the network and a checkerboard pattern between the two types. All three of these scenarios can be seen in Figure 5.13. For example Figure 5.13A contains results from a simulation of the row scenario, Figure 5.13B contains results from the corners scenario and Figure 5.13C contains results from the checkerboard scenario.

The findings in Figure 5.13 are taken from a simulation of each scenario with weak coupling through the gap junctions. The plots in Figure 5.13 show a single pacing period and depict the peak subsarcolemmal Ca^{2+} concentrations in each sarcomere. Figures 5.13D-F are results taken from the same pacing period as that shown in Figures 5.13A-C. The only difference between these two sets of figures is the limits used for the colour bar which has been adjusted in Figures 5.13D-F. This adjustment allows the behaviour in the myocytes with dominant SR coupling to be discerned visually.

From Figure 5.13 we see that the behaviour associated with the form of internal coupling remains mainly intact with the introduction of weak gap junctions coupling. This is similar to our studies of the myocyte networks in which all the myocytes have the same form of internal coupling. However, there appears to be slight nuances in the spatial patterning when moving between myocytes. The reasons behind this become apparent when looking at the eigenvectors of the system. To explain this we only need to consider the eigenvectors, seen in Figure 5.14, related to the three eigenvalues that lie outside the unit circle in the negative direction. We find these eigenvectors only provide insight into the spatial behaviour of the myocytes with dominant cytosolic internal coupling. These systems also contains three eigenvectors, not shown here, that provide insight into the spatial behaviour of the myocytes with dominant SR internal coupling. The unshown eigenvectors are linked to eigenvalues lying outside the unit circle in the positive direction. An important point to note from this, is that each individual eigenvector only ever contains information on the form of spatial behaviour linked to one form of dominant internal coupling. Comparing these eigenvectors to the behaviour in Figure 5.13 we see some interesting differences between the three

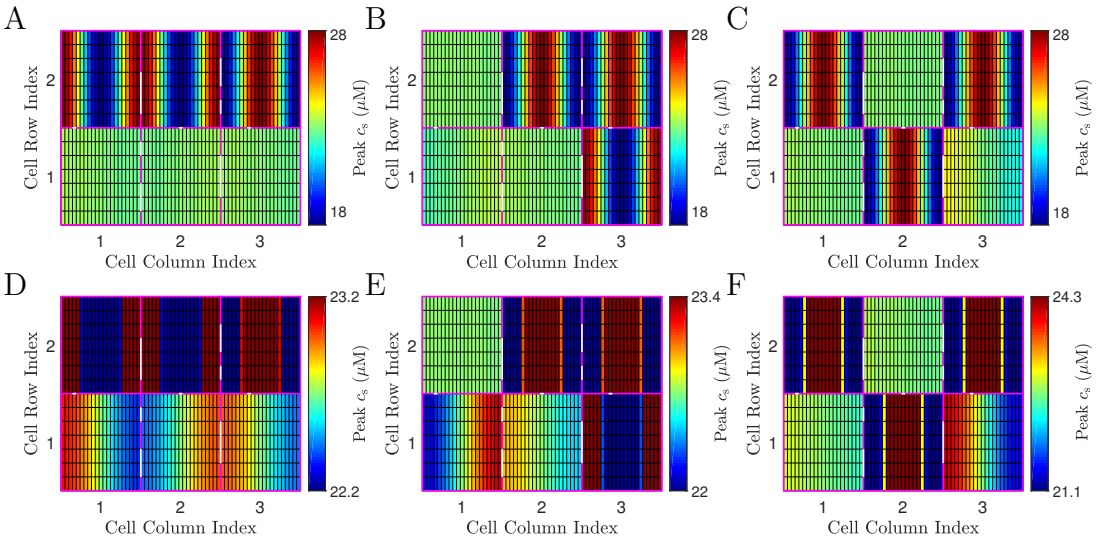

Figure 5.13: Simulation results for three different systems, each consisting of a network of cells with an even mix of cells with either internal dominant cytosolic or SR coupling connected by gap junctions with a weak coupling strength. Peak subsarcolemmal Ca^{2+} concentrations from a single pacing period in a network of 6 cells each containing 141 sarcomeres each connected by 3 gap junctions in the longitudinal direction and 1 gap junction in the transversal direction. The strength of coupling through the gap junctions $\tau_{\text{gap}} = 200$ s. The internal coupling strengths are either $\tau_{\text{c}} = 0.0261$ s and $\tau_{\text{sr}} = 0.15$ s or $\tau_{\text{c}} = 1$ s and $\tau_{\text{sr}} = 0.05$ s with pacing period $T_p = 0.9$ s in all cases. The limits in D-F are adjusted so that the behaviour in the myocytes with dominant SR coupling is clearer. All other parameters as in Appendix A. See text for further details.

scenarios.

One point of interest between the scenarios relates to the eigenvectors. Whilst each eigenvector for the rows and corners scenarios give information for all the myocytes with the same form of internal coupling, we do not see this with the checkerboard scenario. As can be seen in Figures 5.14G-I, the eigenvectors are reminiscent of the uncoupled case originally plotted in Figure 5.7. This implies that the behaviour is much more predictable from the eigenvectors in the checkerboard scenario. This is further supported by comparing the dominant cytosolic behaviour in Figure 5.13C to the eigenvectors on show in Figures 5.14G-I. Interestingly, the behaviour in the dominant SR coupled myocytes seen in Figures 5.13F alludes to another finding in terms of the differences between dominant SR coupling and dominant cytosolic coupling. From our simulations, unless the initial conditions lie close to a dominant SR linked eigenvector, we find that the transient period for spatial alternans is much shorter than that of the behaviour found in myocytes with dominant SR coupling. The biological implications of this needs further research, particularly focusing on the effect on the voltage when it is not clamped.

Now since we have seen how the system behaves when the coupling through the gap junctions is weak, we seek to understand what happens as we increase the coupling strength. In Section 5.3.2 we saw how an increase in the coupling strength reduced the number of unstable eigenvectors down to one in a network of myocytes which all had dominant SR internal coupling. Furthermore, we found that this single eigenvector remained even under very strong coupling. However, Figure 5.15 reveals that when some myocytes have cytosolic coupling as their dominant form of internal coupling this no longer remains the case.

Figure 5.15 represents the results from simulations of the three different scenarios, first shown in Figure 5.13, where there are no eigenvalues lying outside the unit circle in the positive direction. In each case the coupling strength of the gap junctions used is close to the gap junctional strength at which the most positive eigenvalue moves just inside the unit circle. Hence, the behaviour is only driven by the unstable eigenvectors shown in Figure 5.14 and not any others. Comparing all three plots in Figure 5.15, we can see that the myocytes with in-

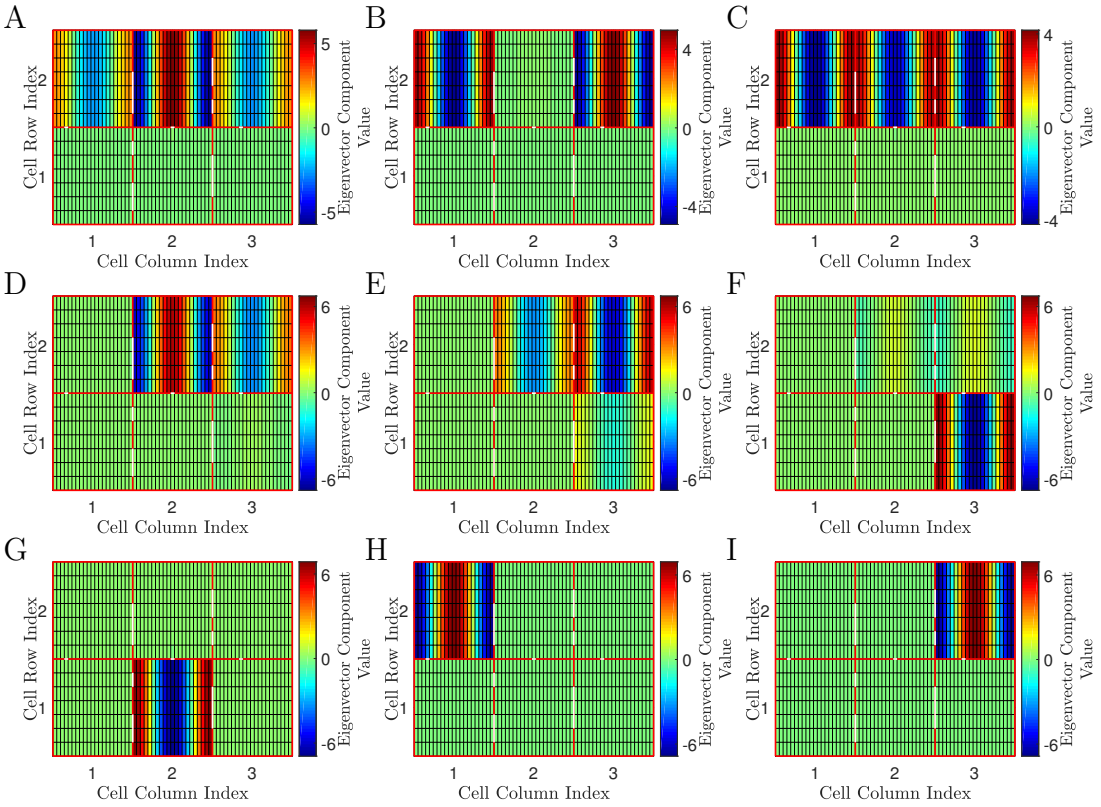

Figure 5.14: The values of the components in the unstable eigenvectors related to all the subsarcolemmal Ca^{2+} concentrations within the network linked to the eigenvalues lying outside the unit circle in the negative direction for the systems used to create Figure 5.13. These plots relate to the simulations shown in Figures 5.13A and 5.13D (A-C), Figures 5.13B and 5.13E (D-F) and Figures 5.13C and 5.13F (G-I).

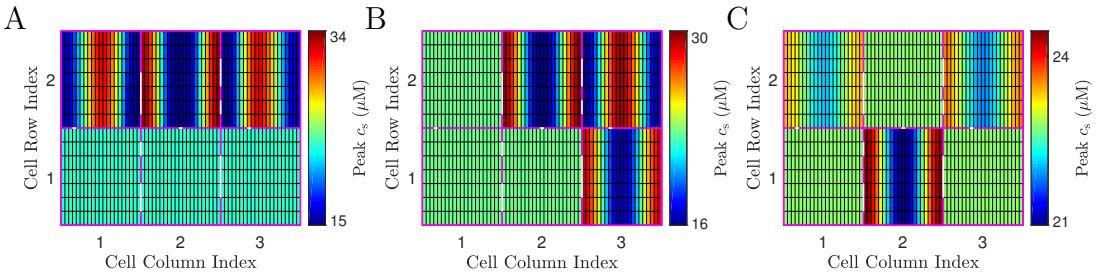

Figure 5.15: Simulation results for three different systems, each consisting of a network of cells with an even mix of cells with either internal dominant cytosolic or SR coupling connected by gap junctions with a stronger coupling strength than that used for Figure 5.13. Peak subsarcolemmal Ca^{2+} concentrations from a single pacing period in a network of 6 cells each containing 141 sarcomeres each connected by 3 gap junctions in the longitudinal direction and 1 gap junction in the transversal direction. The strength of coupling through these gap junctions are $\tau_{\text{gap}} = 1$ s (A), $\tau_{\text{gap}} = 5$ s (B) and $\tau_{\text{gap}} = 10$ s (C). The internal coupling strengths are either $\tau_{\text{c}} = 0.0261$ s and $\tau_{\text{sr}} = 0.15$ s or $\tau_{\text{c}} = 1$ s and $\tau_{\text{sr}} = 0.05$ s with pacing period $T_p = 0.9$ s in all cases. Cell boundaries are in magenta with gap junctions in white. All other parameters as in Appendix A.

ternal SR dominant coupling are stabilised. Interestingly, for each scenario the strength required for this to occur is substantially different, with the row scenario in Figure 5.15A requiring the strongest and the checkerboard scenario in Figure 5.15A requiring the weakest. This suggest that whilst the number of internally cytosolic dominant myocytes may have an effect, the number of borders and gap junctions between the two type of cells are also key in stabilising any behaviour related to a '+1' bifurcation.

Figure 5.16 illustrates the three different scenarios with a coupling strength $\tau_{\text{gap}} = 0.1$ through the gap junctions. Now comparing the three scenarios we see two major differences. The first difference we consider focuses around the myocytes that have dominant cytosolic internal coupling, for example the top row of Figure 5.16A. Looking across all three plots in Figure 5.16, we see that these myocytes all still have similar patterns for the spatially discordant alternans but the amplitude of these alternans varies between each scenario. We find the biggest amplitude in the network with the row scenario, then the amplitude is slightly smaller in the corners scenario before being at its smallest in the checkerboard scenario.

On the other hand if we focus on the myocytes that have internal SR dominant coupling, we see that the spatial alternans begin to form in these cells. Furthermore, these alternans appears to be greater in amplitude nearer the gap junctions. Moreover, comparing all three plots in Figure 5.16 we find that the amplitude size varies between these plots, with the largest amplitude found in the checkerboard scenario and the smallest in the row scenario. Putting these two differences together suggests that the amplitude differences are driven by the placement and number of gap junctions along the borders between the two types of cells.

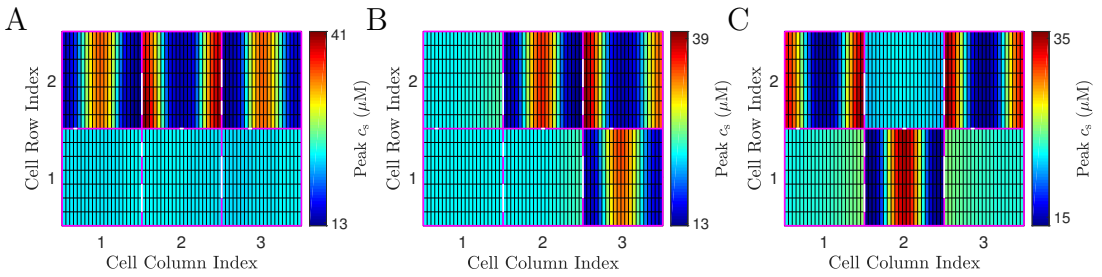

Figure 5.16: Simulation results for three different systems, each consisting of a network of cells with an even mix of cells with either internal dominant cytosolic or SR coupling connected by gap junctions with a stronger coupling strength than that used for Figure 5.15. Peak subsarcolemmal Ca^{2+} concentrations from a single pacing period in a network of 6 cells each containing 141 sarcomeres each connected by 3 gap junctions in the longitudinal direction and 1 gap junction in the transversal direction. The strength of coupling through these gap junctions is $\tau_{\text{gap}} = 0.1$ s. The internal coupling strengths are either $\tau_{\text{c}} = 0.0261$ s and $\tau_{\text{sr}} = 0.15$ s or $\tau_{\text{c}} = 1$ s and $\tau_{\text{sr}} = 0.05$ s with pacing period $T_p = 0.9$ s in all cases. Cell boundaries are in magenta with gap junctions in white. All other parameters as in Appendix A.

5.4 The Effect Of Gap Junctions In A Network With A Mix Of Stable and Unstable Cells

To finish this chapter we introduce some myocytes with balanced internal coupling into networks that have myocytes with either dominant cytosolic or dominant SR internal coupling. We will begin by looking at a network under weak gap junctional coupling to see if the the behaviour of the unstable cells can affect the behaviour of the stable cells through the gap junctions. For simplicity we consider a network which contains six myocytes, with two each containing a form of internal coupling. The two left hand myocytes have dominant SR internal coupling, the two central myocytes have balanced coupling and the two right myocytes have dominant cytosolic internal coupling.

Figure 5.17 displays the peak subsarcolemmal Ca^{2+} concentrations from a single pacing period within these simulations. Both Figure 5.17A and Figure 5.17B are taken from the same pacing period, with the limits for the colour bar in Figure 5.17B adjusted so that the behaviour in the myocytes with SR dominant internal coupling is clearer. As in Section 5.3.3, Figure 5.17 illustrates that the amplitude of the spatial alternans is greater than the amplitude of the spatial variance of the single period orbits found in the SR dominant myocytes.

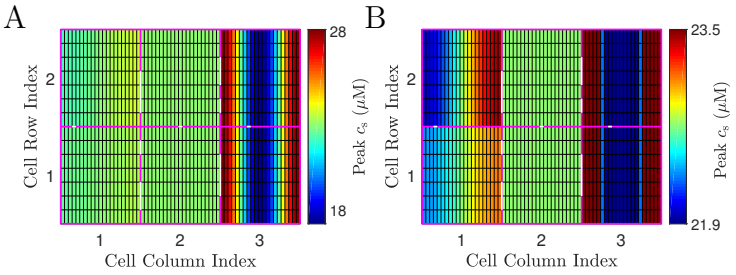

Figure 5.17: Simulation results from a network of cells with an even mix of cells with balanced coupling or either internal dominant cytosolic or SR coupling connected by gap junctions with a weak coupling strength. Peak subsarcolemmal Ca^{2+} concentrations from a single pacing period in a network of 6 cells each containing 141 sarcomeres each connected by 3 gap junctions in the longitudinal direction and 1 gap junction in the transversal direction. The strength of coupling through the gap junctions $\tau_{\text{gap}} = 200$ s. The internal coupling strengths working left to right are $\tau_{\text{c}} = 1$ s and $\tau_{\text{sr}} = 0.05$ s, $\tau_{\text{c}} = 0.05$ s and $\tau_{\text{sr}} = 0.1$ s, $\tau_{\text{c}} = 0.0261$ s and $\tau_{\text{sr}} = 0.15$ s with pacing period $T_p = 0.9$ s in all cases. The limits in D-F are adjusted so that the behaviour in the myocytes with dominant SR coupling is clearer. All other parameters as in Appendix A.

The simulations also once again reveal that the spatial alternans form at a much faster rate than the behaviour found in the SR dominant cells.

Figure 5.17 also suggests that the behaviour in the central two cells still follows that of the synchronised single-period orbit. However, the use of a linear term for our coupling through the gap junctions would suggest this cannot be the case. For example, if we consider the right hand side of the central myocytes, this side of the gap junction would be following a single-period orbit whilst the far right myocytes would be following a period doubling orbit. This would create a difference in the amount of Ca^{2+} passing between the two each pacing period preventing a synchronised single period orbit. Using our stability analysis to study the parts of the unstable eigenvectors related to these myocytes reveals that the orbits of the sarcomeres are indeed slightly perturbed away from the synchronised state. However, the size of the perturbation is negligible when compared to the behaviour occurring in the other myocytes.

Despite the introduction of myocytes with balanced coupling separating the SR and cytosolic dominant myocytes, the simulation results and unstable eigenvectors shown in Figure 5.18 demonstrates that with strong enough coupling through the gap junctions, the behaviour associated with internal SR dominated coupling is eliminated from the system. Whilst the gap junction coupling strength

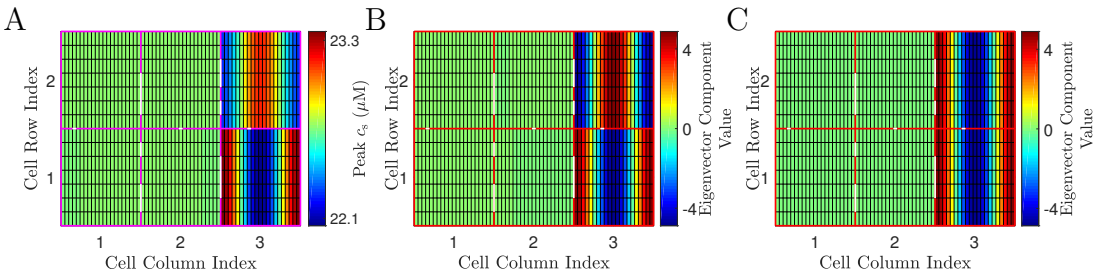

Figure 5.18: Simulation and stability analysis results for a system consisting of a network of cells with an even mix of cells with balanced coupling or either internal dominant cytosolic or SR coupling connected by gap junctions with a stronger coupling strength than that used for Figure 5.17. Peak subsarcolemmal Ca^{2+} concentrations from a single pacing period (A) and the values of the components in the unstable eigenvectors related to all the subsarcolemmal Ca^{2+} concentrations (B,C) in a network of 6 cells each containing 141 sarcomeres each connected by 3 gap junctions in the longitudinal direction and 1 gap junction in the transversal direction. The strength of coupling through the gap junctions $\tau_{\text{gap}} = 15$ s. The internal coupling strengths working left to right are $\tau_{\text{c}} = 1$ s and $\tau_{\text{sr}} = 0.05$ s, $\tau_{\text{c}} = 0.05$ s and $\tau_{\text{sr}} = 0.1$ s, $\tau_{\text{c}} = 0.0261$ s and $\tau_{\text{sr}} = 0.15$ s with pacing period $T_p = 0.9$ s in all cases. . All other parameters as in Appendix A.

is increased enough to eliminate such behaviour, the eigenvectors in Figures 5.18B and 5.18C tell us that any behaviour driven by the unstable eigenvectors in the myocytes with balanced internal coupling is still negligible when compared to the spatial alternans in the myocytes with dominant cytosolic internal coupling. This suggests that the coupling strength of the gap junction itself has more of an influence on the behaviour of a myocyte with balanced internal coupling, as seen in Section 5.2, as opposed to behaviour of the myocyte to which it is coupled.

Although these findings inform us that the coupling strength of the gap junctions is the main influence upon myocytes with balanced internal coupling, throughout this chapter we have seen that the myocytes with internal SR dominant coupling can be influenced by a majority of factors. In Section 5.3.2 we saw that in a network of myocytes that contain dominant SR dominant coupling, the network does not return to a synchronised single-period state even under very strong gap junctional coupling. However, the behaviour related to internal SR dominant coupling can be eliminated in networks that also contain internal cytosolic dominant coupling. As Figure 5.18 reveals, this occurs even when the myocytes with internal SR dominant and internal cytosolic dominant coupling are separated by myocytes with balanced coupling. Such a finding begs two questions. The first is

whether such a loss of behaviour can occur in a network containing just myocytes with internal balanced coupling. The second is if the balanced myocytes do have an effect, how does it compare to the effect of myocytes with internal cytosolic dominant coupling.

We have begun by looking for an example of a network containing one myocyte with internal balanced coupling, whilst the rest of the myocytes have internal SR dominant coupling, that stabilises to a synchronous single-period state under strong gap junctional coupling. Figure 5.19 provides such an example. Figure 5.19A, which shows the peak subsarcolemmal Ca^{2+} concentrations from a single pacing period, illustrates that the system follows a synchronised single-period state. Furthermore, Figure 5.19B confirms that the key eigenvalue now lies within the unit circle and thus the synchronous single-period state is stable. We also note that this stable state occurs with a coupling strength $\tau_{\text{gap}} = 0.1$ s, a much weaker coupling parameter than that used to create Figure 5.12. This demonstrates the power of introducing a myocyte without dominant internal SR coupling into the mix.

We have established that the presence of at least one myocyte with internal balanced coupling can lead to a stable synchronised single-period state, in a network otherwise consisting of myocytes with internal SR dominant coupling, when gap junction coupling is strong enough. We now consider whether having dominant cytosolic coupling within a single myocyte, in a network otherwise consisting of myocytes with internal SR dominant coupling, alters the gap junction coupling strength at which the most positive eigenvalue moves just inside the unit circle. To do this we have studied the behaviour of a network with a single myocyte that has internal dominant cytosolic coupling and a system with a single myocyte under balanced coupling. In both these networks, the rest of the myocytes have internal SR dominant coupling. We have chosen gap junction coupling strengths slightly weaker than the gap junction coupling strength required to move the most positive eigenvalue just inside the unit circle. This allows us to compare the behaviour of each network just before the dominant SR related behaviour is eliminated. The results of a simulation based on each case are shown in Figure 5.20.

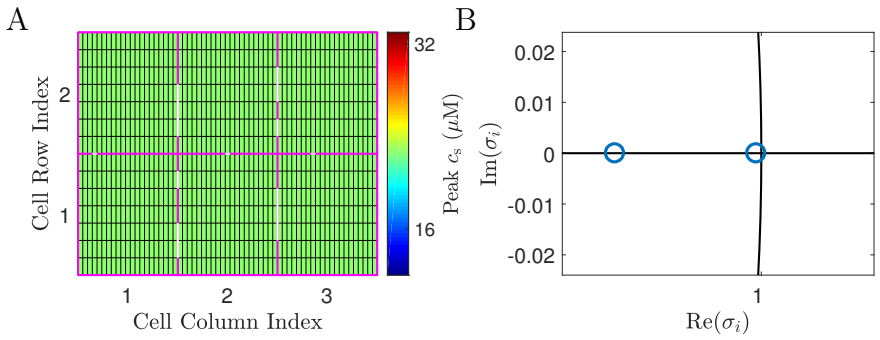

Figure 5.19: Simulation and stability analysis results for a system consisting of a network of cells with a mix of cells with either balanced coupling or internal dominant SR coupling connected by gap junctions with a strong coupling strength. Peak subsarcolemmal Ca^{2+} concentrations from a single pacing period (A) and the eigenvalue lying closest to the edge of the unit circle (B) in a network of 6 cells each containing 141 sarcomeres each connected by 3 gap junctions in the longitudinal direction and 1 gap junction in the transversal direction. The strength of coupling through the gap junctions $\tau_{\text{gap}} = 0.1$ s. The internal coupling strengths are $\tau_{\text{c}} = 1$ s and $\tau_{\text{sr}} = 0.05$ s or $\tau_{\text{c}} = 0.05$ s and $\tau_{\text{sr}} = 0.1$ s with pacing period $T_p = 0.9$ s. All other parameters as in Appendix A.

As Figure 5.20 reveals the behaviour related to SR dominant coupling still occurs under strong gap junctional coupling considering that $\tau_{\text{gap}} = 0.3$ in the top row and $\tau_{\text{gap}} = 0.32$ in the bottom row. This reveals that when there are more myocytes with internal SR dominant coupling in the system compared to the other types, the stronger the gap junction strength needs to be to eliminate the behaviour related to these myocytes. We also note the slight difference in value for the gap junctional strength between the two. This stems from the fact that both these simulations have been performed with gap junction coupling strengths close to the value of the gap junctional strength at which the the SR dominant related behaviour is stabilised. When stating that the SR dominant related behaviour has been stabilised we are referring to the scenario at which there are no longer any eigenvalues of the system lying outside the unit circle in the positive direction. In the case of a network where the non-SR dominant myocyte has dominant cytosolic coupling, when $\tau_{\text{gap}} = 0.3$ the SR dominant behaviour has already been lost. This reveals that the form of internal coupling in a myocyte with non-SR dominant internal coupling does have an affect on the coupling strength of the gap junction needed to eliminate such behaviour, but this effect is small.

In Section 5.3.3 we saw that in a network with equal number of myocytes

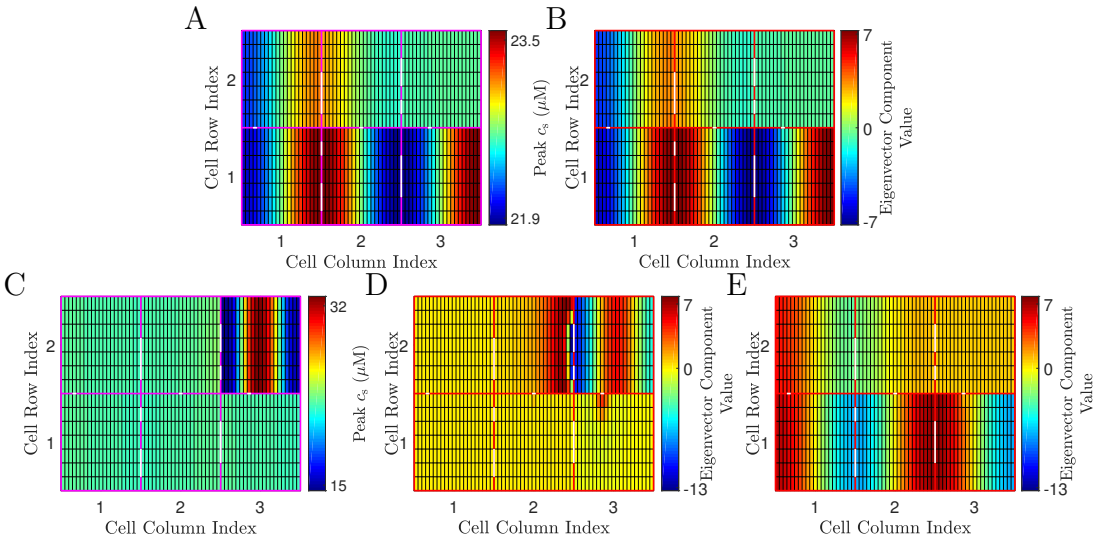

Figure 5.20: A comparison of networks with 5 cells containing internal SR dominant coupling and one cell with either balanced coupling or internal cytosolic dominant coupling. Peak subsarcolemmal Ca^{2+} concentrations (A,C) from a single pacing period from a network of 6 cells each containing 141 sarcomeres each connected by 3 gap junctions in the longitudinal direction and 1 gap junction in the transversal direction. All the myocytes have internal SR dominant coupling bar one myocyte with balanced coupling (A) or one with internal dominant cytosolic coupling (C). The values of the components in the unstable eigenvector related to all the subsarcolemmal Ca^{2+} concentrations within these networks are in B or D and E respectively. The strength of coupling through the gap junctions is $\tau_{\text{gap}} = 0.3$ s (A,B) or $\tau_{\text{gap}} = 0.32$ s (C,D,E). The internal coupling strengths are $\tau_{\text{c}} = 1$ s and $\tau_{\text{sr}} = 0.05$ s for the SR dominant myocytes and $\tau_{\text{c}} = 0.05$ s and $\tau_{\text{sr}} = 0.1$ s (A,B) or $\tau_{\text{c}} = 0.0261$ s and $\tau_{\text{sr}} = 0.15$ s (C,D,E) in the non-dominant SR myocyte with pacing period $T_p = 0.9$ s. All other parameters as in Appendix A.

with dominant SR internal coupling and dominant cytosolic internal coupling, spatial alternans would only begin to occur in the myocytes with dominant SR internal coupling at gap junction coupling strengths much greater than those needed to stabilise the behaviour related to the dominant SR coupling. However, the eigenvectors in Figures 5.20D and 5.20E reveal that this is no longer the case. We find that since the behaviour related to SR dominant internal coupling still occurs at high gap junction coupling strengths, we now have a scenario where both spatial alternans and behaviour related to the SR dominant coupling can occur in the same myocyte. A clearer view of this is shown in Figure 5.21.

Focusing on the cental myocyte in the top row of the network, Figures 5.21A and 5.21B illustrate how the two unstable eigenvectors shown in Figures 5.20D and 5.20E drive two separate behaviours within this single myocyte. Going from one pacing period to the next, we see that the left hand side follows a single-period orbit whilst the right shows alternans. This is even clearer in Figure 5.21C which portrays the trajectories of the subsarcolemmal Ca^{2+} concentration from a sarcomere at each end of this myocyte. The consequences of such a mismatch in behaviours within a myocyte require further research beyond the scope of this thesis.

Our final consideration is whether myocytes in the network that are not direct neighbours of a myocyte with internal dominant SR coupling have an affect on the strength of gap junctional coupling needed to eliminate behaviour related to dominant SR coupling. To do this we have taken a network of three myocytes, each with a different balance of internal coupling. Since we have seen how myocytes with dominant cytosolic internal coupling reduces the strength of gap junctional coupling required to eliminate behaviour related to dominant SR coupling, we separate these two types of myocyte by a myocyte with balanced coupling. A diagram of the set up can be seen in Figure 5.22. We compare the gap junction coupling strength required to eliminate behaviour related to dominant SR coupling in this network with the strength required for the a network containing seven myocytes with balanced internal coupling in the middle.

Figure 5.23 depicts the results of this comparison which we discern from the eigenvalues of the system. As Figures 5.23A and 5.23B confirms, both systems

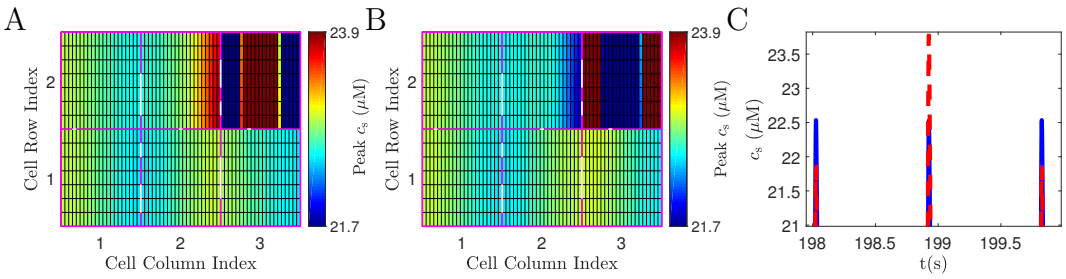

Figure 5.21: Simulation results from a system consisting of a network with five cells containing internal SR dominant coupling and one cell with internal cytosolic dominant coupling connected by gap junctions with strong coupling strength. Peak subsarcolemmal Ca^{2+} concentrations (A,B) from two consecutive pacing periods from a network of 6 cells each containing 141 sarcomeres each connected by 3 gap junctions in the longitudinal direction and 1 gap junction in the transversal direction. All the myocytes have internal SR dominant coupling bar one with internal dominant cytosolic coupling. Colour bar limits have been adjusted to focus on myocytes with SR dominant coupling. Subsarcolemmal Ca^{2+} concentration against time from two sarcomeres at opposite ends of the myocyte in middle of the top row are shown in C. The strength of coupling through the gap junctions is $\tau_{\text{gap}} = 0.32$ s. The internal coupling strengths are $\tau_{\text{c}} = 1$ s and $\tau_{\text{sr}} = 0.05$ s for the SR dominant myocytes and $\tau_{\text{c}} = 0.0261$ s and $\tau_{\text{sr}} = 0.15$ s in the dominant cytosolic myocyte with pacing period $T_p = 0.9$ s. All other parameters as in Appendix A.

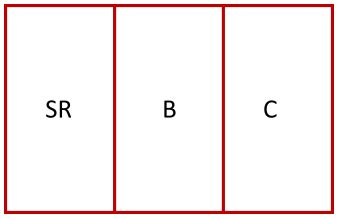

Figure 5.22: Diagram showing set ups of a network of myocytes to be used to study if the distance between a myocyte with dominant SR internal coupling and dominant cytosolic internal coupling can affect the gap junctional strength needed to eliminate behaviour related to SR dominant coupling. SR stands for dominant SR coupling, B for balanced coupling and C for dominant cytosolic coupling.

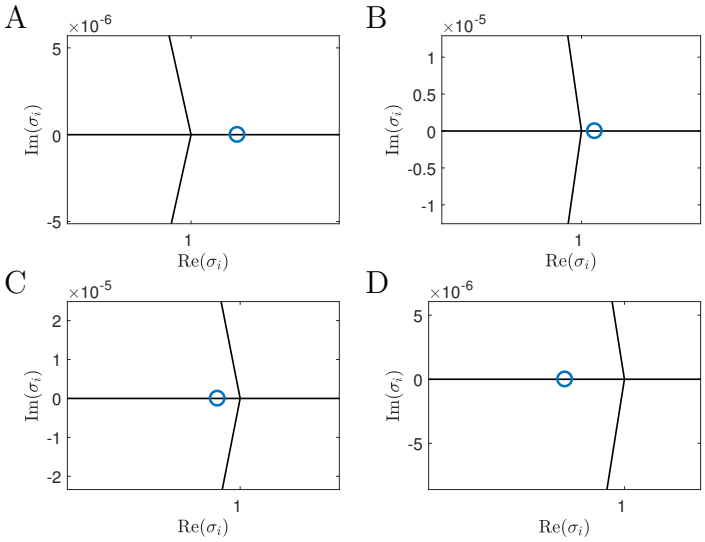

Figure 5.23: Most positive eigenvalue from a network of 3 cells (A,C) and 9 cells (B,D) each containing 141 sarcomeres each connected by 3 gap junctions in the longitudinal direction. The strength of coupling through the gap junctions is $\tau_{\text{gap}} = 16.809$ s (A,B) and $\tau_{\text{gap}} = 16.808$ s (C,D). The internal coupling strengths are $\tau_{\text{c}} = 1$ s and $\tau_{\text{sr}} = 0.05$ s for the SR dominant myocytes, $\tau_{\text{c}} = 0.05$ s and $\tau_{\text{sr}} = 0.1$ s for the balanced myocytes and $\tau_{\text{c}} = 0.0261$ s and $\tau_{\text{sr}} = 0.15$ s in the dominant cytosolic myocyte with pacing period $T_p = 0.9$ s. All other parameters as in Appendix A.

contain an unstable eigenvector related to the dominant SR coupling under the same gap junctional coupling strength ($\tau_{\text{gap}} = 16.809$ s). We have deduced this since Figures 5.23A and 5.23B display an eigenvalue lying outside the unit circle in the real, positive direction. However, both Figures 5.23C and 5.23D reveal the behaviour related to SR dominant internal coupling is stabilised due to a minimal decrease in the value of the coupling parameter ($\tau_{\text{gap}} = 16.808$ s). This equates to a small increase in the gap junction coupling strength and tells us that if it is not directly connected to a dominant SR internally coupled myocyte, a dominant cytosolic internally coupled myocyte has no effect on the gap junction strength required to stabilise behaviour related to a dominant SR coupling. Coupling this with our other findings, we now know that the number and placement of gap junctions, along with how many myocytes, and which form of internal coupling they have, are directly linked to myocytes with SR dominant coupling via gap junctions are the key factors to consider when trying to stabilise behaviour related to dominant SR coupling.

5.5 Summary

In Section 2.1.3 we discussed how the role of Ca^{2+} diffusion between cardiac myocytes via gap junctions is currently disputed. Thus any conclusions drawn from this chapter remain based on a theoretical scenario but with evidence [19] suggesting Ca^{2+} diffusion through cardiac gap junctions is possible, such a scenario may not remain theoretical. Our first results, discussed in Section 5.2, focused around the role of gap junctions in a network where the internal coupling means each myocyte has a stable synchronised state with each sarcomere following the same single-period orbit. Our studies revealed that, under strong enough coupling, these gap junctions could produce a period-doubling bifurcation. Furthermore, we saw that this bifurcation would produce spatial alternans and that the spatial alternans with largest amplitude occurred around the boundary with the largest spread of gap junctions. Moreover, we found that an increase in the number of gap junctions at a boundary would decrease the strength of coupling through the gap junctions needed for a period-doubling bifurcation to occur.

Having established this we turned our attention to networks of myocytes all containing either dominant cytosolic coupling or dominant SR coupling. In sections 5.3.1 and 5.3.2 we found that in networks with purely one form of internally dominant coupling that weakly coupled gap junctions would linearly combine the internal behaviour in varying ways. As such the myocytes would not necessarily have identical behaviour to other myocytes within the network. We also found that the network had the same number of unstable eigenvectors as the number of myocytes when the coupling strength through the gap junctions was weak enough. In Section 5.3.1 we found that as the gap junction coupling strength was increased the spatial patterns would change. We found that the region in the myocyte containing the alternans with largest amplitude would shift towards the areas closest to the gap junctions. On the other hand, in Section 5.3.2 we saw that when the internal coupling was SR dominant in all the myocytes, an increase in the coupling strength of the the gap junctions would decrease the number of unstable eigenvectors. Interestingly, the gap junctions appeared unable to remove the final unstable eigenvector and return the system to a synchronised state with each sarcomere following a single-period orbit. This was even the case when the

strength of coupling through the gap junctions was exceptionally strong. However, by reducing the number of unstable eigenvectors to one, it meant that we could predict the spatial pattern of the system.

In the final parts of this chapter we studied networks containing a mix of myocytes with internal SR dominant coupling, cytosolic dominant coupling or balanced coupling. These studies found that as long as one myocyte in the network did not have internal dominant SR coupling, the behaviour related to dominant SR coupling could be removed from the whole network if the coupling through the gap junctions was increased enough. Further to this we demonstrated that the number or placement of these non SR dominant myocytes could alter the strength needed through the gap junctions to eliminate any SR dominant related behaviour. On the other hand, in Section 5.4 we saw that the difference in the gap junction coupling strength required to eliminate SR dominant related behaviour was only marginally affected by whether a myocyte within the network had either dominant cytosolic coupling or balanced coupling. This became very apparent when comparing networks of myocytes that had a different number of myocytes with balanced coupling between the dominant SR coupled myocytes and dominant cytosolic coupled myocytes. As our study in Section 5.4 illustrated, the affect a myocyte has on any other myocyte that is not their neighbour is negligible.

Whilst our findings show a minimal difference between a myocyte with balanced coupling and dominant cytosolic coupling on the gap junction coupling strength at which behaviour related to SR dominant coupling is eliminated, it does not mean the presence of myocytes with dominant cytosolic coupling should be ignored. As we have found through our simulations, spatial alternans form much faster than the behaviour related to SR dominant coupling. As well as this, in Section 5.4 we demonstrated that when the number of myocytes with SR dominant coupling moderately outweighs the number of myocytes with dominant cytosolic coupling, a mix of behaviours can occur within a single myocyte. The mixture of behaviours was due to the ability of the dominant SR coupling behaviour to reside in the system under strong gap junctional coupling thanks to the larger number of myocytes with internal SR dominant coupling versus those

with a different balance of internal coupling. The consequences of these findings raise many questions, particularly what effects such findings would have on the voltage dynamics, that require further research beyond the scope of this thesis.

6 Discussion and Future Work

6.1 Role Of Calcium Diffusion

The major focus of this thesis, particularly in Chapters 3 and 4, has been on how intracellular Ca^{2+} diffusion can affect the stability of a synchronised state in subcellular networks. The forms of intracellular diffusion we have studied have been both cytosolic and SR diffusion between sarcomeres. Using both simulations and the stability approach laid out in Section 2.4, we have illustrated that when internal coupling is balanced and the pacing period is slow enough, the network follows a synchronised single-period orbit. Then, by increasing the strength of one of these forms of coupling, the system can undergo a of bifurcation whose nature is dependent upon the dominant form of coupling.

When the stronger form of coupling is cytosolic, the type of bifurcation is a period-doubling bifurcation. Whilst this has been confirmed previously [1], we were able to take this further in terms of the spatial patterns linked to the period-doubling bifurcation. By varying both coupling strengths in such a way that the system remained close to the point of a period-doubling bifurcation, we demonstrated that the spatial pattern at the onset of bifurcation could change. Some of these patterns are known as SDA. This was striking as there appears to be little to no evidence of SDA in a voltage clamped system without experimentally inducing calcium waves [114] or heterogeneity between sarcomeres [15]. The spatial patterns could be predicted by the eigenvector linked to the eigenvalue lying outside the unit circle.

In terms of dominant SR coupling, we showed that the synchronised single-period orbit underwent a '+1' bifurcation. Such a '+1' bifurcation led to the development of multiple new single-period orbits. These orbits have differing spatial structures as we move from one sarcomere to the next and, as with dominant cytosolic coupling, the spatial pattern of the system is dictated by the coupling strengths of both forms of coupling. Again, the spatial pattern is predicted by the eigenvector linked to the eigenvalue lying outside the unit circle. The predictive nature of these eigenvectors demonstrate the power of the stability approach shown in Section 2.4.

The appearance of a '+1' bifurcation and the behaviour it bestows upon the system is something that appears to have never been seen previously. Considering that it has been suggested that SR Ca^{2+} diffusion may indeed be faster than cytosolic Ca^{2+} diffusion [103], it is clear that the affect of such a bifurcation should be studied further. An obvious next step would be to consider introducing voltage dynamics. This would be particularly prudent in cases where the levels of Ca^{2+} are high in large regions of the myocyte due to their links to DADs [86]. Furthermore, it would be interesting to see whether the introduction of the voltage dynamics would introduce some new voltage behaviour or whether the regional differences in the free intracellular Ca^{2+} concentration could lead to APD alternans. This would reveal another key difference between the two forms of dominant coupling, in that dominant SR coupling needs voltage dynamics to drive alternans whilst dominant cytosolic coupling does not. However, in both cases the spatial pattern is driven by the Ca^{2+} dynamics.

Another avenue for further research into the '+1' bifurcation of the synchronised single-period orbit and its related behaviour was alluded to in Sections 4.1 and 4.2. In these sections we discussed how the '+1' bifurcation had a link to both the SERCA pump uptake strength and the timing of the steep release in the load-release function. We showed in Section 4.1 that the small area of bistability would disappear when the uptake strength is significantly lowered. Such a lowering of the uptake strength would prevent a steep release from the load-release function. This suggests the presence of steep release from the load-release function is related to the presence of the small area of bistability. Further to this, in Section 4.2 we discovered that when steep release from the load-release function does not occur at all, then a '+1' bifurcation cannot take place. Considering that the timing of the steep release from the load-release function is intrinsically linked to the uptake strength, understanding how this relationship affects the '+1' bifurcation requires further development. These findings for both dominant SR coupling, along with dominant cytosolic coupling, are summarised in Table 1.

As well as studying networks of sarcomeres at pacing periods where the synchronised single-period orbit is stable, in Section 4.4 we considered pacing periods where SCA is a stable. We first established that SCA was a stable synchronised

Start of steep release from load-release function	Dominant cytosolic coupling ($\tau_{ci} << \tau_{sr}$)	Dominant SR coupling ($\tau_{sr} << \tau_{ci}$)
From the beginning of the pacing period	'-1' bifurcation	'+1' bifurcation
After the beginning of the pacing period	'-1' bifurcation	'+1' bifurcation
Does not occur during pacing period	'-1' bifurcation	No bifurcation

Table 1: Table showing which bifurcations of the synchronised state occur due to each form of dominant coupling in a network of sarcomeres. The table is split to account for the different times at which steep release from the load-release function can occur.

state with each sarcomere following the same period-doubled orbit. Since SCA is a synchronised state and stable this allows the use of the stability approach discussed in Section 2.4. This illustrates the adaptability of the stability approach, since it can be used for synchronised states that involve either a single-period and period-doubled orbit. The stability analysis revealed the forms of bifurcation that occur due to each type of dominant coupling are the same as those seen for the synchronised single-period orbit. In the case of SR dominant coupling this means that SCA undergoes a '+1' bifurcation which produced spatially varying period-doubled orbits. As with the slower pacing periods, to further study this new behaviour the next logical step is to introduce voltage dynamics and see how this affects this behaviour. Similarly, dominant cytosolic coupling causes SCA to undergo a period-doubling bifurcation leading to spatially varied period-four orbits. Furthermore, when both forms of coupling are increased spatial discordance for these period-four orbits appear.

Since these instabilities occur due to either dominant cytosolic or SR coupling, one approach to combatting them would be to try and balance the two forms of coupling. Swietach et al [119] point out that buffering in the myocyte reduces the ability for calcium to diffuse. This would suggest that promoting buffering in the part of the cell that contains dominant coupling could reduce the possibility of these instabilities. In terms of the SR, by far the most abundant buffer is CSQN. Experiments studying the effects of increased CSQN levels in ventricular myocytes have been done [120, 121] and the techniques they use could provide an

avenue to test the findings based on dominant cytosolic coupling. In the case of the cytoplasm experiments have shown that the addition of Fluo-3 can increase the presence of buffers in the cytoplasm [117], this could possibly be used to test the findings based around dominant SR coupling.

6.2 Roles Of Calcium Channels and Organelles

In our studies for a '+1' bifurcation the role of diffusion is highly influenced by other processes within the myocyte. In Section 4.5.2 we discussed how the behaviour of the SERCA pump can effect the strength of SR coupling needed for a '+1' bifurcation to occur. We related this to the different approaches in modelling the SERCA pump, modelled as a linear function whilst the original Shiferaw-Karma SERCA pump was modelled as a Hill function. To lessen the differences between these two approaches would be to model the SERCA pump as a PWL function with two switches based on the bulk cytosolic Ca^{2+} concentration. These switches would then be used to reflect the minimal and maximal values of the Hill function. On the other hand, there is a growing consensus about a role for the SR Ca^{2+} concentration in dictating the amount of Ca^{2+} pumped into the SR. Previous attempts to include the role of the SR Ca^{2+} concentration in the SERCA pump have included the modelling of a bidirectional pump [122] or modelling of a two stage reversible pump that includes a role for buffers [123]. The challenge of how to incorporate these more phenomenological approaches into a PWL model needs further research, so that the effects of a bidirectional pump upon the stability of these synchronous states can be studied directly.

Both increases and decreases of SERCA pump activity have been achieved experimentally. In terms of lowering SERCA pump activity it has been shown that the removal of PS1 and PS2 genes can achieve such an affect [124]. Similarly it has been shown that exposing myocytes briefly to thapsigargin can also inhibit SERCA pump activity [125]. On the other hand, increased SERCA pump activity has been achieved experimentally through targeted gene manipulation [126]. As such it may be possible to use a combination of these techniques to study our findings related to both significant increases and decreases in SERCA pump uptake.

As well as the role of the SERCA pump in networks, within Section 3.2.1 we illustrated that changes in either the SERCA pump uptake strength or the release slope in the load-release function could also effect the value of the critical pacing period for a period-doubling bifurcation in the uncoupled case. However, these are not the only parts of the myocyte that can have an effect with studies into the NCX [9, 12] and cytosolic buffers [9] revealing links to alternans. The PWL framework makes further studies into how parameters involved in the NCX very simple due to how well the PWL version of the NCX agrees with the original version. On the other hand, studies into the cytosolic buffers would need to be more nuanced as the PWL model treats the buffers as a constant which is a poor representation. As such improvements in the PWL modelling of the buffers would need to be found.

Whilst improving parts of the current PWL model would help to further build an understanding of how the processes within the myocyte can affect one another, it is also worth considering parts of the calcium cycle not included in the PWL model. The first of which is Ca^{2+} SR leak. As Xie *et al* [8] revealed through their iterated map method, increased SR leak could promote alternans. However, by using an iterated map method to predict how changes to parameter values could lead to a bifurcation, the parameter values at which these bifurcations occurred did not always correlate to a bifurcation within the full numerical model. Since the PWL model does not have this drawback, including leak to find these values would be a sensible move. Furthermore, since leak is usually modelled as a linear function [62], it can be incorporated directly into the PWL model without the need for any model approximations.

Another part of the calcium cycle that is usually modelled is the role of the luminal buffer CSQN. This has been done either by representing CSQN as a variable [46, 87] or by incorporating the effects of CSQN on the release from the SR [13]. Both of these approaches have revealed the luminal buffer role in the onset of alternans. Therefore it would be logical to incorporate CSQN into our PWL model to expand our understanding of its role in alternans. Again, as with the cytosolic buffers, this would present a challenge due to the non-linearity of the current modelling approaches.

One of the most overlooked parts of calcium cycle in many models, including the models used within this thesis, is mitochondria. Whilst often neglected in cardiac myocyte modelling, the importance of its role in cardiac diseases has been shown by many studies, some examples of which can be found in the following reviews [127, 128, 129, 130]. Calcium found within the bulk cytosol is both taken up by and released from mitochondria. This means mitochondrion have an active role in the cycling of calcium within myocytes. As such it is a surprise that it is often neglected in cardiac myocyte modelling studies. Two models that have included the dynamics of mitochondria are those by Gauthier *et al* [131] and Hatano *et al* [132]. Both these models use an ODE description of the mitochondrial voltage and the Dash *et al* descriptions [133] for the two main mitochondrial calcium channels, the mitochondrial sodium-calcium exchanger (NCLX) and mitochondrial Ca^{2+} uniporter (MCU). However, work by Williams *et al* [134] has since developed a model for the mitochondrial Ca^{2+} uniporter that shows potential for a PWL form. With further work involving a clamped mitochondrial voltage and alterations to the NCLX, the possibility of introducing the mitochondrial calcium dynamics into a PWL model greatly increases.

6.3 Inhomogeneous Diffusion and T-tubule Pathologies

As mentioned in Section 3.4.2 there is evidence to suggest the SR diffusion rates in the longitudinal and transversal direction are different. These differences have been incorporated into some models [135]. This raises the question of whether such differences could produce either new forms of bifurcations but, perhaps more likely, some very different spatial patterns. Whilst considering all forms of coupling together can be done in a similar way to our gap junction studies, having variations in the coupling strengths betweens sarcomeres would require multiple connectivity matrices. We would require multiple connectivity matrices since we would have more than one matrix to describe the way sarcomeres are coupled. For example, if we had different SR coupling strengths for the longitudinal and transversal directions we would need a matrix H^{long}, which would contain the longitudinal SR coupling strength, and a matrix H^{trans} containing the transversal SR coupling strength. Each of these matrices would then be partnered with a

connectivity matrix to describe which sarcomeres are coupled by the SR with these coupling strengths. As our current approach uses ideas developed by Pecora and Carroll [102] our stability approach cannot tackle this problem since these techniques rely on the presence of just one connectivity matrix. Whilst some similar techniques have been achieved with multiple connectivity matrices, these have only been for special cases, such as when the connectivity matrices commute [118]. Work has been done to progress to a more general case [136] but these techniques still rely on numerical approximations whereas we seek to study the stability via a purely analytical approach.

Should such issues be resolved this could open up other avenues of research related to variances in intracellular diffusion rates. As discussed in both Chapters 3 and 4 there is much debate as to which form of intracellular diffusion is faster. This has also led to the suggestion that one form of diffusion may be faster in some areas, whilst the other form of diffusion is faster elsewhere [105]. It would be interesting to see if this could produce new bifurcations or both a '+1' and period-doubling bifurcation simultaneously. Another possible avenue of research involves conditions such as heart disease that can cause a change in myocyte morphology. This leads to a reorganisation of the myofibrils within the myocyte altering how close sarcomeres lie to each other or their orientation [137]. Alternatively, heart disease has also been shown to cause a degradation in the SR connectivity, leading to a decrease in the amount of Ca^{2+} able to diffuse throughout the SR [138]. Both of these changes could possibly be represented by varied diffusion rates between sarcomeres within the subcellular networks considered in this thesis.

As well as changes to myocyte morphology through a reorganisation of the myofibrils, the morphology can also change due to pathological alterations to the T-tubules [139, 140]. These pathological alterations have been linked to different stages of heart failure [140] and have been shown to reshape T-tubules such that the distance between them and the ryanodine receptors increases. This can slow down the process of CICR leading to a loss of synchrony in SR release throughout the myocyte [141]. One possible avenue of research could be to use the stability approach discussed within this thesis to seek the distance between the T-tubule and ryanodine receptors at which this loss of synchrony would occur.

To do this would require a new PWL approach to modelling CICR as the current model clamps SR release to the L-Type Ca^{2+} channel. Should this be achieved, the alterations in T-tubule morphology could be studied by altering a parameter describing Ca^{2+} diffusion between the L-Type Ca^{2+} channel and ryanodine receptors.

6.4 The Role Of Gap Junctions

The focus of Chapter 5 was the effect of Ca^{2+} diffusion through gap junctions on a small network of myocytes. Within this chapter we illustrated that alternans could develop due to strong gap junction coupling, in a network of myocytes whose internal coupling was balanced. Furthermore, we revealed that the alternans with greatest amplitude lay either side of the myocyte boundary that had the largest spread of gap junctions across this boundary. In a similar way, we also found that the number of gap junctions had an affect on the coupling strength required for alternans to form, with an increase in gap junctions leading to a decrease in the coupling strength needed.

We then turned our attention to networks which contained at least some myocytes whose internal coupling had either dominant SR or cytosolic coupling. We demonstrated that an increase in the gap junction coupling strength could stabilise the behaviour related to dominant SR coupling in a network with an equal number of myocytes with each type of dominant coupling. Further to this, we demonstrated that the way these myocytes were placed within the network had an affect on the gap junctional coupling strength required to stabilise this SR dominant driven behaviour. When the number of dominant SR coupling myocytes outweighs the number of other types of myocytes, the required coupling strength of the gap junctions to stabilise SR dominant driven behaviour also increased. In Section 5.4 we saw this increased coupling strength could cause a mix of both alternans behaviour and SR dominant driven behaviour to occur within a single myocyte.

The final studies within Chapter 5 demonstrated that the gap junctional strength required to stabilise SR dominant behaviour is affected by the form of internal coupling in the neighbouring myocytes. However, the affect is small

since the gap junction coupling strength that stabilised SR dominant behaviour when the internal coupling of the neighbouring myocyte is balanced is only marginally stronger than the strength required when the internal coupling is dominant cytosolic coupling. We also saw that the myocytes that effect the required gap junctional coupling strength are only those directly coupled to the SR dominant myocytes by gap junctions, any myocytes further away within the network showed no effect.

In Chapter 5 we modelled gap junctions as a linear function with each gap junction being modelled in the same way. However, it has been suggested that intracellular Ca^{2+} concentrations may have a role in controlling the gating properties in gap junctions [142] with suggestions on how develop suitable mathematical models [143]. Moreover, gap junctions can come in a variety of forms with each form having different effects on cardiac myocyte behaviour [144]. Possible further research could seek to understand these differences whilst incorporating a modelling approach to include gating of the gap junctions.

6.5 Voltage Dynamics

Throughout this thesis we have studied a system with a clamped voltage. We have done this as we wish to understand how the calcium dynamics alone can lead to instabilities in the behaviour of the myocyte without the need for the voltage. However, within myocytes the voltage is not clamped and is affected by the movement of ions such as Ca^{2+} across the cell membrane. As such, as with any findings with clamped voltages, the findings of this thesis need to be studied further in a system with voltage dynamics. This would be particularly interesting where we have seen dominant SR coupling since the behaviour related to this has not been seen in the literature before. In a similar way, we have found the strength of coupling can have a large effect on the spatial pattern that these unwanted behaviours take. Through the introduction of voltage dynamics in a larger system we will be able to understand which of these subcellular spatial patterns may have a more significant effect on the voltage at a tissue level. For example, Skardal and Restrepo [92, 145] used a 1D cable of cells to reveal the possibility of varying instabilities across the tissue arising due to the level of

calcium driven instability within the network. However, their studies treated each cell as a single node as opposed to a subcellular network of sarcomeres and so the resulting behaviour of these instabilities had no subcellular spatial element which, as we have shown, can vary substantially from cell to cell and thus need considering. An appropriate voltage model to study the effects of our findings within this thesis would be the Fox model [59] as it is a widely accepted model due to its biological accuracy. It has also been previously coupled to the Shiferaw-Karma model [94] to study the effect of bidirectional coupling. For this reasons this would be the clear starting point to study our findings in a model with voltage dynamics.

6.6 Mathematical Techniques

The use of a piecewise linear approximation of models is prevelant, particularly in the world of neuroscience. One of the most famous piecewise linear approximations is that of the Fitzhugh-Nagumo model [146] by McKean [101]. McKean did this as it allowed him to analyse the model in much more detail since there is currently no generalised mathematical techniques for analysing non-linear models. This reasoning matches that to our thesis in which the piecewise linear approach allows us to use techniques developed by Pecora and Carroll [102] to study the stability of the system in a semi-analytical way. Since non-linear models are prevalent in cardiac modelling, should it be possible to redefine these models using a PWL caricature without losing the qualitative behaviour it would make sense to do so. Such an approach is much more possible in voltage clamped systems since the nonlinear functions used to model the voltage dynamics cannot be easily transformed into PWL functions without some loss of qualitative behaviour. The main challenges for creating PWL caricatures in models in terms of the calcium dynamics are the buffering, which we previously alluded to earlier, and the gating for SR Ca^{2+} release. In this thesis the problem of SR release gating were circumnavigated by clamping it to the L-Type channel. However, if such an approach can be avoided, then this would open the possibility for more in depth analysis of such phenomena as spontaneous Ca^{2+} release.

The techniques discussed in this thesis for studying stability can be easily

be reapplied where network models show synchronicity. In terms of biological systems this could include neuronal networks, genetic networks as well as other cardiac networks such as those involving atrial myocytes. Beyond mathematical biology, it also has possible applications in data mining, wireless communication networks and finance. This is just the tip of the iceberg and the scope of systems that show synchronicity is endless. As discussed in the review by Arenas et al [147], many of the models of these systems can be studied using approaches similar to the one used within this thesis.

A Model Variables and Parameter Values

Table 2 contains the variables used in the PWL Shiferaw-Karma model and the Shiferaw-Karma model. We have noted which variables are only found in the Shiferaw-Karma model.

Table 2: Model Variables

Variable	Definition
C_s	Subsarcolemmal Ca^{2+} Concentration
C_i	Cytosolic Ca^{2+} Concentration
C_j	Total SR Ca^{2+} Concentration
C'_j	Unrecruited JSR Ca^{2+} Concentration
I_r	Release Current From The SR Into The Cytosol
f	Voltage Dependent Inactivation Gating Variable (Shiferaw-Karma Only)
$f_{Ca^{2+}}$	Voltage Dependent Inactivation Gating Variable (Shiferaw-Karma Only)
$[CaT_s]$	Amount Of Ca^{2+} Bound To Troponin C In The Subsarcolemmal Space (Shiferaw-Karma Only)
$[CaT_i]$	Amount Of Ca^{2+} Bound To Troponin C In The Cytosol (Shiferaw-Karma Only)

Below are a list of parameter values generally used in the models described in this thesis. Some parameters are defined as Luo-Rudy II constants, for more information see the Luo-Rudy paper [60]. Where necessary the acronyms PWL (piecewise linear) and SK (Shiferaw-Karma) are placed next to the parameter names where the usual value varies between models. Values for the parameters in the Shiferaw-Karma model were obtained from the Shiferaw and Karma paper [11] and are based on experimental data. The values that were changed for the PWL model were chosen such that simulations of the PWL model reasonably replicated those of the Shiferaw-Karma model [1].

Table 3: Values for the NCX and SERCA Pump

Parameter	Definition	Value
T	Temperature	308 K
F	Faraday's Constant	96.4867 C/mmol
R	Gas Constant	8.314 J/K mol
Na_o	External Sodium Concentration	140 mM
Ca_o	External Calcium Concentration	1.8 mM
v_s/v_i	Subsarcolemmal/Cell Volume	0.1

Table 4: Values for the NCX and SERCA Pump

Parameter	Definition	Value
c_{up}	Uptake Threshold	0.5 μM
v_{up}	Uptake Strength	405 μM/s
$\bar{I}_{\text{NaCa}}$	Strength Of NCX	10^5 μM/s
k_{sat}	Luo-Rudy II Constant	0.1
ξ	Luo-Rudy II Constant	0.35
K_{mNa}	Luo-Rudy II Constant	87.5 mM
K_{mCa}	Luo-Rudy II Constant	1.38 mM
γ_{s}	Luo-Rudy II Constant	1
γ_{o}	Luo-Rudy II Constant	0.341

Table 5: Values for the L-type Ca^{2+} channel

Parameter	Definition	Value
P_{Ca}	Luo-Rudy II Constant	5.4×10^{-4} cm/s
$\bar{i}_{\text{Ca}}$ (PWL)	Flux Constant	2200 μmol/C cm
$\bar{i}_{\text{Ca}}$ (SK)	Flux Constant	11000 μmol/C cm
τ_{f}	Time Constant For Voltage Dependent Inactivation	30 ms
τ_{fCa}	Time Constant For Calcium Dependent Inactivation	20 ms
$\tilde{C}_{\text{c}}$	Calcium Inactivation Threshold	0.5 μmol
γ_{L}	Sensitivity Parameter For Calcium Dependent Inactivation	1

Table 6: Values for the SR Release

Parameter	Definition	Value
g (PWL)	Release Current Strength	3.5×10^4 sparks/μM
g (SK)	Release Current Strength	3×10^4 sparks/μM
u	Release Slope	11.3 s^{-1}
τ_{r}	Average Spark Life Time	20 ms
τ_{a}	Relaxation Time Of c'_{j} to c_{j}	50 ms
τ_{s}	Submembrane Diffusion Time Constant	10 ms

Table 9 provides the range of biologically realistic values for the cytsolic and SR coupling parameters in one and two dimensional networks. These are based off of studies by Swietach *et al* [119] and Wu and Bers [103]. Swietach suggests that the wide range of values is linked to the varying effects of buffering and tortuosity.

Table 7: Values for the Buffering

Parameter	Definition	Value
β_s	Buffering Constant For C_s	0.5
β_i	Buffering Constant For C_i	0.1
B_T	Total Concentration Of Troponin C	70 μmol/l cytosol
B_SR	Total Concentration Of SR Binding Sites	47 μmol/l cytosol
B_Cd	Total Concentration Of Calmodulin Binding Sites	24 μmol/l cytosol
K_SR	Dissociation Constant For SR Binding Sites	7 μM
K_Cd	Dissociation Constant For Calmodulin Binding Sites	0.6 μM
K_on^T	On Rate For Troponin C	32.7/μMs
$K_\mathrm{off}^\mathrm{T}$	Off Rate For Troponin C	19.6 s^{-1}

Table 8: Values for the Voltage Clamp and Internal Na Concentration

Parameter	Definition	Value
V_max	Maximal Voltage	30 mV
V_min	Minimal Voltage	-80 mV
a_x	Fitting Parameter For APD	2/3
a_N	Fitting Parameter For Internal Na Concentration	78
b_N	Fitting Parameter For Internal Na Concentration	10

Table 9: Biologically Realistic Values Cytosolic And SR Ca^{2+} Coupling

Parameter	Definition	Value
τ_c	Cytosolic Coupling Strength	2 - 250 ms
τ_sr	SR Coupling Strength	8 - 300 ms

B Voltage

Here we give details on how the voltage is modelled in both the PWL [1] and original Shiferaw-Karma model [11]. In both the PWL Shiferaw-Karma model and the original Shiferaw-Karma model the voltage is clamped such that

$$V(t) = \begin{cases} V_+(t) & kT_p \leq t < (k+x)T_p \\ V_\mathrm{min} & (k+x)T_p \leq t(k+1)T_p \end{cases}, \tag{B.1}$$

where $k \in \mathbb{N}$ and $x = a_x/(a_x + T_p)$. In the case of the original Shiferaw-Karma model V_+ has the form

$$V_+(t) = V_\mathrm{min} + (V_\mathrm{max} - V_\mathrm{min})\sqrt{1 - \left(\frac{t - kT_p}{xT_p}\right)^2}. \tag{B.2}$$

The form of V_+ for the PWL model is based on the first 6 terms of the Fourier series of the square root in Equation (B.2) for $0 \leq t \leq xT_p$. This then gives the form of V_+ for the PWL model as

$$V_+(t) = V_{\min} + (V_{\max} - V_{\min}) \sum_{j=0}^{5} a_j \cos\left(\frac{j\pi}{2xT_p} \mod (t, T_p)\right). \tag{B.3}$$

where $\mod (t, T_p) = t \mod T_p$ is the modulo operation. The coefficients a_j are

$$a_j = \frac{1}{2xT_p} \int_{-2xT_p}^{2xT_p} V_s(t) \cos\left(\frac{j\pi}{2xT_p} \mod (t, T_p)\right) \mathrm{d}t, \tag{B.4}$$

where

$$V_s = \begin{cases} -\sqrt{1 - \left(\frac{-2xT_p - \mod (t,T_p)}{xT_p}\right)^2} & -2xT_p \leq \mod (t, T_p) \leq -xT_p \\ +\sqrt{1 - \left(\frac{\mod (t,T_p)}{xT_p}\right)^2} & -xT_p \leq \mod (t, T_p) \leq xT_p \\ -\sqrt{1 - \left(\frac{2xT_p - \mod (t,T_p)}{xT_p}\right)^2} & xT_p \leq \mod (t, T_p) \leq 2xT_p \end{cases}. \tag{B.5}$$

C Piecewise Linear Shiferaw-Karma Model

Here we give details on the model equations used for some of the currents in the PWL Shiferaw-Karma model [1].

The L-type Ca^{2+} current takes the form $I_{\mathrm{CaL}} = \Theta(V - V_{\mathrm{L}}) i_{\mathrm{CaL}}$ where $V_{\mathrm{L}} = V_{\max} - 1$ and a constant conductance

$$i_{\mathrm{CaL}} = -\bar{i}_{\mathrm{Ca}} P_{\mathrm{Ca}} \frac{a_{\mathrm{CaL}} F \gamma_{\mathrm{o}} \mathrm{Ca}_{\mathrm{o}}}{\exp(2a_{\mathrm{CaL}}) - 1}, \tag{C.1}$$

where $a_{\mathrm{CaL}} = V_{\max} F / RT$.

The SERCA pump takes the form

$$I_{\mathrm{up}} = v_{\mathrm{up}} c_{\mathrm{i}}. \tag{C.2}$$

The NCX has the form $I_{\mathrm{NaCa}} = \phi(V) - \psi(V)c_{\mathrm{s}}$ where

$$\phi = \bar{I}_{\mathrm{NaCa}} \frac{\eta_q \mathrm{Na_i}^3 \mathrm{Ca_o}}{(K_{\mathrm{mNa}}^3 + \mathrm{Na_o}^3)(K_{\mathrm{mCa}} + \mathrm{Ca_o})}, \tag{C.3}$$

and

$$\psi = \bar{I}_{\mathrm{NaCa}} \frac{\gamma_{\mathrm{NaCa}} \mathrm{Na_o}^3 \times 10^{-3}}{(K_{\mathrm{mNa}}^3 + \mathrm{Na_o}^3)(K_{\mathrm{mCa}} + \mathrm{Ca_o})}. \tag{C.4}$$

The internal Na concentration is defined as

$$\mathrm{Na_i} = \frac{a_N}{1 + b_N \sqrt{T_p}}. \tag{C.5}$$

In Equation (C.3) η_q is the following quadratic

$$\eta_q = 0.0501\alpha^2 + 0.3816\alpha + 0.9182, \tag{C.6}$$

where $\alpha = FV/RT$. In equation (C.4) γ_{NaCa} is a piecewise constant function such that

$$\gamma_{\mathrm{NaCa}} = \begin{cases} 0.45 & V > V_{\mathrm{NaCa}} \\ 4 & V \leq V_{\mathrm{NaCa}} \end{cases}, \tag{C.7}$$

where $V_{\mathrm{NaCa}} = -50$. Ca_o represent the extracellular Ca^{2+} concentration and is used to make sure calcium is conserved within the myocyte. The load-release function Q is as given in Section 2.3 and the buffers are the constants given in Table 7 in Appendix A.

D Shiferaw-Karma Model

Here we give the model and equations used within the original Shiferaw-Karma model [11]. The Shiferaw-Karma model comes with 4 further variables (per sarcomere in the case of a network) compared to the PWL version. These are the voltage dependent inactivation gating variable (f), the calcium-induced inactivation gating variable (f_{Ca}) along with the amount of Ca^{2+} bound to Troponin C in the subsarcolemmal space ($[\mathrm{CaT}]_{\mathrm{s}}$) and the bulk cytosol ($[\mathrm{CaT}]_{\mathrm{i}}$). This means

the ODE's for a sarcomere in a coupled network are now

$$
\begin{aligned}
\frac{\mathrm{d}c_{\mathrm{s}}^{\mu}}{\mathrm{d}t} &= \beta(c_{\mathrm{s}}^{\mu})\left[\frac{v_{\mathrm{i}}}{v_{\mathrm{s}}}\left(I_{\mathrm{r}}^{\mu}-\frac{c_{\mathrm{s}}^{\mu}-c_{\mathrm{i}}^{\mu}}{\tau_{\mathrm{s}}}-I_{\mathrm{CaL}}\right)+I_{\mathrm{NaCa}}^{\mu}-I_{\mathrm{trpn^s}}^{\mu}\right],\\
\frac{\mathrm{d}c_{\mathrm{i}}^{\mu}}{\mathrm{d}t} &= \beta(c_{\mathrm{i}}^{\mu})\left[\frac{c_{\mathrm{s}}^{\mu}-c_{\mathrm{i}}^{\mu}}{\tau_{\mathrm{s}}}-I_{\mathrm{up}}^{\mu}-I_{\mathrm{trpn^i}}^{\mu}+\sum_{\zeta\in cc}(\mathrm{c_i}^{\zeta}-\mathrm{c_i}^{\mu})/\tau_{\mathrm{c}}\right],\\
\frac{\mathrm{d}c_{\mathrm{j}}^{\mu}}{\mathrm{d}t} &= -I_{\mathrm{r}}^{\mu}+I_{\mathrm{up}}^{\mu}+\sum_{\zeta\in cc}(\mathrm{c_j}^{\zeta}-\mathrm{c_j}^{\mu})/\tau_{\mathrm{sr}},\\
\frac{\mathrm{d}c_{\mathrm{j}}'^{\mu}}{\mathrm{d}t} &= \frac{c_{\mathrm{j}}^{\mu}-c_{\mathrm{j}}'^{\mu}}{\tau_{\mathrm{a}}},\\
\frac{\mathrm{d}I_{\mathrm{r}}^{\mu}}{\mathrm{d}t} &= -gI_{\mathrm{CaL}}Q\left(c_{\mathrm{j}}'^{\mu}\right)-\frac{I_{\mathrm{r}}^{\mu}}{\tau_{\mathrm{r}}},\\
\frac{\mathrm{d}f^{\mu}}{\mathrm{d}t} &= \frac{f_{\infty}-f^{\mu}}{\tau_{\mathrm{f}}},\\
\frac{\mathrm{d}f_{\mathrm{Ca}}^{\mu}}{\mathrm{d}t} &= \frac{f_{\mathrm{Ca},\infty}-f\mathrm{Ca}^{\mu}}{\tau_{\mathrm{fCa}}},\\
\frac{\mathrm{d}[\mathrm{CaT}]_{\mathrm{s}}^{\mu}}{\mathrm{d}t} &= I_{\mathrm{trpn^s}}^{\mu},\\
\frac{\mathrm{d}[\mathrm{CaT}]_{\mathrm{i}}^{\mu}}{\mathrm{d}t} &= I_{\mathrm{trpn^i}}^{\mu}.
\end{aligned}
\tag{D.1}
$$

In Equation D.1 μ the currents I_{CaL}, I_{NaCa} and I_{up} still represent the same currents as in Section 2.3 and the coupling terms are still for nearest neighbour coupling. The two versions of I_{trpn} represent the change in the amount of Ca^{2+} bound to Troponin C and either the subsarcolemmal space or the bulk cytosol. The buffering β is now a function of the Ca^{2+} concentration in either the subsarcolemmal space or bulk cytosol.

The L-type Ca^{2+} current takes the form $I_{\mathrm{CaL}} = d_{\infty}ff_{\mathrm{Ca}}i_{\mathrm{CaL}}$ where

$$
i_{\mathrm{CaL}} = 4\alpha F\bar{i}_{\mathrm{Ca}}P_{\mathrm{Ca}}\frac{c_{\mathrm{s}}exp(2\alpha)-\gamma_{\mathrm{o}}\mathrm{Ca_o}}{\exp(2\alpha)-1}. \tag{D.2}
$$

where α has the same form as seen in Appendix C. The steady-state equations for voltage dependent activation (d_{∞}), voltage dependent inactivation (f_{∞}) and

calcium-induced inactivation ($f_{\mathrm{Ca},\infty}$) are

$$\begin{aligned} d_\infty &= \frac{1}{1+exp[-(V-5)/6.24]}, \\ f_\infty &= \frac{1}{1+exp[(V=35)/8.6]}, \\ f_{\mathrm{Ca},\infty} &= \frac{1}{1+\left(c_\mathrm{s}/\tilde{C}_\mathrm{c}\right)^{\gamma_\mathrm{L}}}. \end{aligned} \tag{D.3}$$

The SERCA pump takes the form

$$I_\mathrm{up} = \frac{v_\mathrm{up} c_\mathrm{i}^2}{c_\mathrm{up}^2 + c_\mathrm{i}^2}. \tag{D.4}$$

This representation is used to capture the maximal and minimal flow of Ca^{2+} through the SERCA pump due to the bulk cytosolic Ca^{2+} concentration. The parameter c_up is the uptake threshold at which the gradient of the function representing the SERCA pump begins to decrease as it approaches the maximal value. This is deemed more biologically realistic than the linear representation used in the PWL Shiferaw-Karma model.

The NCX has the form

$$I_\mathrm{NaCa} = \bar{I}_\mathrm{NaCa} \frac{\eta \mathrm{Na_i}^3 \mathrm{Ca_o} - \eta e^{-\alpha} \mathrm{Na_o}^3 c_\mathrm{s} \times 10^{-3}}{(K_\mathrm{mNa}^3 + \mathrm{Na_o}^3)(K_\mathrm{mCa} + \mathrm{Ca_o})}, \tag{D.5}$$

where η has the following form

$$\eta = \frac{e^{\xi\alpha}}{1 + k_\mathrm{sat} e^{(\xi-1)\alpha}}. \tag{D.6}$$

The equations for α and $\mathrm{Na_i}$ are the same as those in Appendix C.

The equations for the buffers are defined using the rapid buffering approximation [115] and thus have the general functional form

$$\beta(c) = \frac{1}{1 + \dfrac{B_\mathrm{SR} K_\mathrm{SR}}{(c+K_\mathrm{SR})^2} + \dfrac{B_\mathrm{Cd} K_\mathrm{Cd}}{(c+K_\mathrm{Cd})^2}}. \tag{D.7}$$

Whilst the general functional form for the change in the amount of Ca^{2+} is defined

as

$$I_{\text{trpn}} = K_{\text{on}}^{\text{T}} c(B_{\text{T}} - [\text{CaT}]) - K_{\text{off}}^{\text{T}}[\text{CaT}]. \tag{D.8}$$

The load-release function Q is as given in Section 2.3.

References

[1] R. Thul and S. Coombes. Understanding cardiac alternans: A piecewise linear modelling framework. *Chaos*, 20:045102, 2010.

[2] M.E. Diaz, S.C. O'Niell, and D.A. Eisner. Sarcoplasmic reticulum calcium content fluctuation is the key to cardiac alternans. *Circulation Research*, 94:650–656, 2004.

[3] M.L. Kollar, M.L. Riccio, and R.F. Gilmour JR. Effect of $[K^+]_o$ on electrical restitution and activation dynamics during ventricular fibrillation. *American Journal of Physiology - Heart and Circulatory Physiology*, 279:H2665H2672, 2000.

[4] D.M. Bers. Cardiac excitation-contraction coupling. *Nature*, 415:198–205, 2002.

[5] J.M. Nerbonne and R.S. Kass. Molecular physiology of cardiac repolarization. *Physiological Reviews*, 85(4):1205–1253, 2005.

[6] D.S. Rosenbaum, L.E. Jackson, J.M. Smith, H. Garan, J.N. Ruskin, and R.J. Cohen. Electrical alternans and vulnerability to ventricular arrythmias. *The New England Journal of Medicine*, 330:235–241, 1994.

[7] M. Rubart and D.P. Zipes. Mechanisms of sudden cardiac death. *Journal of Clinical Investigation*, 115:23052315, 2005.

[8] L. Xie, D. Sato, A. Garfinkel, Z. Qu, and J.N Weiss. Intracellular Ca^{2+} alternans: Coordinated regulation by sarcoplasmic reticulum release, uptake and leak. *Biophysical Journal*, 95:3100–3110, 2008.

[9] M. Nivala and Z. Qu. Calcium alternans in a couplon network model of ventricular myocytes: Role of sarcoplasmic reticulum load. *American Journal of Physiology - Heart and Circulatory Physiology*, 303:H341–H352, 2012.

[10] Z. Qu, M.B. Liu, and M. Nivala. A unified theory of calcium alternans in ventricular myocytes. *Scientific Reports*, 6:35625, 2016.

[11] Y. Shiferaw, M.A. Watanabe, A. Garfinkel, J.N. Wiess, and A. Karma. Model of intracellular calcium cycling in ventricular myocyctes. *Biophysical Journal*, 85:3666–3686, 2003.

[12] M.A. Huertas, G.D. Smith, and S. Györke. Ca^{2+} alternans in a cardiac myocyte model that uses moment equations to represent heterogeneous junctional sr Ca^{2+}. *Biophysical Journal*, 99:377–387, 2010.

[13] J.G. Restrepo, J.N. Weiss, and A. Karma. Calsequestrin-mediated mechanism for cellular calcium transient alternans. *Biophysical Journal*, 95:3767–3789, 2008.

[14] O. Tian, L. Kaestner, and P. Lipp. Noise-free visualization of microscopic calcium signalling by pixel-wise fitting. *Circulation Research*, 111:17–27, 2012.

[15] G.L. Aistrup, Y. Shiferaw, S. Kapur, A.H. Kadish, and J.A. Wasserstrom. Mechanisms underlying the formation and dynamics of subcellular calcium alternans in the intact rat heart. *Circulation Research*, 104:639–649, 2009.

[16] T. Höfer, A. Politi, and R. Heinrich. Intercellular Ca^{2+} wave propagation through gap-junctional Ca^{2+} diffusion: A theoretical study. *Biophysical Journal*, 80:75–87, 2001.

[17] C. Lamont, P.W. Luther, C.W. Balke, and W.G. Wier. Intercellular Ca^{2+} waves in rat heart muscle. *Journal of Physiology*, 512(Pt 3):669–676, 1998.

[18] Z. Jia, H. Bien, Y. Shiferaw, and E. Entcheva. Cardiac cellular coupling and the spread of early instabilities in intracellular Ca^{2+}. *Biophysical Journal*, 102:1294–1302, 2012.

[19] N. Kurebayashi, H. Yamashita, Y. Nakazato, H. Daida, and Y. Ogawa. Behaviour of Ca^{2+} waves in multicellular preparations from guniea pig ventricle. *American Journal of Physiology - Cell Physiology*, 287:C1646–C1656, 2004.

[20] G.A. Langer. Ion fluxes in cardiac excitation and contraction and their relation to myocardial contractility. *Physiological Reviews*, 48:708–757, 1968.

[21] H.A. Fozzard. Heart: Excitation-contraction coupling. *Annual Review of Physiology*, 39:201–220, 1977.

[22] S. Perni, V.R. Iyer, and C. Franzini-Armstrong. Ultrastructure of cardiac muscle in reptiles and birds: optimizing and/or rudicing the probability of transimisson between calcium release units. *Journal of Muscle Research and Cell Motility*, 33:145–152, 2012.

[23] S. Seki, M. Nagashima, Y. Yamada, M. Tsutsuura, T. Kobayashi, A. Namiki, and N. Tohse. Fetal and postnatyal development of Ca^{2+} transients and Ca^{2+} sparks in rat cardiomyocytes. *Cardiovascular Research*, 58:535–548, 2003.

[24] M.M. Kirk, L.T. Izu, Y. Chen-Izu, S.L. McCulle, W.G. Wier, C.W. Balke, and S.R. Shorofsky. Role of thte transverse-axial tubule system in generating calcium sparks and calcium transients in rat atrial myocytes. *Journal of Physiology*, 547(Pt 2):441–451, 2003.

[25] M.A. Richards, J.D. Clarke, P. Saravanan, N. Voigt, D. Dobrev, D.A. Eisner, A.W. Trafford, and K.M. Dibb. Transverse tubules are a common feature in large mammalian atrial myocytes including human. *American Journal of Physiology - Heart and Circulatory Physiology*, 301:H1996–H2005, 2011.

[26] A.M. Katz. *Physiology Of The Heart*. Lippincott Williams & Wilkins, 4^{th} ed. edition, 2006.

[27] D.W. Fawcett and N.S. McNutt. The ultrastructure of the cat myocardium. *The Journal Of Cell Biology*, 42:1–45, 1969.

[28] A.S. Ayettey and V. Navaratnam. The t-tubule system in the specialized and general myocardium of the rat. *Journal Of Anatomy*, 127(Pt 1):125–140, 1978.

[29] I.D. Jayasinghe, M.B. Cannell, and C. Soeller. Organization of ryanodine receptors, transverse tubules, and sodium-calcium exchanger in rat myocytes. *Biophysical Journal*, 97:2664–2673, 2009.

[30] G.A. Dabiri, K.K. Turnacioglu, J.M. Sanger, and J.W. Sanger. Myofibrillogenesis visualized in living embryonic cardiomyocytes. *PNAS*, 94:9493–9498, 1997.

[31] N.J. Severs, S.R. Coppen, E. Dupont, H. Yeh, Y. Ko, and T. Matsushita. Gap junction alterations in human cardiac disease. *Cardiovascular Research*, 62:368–377, 2004.

[32] H.L. Kanter, J.G. Laing, E.C. Beyer, K.G. Green, and J.E. Saffitz. Multiple connexins colocalize in cannine ventricular myocyte gap junctions. *Circulation Research*, 73:344–350, 1993.

[33] M.J.A. Van Kampen, J.L.M. Vermeulen, A.F.M. Moorman, D. Gros, D.L. Paul, and W.H. Lamers. Developmental changes of connexin40 and connexin43 mrna distribution patterns in the rat heart. *Cardiovascular Research*, 32:886–900, 1996.

[34] R. Bruzzone, T.W., and D.L. Paul. Connections with connexins: the molecular basis of direct intercellular signaling. *the FEBS Journal*, 238:1–27, 1996.

[35] T. Lewis. Notes upon alternation in the heart. *Quaterly Journal Of Medicine*, 4:141–144, 1911.

[36] H.C. Lee, R. Mohabir, N. Smith, M.R. Franz, and W.T. Clusin. Effect of ischemia on calcium-dependent fluorescence transients in rabbit hearts containing indo 1: Correlation with monophasic action potentials and contraction. *Circulation*, 78:1047–1059, 1988.

[37] M.J. Lab and J.A. Lee. Changes in intracellular calcium during mechanical alternans in isolated ferret ventricular muscle. *Circulation Research*, 66:585–595, 1990.

[38] Y. Kihara and J. P. Morgan. Abnormal Ca_i^{2+} handling is the primary cause of mechanical alternans: study in ferret ventricular muscles. *American Journal of Physiology - Heart and Circulatory Physiology*, 261:H1746–H1755, 1991.

[39] J.B. Nolasco and R.W. Dahlen. A graphic method for the study of alternation in cardiac action potentials. *Journal Of Applied Physiology*, 25:191–196, 1968.

[40] M. Chinushi, D. Kozhevnikov, E.B. Caref, M. Restivo, and N. El-Sherif. Mechanism of discordant t wave alternans in the in vivo heart. *Biophysical Journal*, 14:632–638, 2003.

[41] E. Chudin, J. Goldhaber, A. Garfinkel, J. Weiss, and B. Kogan. Intracellular Ca^{2+} dynamics and the stability of ventricular tachycardia. *Biophysical Jorunal*, 77:2930–2941, 1999.

[42] J. Hüser, Y.G. Wang, K.A. Sheehan, F. Cifuentes, S.L. Lipsius, and L.A. Blatter. Functional coupling between glycolysis and excitationcontraction coupling underlies alternans in cat heart cells. *Journal of Physiology*, 524(Pt 3):795–806, 2000.

[43] J.I. Goldhaber, L-H. Xie, T. Duong, C. Motter, K. Khuu, and J.N. Weiss. Action potential duration restitution and alternans in rabbit ventricular myocytes: The key role of intracellular calcium cycling. *Circulation Research*, 96:459–466, 2005.

[44] E.J. Pruvot, R.P. Katra, D.S. Rosenbaum, and K.R. Laurita. Role of calcium cycling versus restitution in the mechanism of repolarization alternans. *Circulation Research*, 94:1083–1090, 2004.

[45] M.R. Franz. The electrical restitution curve revisited: Steep or flat slopewhich is better? *Journal of Cardiovascular Electrophysiology*, 14:S140S147, 2003.

[46] T.R.Shannon, F. Wang, J. Puglisi, C. Weber, and D.M. Bers. A mathematical treatment of integrated ca dynamics within the ventriuclar myocyte. *Biophysical Journal*, 87:3351–3371, 2004.

[47] J.M. Pastore, S.G. Girouard, K.R. Laurita, F.G. Akar, and D.S. Rosenbaum. Mechanism linking t-wave alternans to the genesis of cardiac fibrillation. *Circulation*, 99:1385–1394, 1999.

[48] W. Shimizu and C. Antzelevitch. Cellular and ionic basis for T-wave alternans under long-QT conditions. *Circulation*, 99:1499–1507, 1999.

[49] Y-W. Qian, W.T. Clusin, S-H. Lin, J. Han, and R.J. Sung. Spatial heterogeneity of calcium transient alternans during the early phase of myocardial ischemia in the blood-perfused rabbit heart. *Circulation*, 104:2082–2087, 2001.

[50] A.L. Hodgkin and H.F. Huxley. The components of membrane conductance in the giant axon of loligo. *Journal of Physiology*, 116:473–496, 1952.

[51] R.E. McAllister, D. Noble, and R.W. Tsien. Reconstruction of the electrical activity of cardiac purkinje fibres. *Journal of Physiology*, 251:1–59, 1975.

[52] G.W. Beeler and H. Reuters. Reconstruction of the action potential of ventricular myocytes. *Journal of Physiology*, 268:177–210, 1977.

[53] B.F. Hoffman ans E.E. Suckling. Effect of heart rate on cardiac membrane potentials and the unipolar electrogram. *American Journal of Physiology*, 179:123–130, 1954.

[54] D. Noble. A modification of the hodgin-huxley equations applicable to purkinje fibre action and pacemaker potentials. *Journal of Physiology*, 160:317–352, 1962.

[55] D.S. Riggs. *The Mathematical Approach to Physiological Problems*. Lippincott Williams & Wilkins, 1st ed. edition, 1964.

[56] M.R. Guevara, G. Ward, A. Shrier, and L. Glass. Electrical alternans and period-doubling bifurcations. *Computers in Cardiology*, pages 167–170, 1984.

[57] C.M. Berger, X. Zhao, D.G. Schaeffer, H.M. Dobrovolny, W. Krassowska, and D.J. Gauthier. Period-doubling bifurcations to alternans in paced cardiac tissue: Crossover from smooth to border-collision characteristics. *Physical Review Letters*, 99:058101, 2007.

[58] Z. Qu, A. Garfinkel, P. Chen, and J.N. Weiss. Mechanisms of discordant alternans and induction of reentry in simulated cardiac tissue. *Circulation*, 102:1664–1670, 2000.

[59] J.J. Fox, J.L. McHarg, and R.F. Gilmour JR. Ionic mechanism of elecrtical alternans. *American Journal of Physiology - Heart and Circulatory Physiology*, 282:H516–H530, 2001.

[60] C. Luo and Y. Rudy. A dynamic model of the cardiac ventricular action potential. *Circulation Research*, 74:1071–1096, 1994.

[61] R.L. Winslow, J. Rice, S. Jafri, E. Marbán, and B. O'Rourke. Mechanisms of altered excitation-contraction coupling in canine tachycardia-induced heart failure ii: Model studies. *Circulation Research*, 84:571–586, 1999.

[62] A. Mahajan, Y. Shiferaw, D. Sato, A. Baher, R. Olcese, L. Xie, M. Yang, P. Chen, J.G. Restrepo, A. Karma, A. Garfinkel, Z. Qu, and J.N. Weiss. A rabbit ventricular action potential model replicating cardiac dynamics at rapid heart rates. *Biophysical Journal*, 94:392–410, 2008.

[63] A.V. Zaitsev, P.K. Guha, F. Sarmast, A. Kolli, O. Berenfeld, A.M. Pertsov, J.R. de Groot, R. Coronel, and J. Jalife. Wavebreak formation during ventricular fibrillation in the isolated, regionally ischemic pig heart. *Circulation Research*, 92:546–553, 2003.

[64] L.M. Livshitz and Y. Rudy. Regulation of Ca^{2+} and electrical alternans in cardiac myocytes: Role of camkii and repolarizing currents. *American Journal of Physiology - Heart and Circulatory Physiology*, 292:H2854–H2866, 2007.

[65] M.S. Jafri, J.J. Rice, and R.L. Winslow. Cardiac Ca^{2+} dynamics: The roles of ryanodine receptor adaptation and sarcoplasmic reticulum load. *Biophysical Journal*, 74:1149–1168, 1998.

[66] M.D. Stern. Theory of excitation-contraction coupling in cardiac muscle. *Biophysical Journal*, 63:497–517, 1992.

[67] M.D. Stern. The model of snyder et al. does not simulate graded Ca^{2+} release from the cardiac sarcoplasmic reticulum in intact cells. *Biophysical Journal*, 79:33533354, 2000.

[68] G.S.B. Williams, G.D. Smith, E.A. Sobie, and M.S. Jafri. Models of cardiac excitation-contraction coupling in ventricular myocytes. *Mathematical Biosciences*, 226:1–15, 2010.

[69] M. Fink, S.A. Niederer, E.M. Cherry, F.H. Fenton, J.T. Koivumäki, G. Seemann, R. Thul, H. Zhang, F.B. Sachse, D. Beard, E.J. Crampin, and N.P. Smith. Cardiac cell modelling: Observations from the heart of the cardiac physiome project. *Progress in Biophysics and Molecular Biology*, 104:2–21, 2011.

[70] J.L. Greenstein and R.L. Winslow. Integrative system models of cardiac excitation contraction coupling. *Circulatory Research*, 108:70–84, 2011.

[71] M.S. Jafri. Models of excitation-contraction coupling in cardiac ventricular myocytes. In R. Larson, editor, *Bioinformatics and Drug Discovery*, chapter 14, pages 309–335. Humana Press, Totowa NJ, 2014.

[72] M. Kameyama, Y. Hirayama, H. Saitoh, M. Maruyama, H. Atarashi, and T. Takano. Possible contribution of the sarcoplasmic reticulum Ca^{2+} pump function to electrical and mechanical alternans. *Journal of Electrocardiology*, 36:125–135, 2003.

[73] S. C. O'Neill, L. Miller, R. Hinch, and D. A. Eisner. Interplay between serca and sarcolemmal Ca^{2+} efflux pathways controls spontaneous release of Ca^{2+} from the sarcoplasmic reticulum in rat ventricular myocytes. *Journal of Physiology*, 559:121–128, 2004.

[74] Y. Shiferaw. Nonlinear onset of calcium wave propagation in cardiac cells. *Physical Review E*, 94:032405, 2016.

[75] D.A. Eisner, H.S. Choi, M.E. Daz, S.C. ONeill, and A.W. Trafford. Integrative analysis of calcium cycling in cardiac muscle. *Circulation Research*, 87:1087–1094, 2000.

[76] Y. Li, M.E. Diaz, D.A. Eisner, and S. O'Neill. The effects of membrane potential, sr Ca^{2+} content and ryr responsiveness on systolic Ca^{2+} alternans in rat ventricular myocytes. *Journal of Physiology*, 587:12831292, 2009.

[77] J.N. Weiss, A. Karma, Y. Shiferaw, P. Chen, A. Garfinkel, and Z. Qu. From pulsus to pulseless: The saga of cardiac alternans. *Circulation Research*, 98:1244–1253, 2006.

[78] Z. Qu, Y. Shiferaw, and J.N. Weiss. Nonlinear dynamics of cardiac excitation-contraction coupling: An iterated map study. *Physical Reveiw E*, 75:011927, 2007.

[79] E. Picht, J. DeSantiago, and L.A. Blatter D.M. Bers. Cardiac alternans do not rely on diastolic sarcoplasmic reticulum calcium content fluctuations. *Circulation Research*, 99:740–748, 2006.

[80] A. Peñaranda, E. Alvarez-Lacalle, I.R. Cantalapiedra, and B. Echebarria. Nonlinearities due to refractoriness in sr ca release. *Computing in Cardiology*, 39:297–300, 2012.

[81] M.D. Stern, L. Song, H. Cheng, J.S.K. Sham, H.T. Yang, K.R. Boheler, and E. Ros. Local control models of cardiac excitationcontraction coupling: A possible role for allosteric interactions between ryanodine receptors. *The Journal of General Physiology*, 113(3):469–489, 1999.

[82] E. Alvarez-Lacalle, I.R. Cantalapiedra, A. Peñaranda, J. Cinca, L. Hove-Madsen, and B. Echebarria. Dependency of calcium alternans on ryanodine receptor refractoriness. *PLoS One*, 8:e55042, 2013.

[83] I.R. Cantalapiedra, E. Alvarez-Lacalle, A. Peñaranda, and B. Echebarria. Minimal model for calcium alternans due to sr release refractoriness. *Chaos*, 27:093904, 2017.

[84] T. Tao, S.C. O'Neill, M.E. Diaz, Y.T. Li, D.A. Eisner, and H. Zhang. Alternans of cardiac cycling in a cluster of ryanodine receptors: A simulation study. *American Journal of Physiology - Heart and Circulatory Physiology*, 295:H598–H609, 2008.

[85] X. Wan, K.R. Laurita, E.J. Pruvot, and D.S. Rosenbaum. Molecular correlates of repolarization alternans in cardiac myocytes. *Journal of Molecular and Cellular Cardiology*, 39:419–428, 2005.

[86] K. Schlotthauer and D.M. Bers. Sarcoplasmic reticulum Ca^{2+} release causes myocyte depolarization: Underlying mechanism and threshold for triggered action potentials. *Circulation Research*, 87:774–780, 2000.

[87] E. Alvarez-Lacalle, A. Peñaranda, and I.R. Cantalapiedra. Effects of ryr2 refractoriness and hypercalcemia on calcium overload, spontaneous release, and calcium alternans. *Computing In Cardiology*, 40:683–686, 2013.

[88] E. Alvarez-Lacalle, B. Echebarria, J. Spalding, and Y. Shiferaw. Calcium alternans is due to an order-disorder phase transition in cardiac cells. *Physical Review Letters*, 1144:108101, 2015.

[89] X. Cui, R.J. Rovetti, L. Yang, A. Garfinkel, J.N. Weiss, and Z. Qu. Period-doubling bifurcation in an array of coupled stochastically excitable elements subjected to global periodic forcing. *Physical Review Letters*, 103:044102, 2009.

[90] R. Rovetti, X. Cui, A. Garfinkel, J.N. Weiss, and Z. Qu. Spark-induced sparks as a mechanism of intracellular calcium alternans in cardiac myocytes. *Circulation Research*, 106:1582–1591, 2010.

[91] H. Bien, L. Yin, and E. Entcheva. Calcium instabilities in mammalian cardiomyocyte networks. *Biophysical Journal*, 90:2628–2640, 2006.

[92] P.S. Skardal and J.G. Restrepo. Coexisting chaotic and multi-periodic dynamics in a model of cardiac alternans. *Chaos*, 24:043126, 2014.

[93] Y. Shiferaw, D. Sato, and A. Karma. Coupled dynamics of voltage and calcium in paced cardiac cells. *Physical Review E*, 71:021903, 2005.

[94] Y. Shiferaw and A. Karma. Turing instability mediated by voltage and calcium diffusion in paced cardiac cells. *PNAS*, 103:56705675, 2006.

[95] J.G. Restrepo and A. Karma. Spatiotemporal intracellular calcium dynamics during cardiac alternans. *Chaos*, 19:037115, 2009.

[96] S.A. Gaeta, T. Krogh-Madsen, and D.J. Christini. Feedback-control induced pattern formation in cardiac myocytes: a mathematical modeling study. *Journal of Theoretical Biology*, 266:408–418, 2010.

[97] M. Li and N.F. Otani. Ion channel basis for alternans and memory in cardiac myocytes. *Annals of Biomedical Engineering*, 31:1213–1230, 2003.

[98] W. Groenendaal, F.A. Ortega, T. Krogh-Madsen, and D.J. Christini. Voltage and calcium dynamics both underlie cellular alternans in cardiac myocytes. *Biophysical Journal*, 106:2222–2232, 2014.

[99] E.M. Cherry. Distinguishing mechanisms for alternans in cardiac cells using constant-diastolic-interval pacing. *Chaos*, 27:093902, 2017.

[100] Z. Song, C.Y. Ko, M. Nivala. J.N. Weiss, and Z. Qu. Calcium-voltage coupling in the genesis of early and delayed afterdepolarizations in cardiac myocytes. *Biophysical Journal*, 106:1908–1921, 2015.

[101] H.P. McKean Jr. Nagumo's equation. *Advances in Mathematics*, 4:209–223, 1970.

[102] L.M. Pecora and T.L. Carroll. Master stability functions for synchronized coupled systems. *Phys. Rev. Lett.*, 80:2109–2112, 1998.

[103] X. Wu and D.M. Bers. Sarcoplasmic reticulum and nuclear envelope are one highly interconnected Ca^{2+} store throughout cardiac myocyte. *Circulation Research*, 99:283–291, 2006.

[104] P. Swietach, K.W. Spitzer, and R.D. Vaughan-Jones. Ca^{2+}-mobility in the sarcoplasmic reticulum of ventricular myocytes is low. *Biophysical Journal*, 95:1412–1427, 2008.

[105] D.M. Bers and T.R. Shannon. Calcium movements inside the sarcoplasmic reticulum of cardiac myocytes. *Journal of Molecular and Cellular Cardiology*, 58:59–66, 2013.

[106] S.A. Gaeta and D.J. Christini. Non-linear dynamics of cardiac alternans: subcellular to tissue-level mechanisms of arrythmia. *Frontiers in Physiology*, 3:157.1–157.13, 2012.

[107] R. Majumder, M.C. Engels, A.A.F. de Vries, A.V. Panfilov, and D.A. Pijnappels. Islands of spatially discordant apd alternans underlie arrhythmogenesis by promoting electrotonic dyssynchrony in models of fibrotic rat ventricular myocardium. *Scientific Reports*, 6:24334, 2016.

[108] E. Picht, A.V. Zima, T.R. Shannon, A.M. Duncan, L.A. Blatter, and D.M. Bers. Dynamic calcium movement inside cardiac sarcoplasmic reticulum during release. *Circulation Research*, 108:847–856, 2011.

[109] E.G. Lakatta. Functional implications of spontaneous sarcoplasmic reticulum Ca^{2+} release in the heart. *Cardiovascular Research*, 26:193–214, 1992.

[110] E.G. Lakatta. Measurement of sarcoplasmic reticulum Ca^{2+} content and sarcolemmal Ca^{2+} fluxes in isolated rat ventricular myocytes during spontaneous Ca^{2+} release. *Journal of Physiology*, 501:3–16, 1997.

[111] S.G. Priori and S.R. Wayne Chen. Inherited dysfunction of sarcoplasmic reticulum Ca^{2+} handling and arrhythmogenesis. *Circulation Research*, 108:871–883, 2011.

[112] G.L. Aistrup, J.E. Kelly, S. Kapur, M. Kowalczyk, I. Sysman-Wolpin, A.H. Kadish, and J.A. Wasserstrom. Pacing-induced heterogeneities in intracellular Ca^{2+} signaling, cardiac alternans, and ventricular arrhythmias in intact rat heart. *Circulation Research*, 99:E65–E73, 2006.

[113] Z. Song, M.B. Liu, and Z. Qu. Transverse tubular network structures in the genesis of intracellular calcium alternans and triggered activity in cardiac cells. *Journal of Molecular and Cellular Cardiology*, 114:288–299, 2018.

[114] L-H. Xie and J.N. Weiss. Arrhythmogenic consequences of intracellular calcium waves. *American Journal of Physiology - Heart and Circulatory Physiology*, 297:H997–H1002, 2009.

[115] J. Wagner and J. Keizer. Effects of rapid buffers on Ca^{2+} diffusion and Ca^{2+} oscillations. *Biophysical Journal*, 67:447–456, 1994.

[116] A. Fabiato. Calcium-induced release of calcium from the cardiac sarcoplasmic reticulum. *American Journal of Physiology - Cell Physiology*, 245:C1–C14, 1983.

[117] A. Michailova, D. DelPrincipe, M. Egger, and E. Niggli. Spatiotemporal features of Ca^{2+} buffering and diffusion in atrial cardiac myocytes with inhibited sarcoplasmic reticulum. *Biophysical Journal*, 83:31343151, 2002.

[118] F. Sorrentino. Synchronization of hypernetworks of coupled dynamical systems. *New Journal of Physics*, 14:033035, 2012.

[119] P. Swietach, K.W. Spitzer, and R.D. Vaughan-Jones. Modeling calcium waves in cardiac myocytes: importance of calcium diffusion. *Frontiers in Bioscience*, 15:661–680, 2010.

[120] D. Terentyev, S. Viatchenko, I. Györke, P. Volpe, S.C. Williams, and S. Györke. Calsequestrin determines the functional size and stability of cardiac intracellular calcium stores: Mechanism for hereditary arrhythmia. *PNAS*, 100:1175911764, 2003.

[121] A. Guo, S.E. Cala, and L-S. Song. Calsequestrin accumulation in rough endoplasmic reticulum promotes perinuclear Ca^{2+} release. *The Journal Of Biological Chemistry*, 287:1667016680, 2012.

[122] T.R. Shannon, K.S. Ginsburg, and D.M. Bers. Reverse mode of the sarcoplasmic reticulum calcium pump and load-dependent cytosolic calcium decline in voltage-clamped cardiac ventricular myocytes. *Biophysical Journal*, 78:322–333, 2000.

[123] J.T. Koivumäki, J. Takalo, T. Korhonen, P. Tavi, and M. Weckström. Modelling sarcoplasmic reticulum calcium atpase and its regulation in cardiac myocytes. *Philosophical Transactions of The Royal Society A*, 367:21812202, 2009.

[124] K.N. Green, A. Demuro, Y. Akbari, B.D. Hitt, I.F. Smith, I. Parker, and F.M LaFerla. Serca pump activity is physiologically regulated by presenilin and regulates amyloid β production. *Journal of Cell Biology*, 181:1107–1116, 2008.

[125] L. Gómez-Viquez, G. Guerroro-Serna, U. García, and A. Guerrero-Hernández. Serca pump optimizes Ca^{2+} release by a mechanism independent of store filling in smooth muscle cells. *Biophysical Journal*, 85:370380, 2003.

[126] R. Vetter, U. Rehfeld, C. Reissfelder, W. Weiss, K-D. Wagner, J. Günther, A. Hammes, C. Tschöpe, W. Dillmann, and M. Paul. Transgenic overexpression of the sarcoplasmic reticulum Ca^{2+}atpase improves reticular Ca^{2+} handling in normal and diabetic rat hearts. *The FASEB Journal*, 16:16571659, 2002.

[127] G.S.B. Williams, L. Boyman, and W.J. Lederer. Mitochondrial calcium and the regulation of metabolism in the heart. *Journal of Molecular and Cellular Cardiology*, 78:35–45, 2015.

[128] K. Yang, M.G. Bonini, and S.C. Dudley Jr. Mitochondria and arrhythmias. *Free Radical Biology and Medicine*, 71:351–361, 2014.

[129] D.A. Brown and B. O'Rourke. Cardiac mitochondria and arrhythmias. *Cardiovascular Research*, 88:241–249, 2010.

[130] M.A. Aon, S. Cortassa, F.G. Akar, D.B. Brown, L. Zhou, and B. O'Rourke. From mitochondrial dynamics to arrhythmias. *The International Journal of Biochemistry & Cell Biology*, 41:1940–1948, 2009.

[131] L.D. Gauthier, J.L. Greenstein, and R.L. Winslow. Toward an integrative computational model of the guinea pig cardiac myocyte. *Frontiers in Physiology*, 3:244, 2012.

[132] A. Hatano, J. Okada, T. Washio, T. Hisada, and S. Sugiura. A three-dimensional simulation model of cardiomyocyte integrating excitation-

contraction coupling and metabolism. *Biophysical Journal*, 101:2601–2610, 2011.

[133] R.K. Dash and D.A. Beard. Analysis of cardiac mitochondrial Na^+Ca^{2+} exchanger kinetics with a biophysical model of mitochondrial Ca^{2+} handing suggests a 3 : 1 stoichiometry. *Journal of Physiology*, 586:32673285, 2008.

[134] G.S.B. Williams, L. Boyman, A.C. Chikando, R.J. Khairallah, and W.J. Lederer. Mitochondrial calcium uptake. *PNAS*, 110:10479–10486, 2013.

[135] D. Sato, T.R. Shannon, and D.M. Bers. Sarcoplasmic reticulum structure and functional properties that promote long-lasting calcium sparks. *Biophysical Journal*, 110:382–390, 2016.

[136] C.I. del Genio, J. Gmez-Gardees, I. Bonamassa, and S. Boccaletti. Synchronization in networks with multiple interaction layers. *Science Advances*, 2:e1601679, 2016.

[137] M. Bray, S.P. Sheehy, and K.K. Parker. Sarcomere alignment is regulated by myocyte shape. *Cell Motility and the Cytoskeleton*, 65:641–651, 2008.

[138] P. Pérez-Treviño, J. Pérez-Treviño, C. Borja-Villa, N. García, and J. Altamirano. Changes in t-tubules and sarcoplasmic reticulum in ventricular myocytes in early cardiac hypertrophy in a pressure overload rat model. *Cellular Physiology and Biochemistry*, 37:1329–1344, 2015.

[139] W.E. Louch, O.M. Sejersted, and F. Swift. There goes the neighborhood: Pathological alterations in t-tubule morphology and consequences for cardiomyocyte Ca^{2+} handling. *Journal of Biomedicine and Biotechnology*, 2010:503906, 2010.

[140] A. Guo, C. Zhang, s. Wei, B. Chen, and L-S. Song. Emerging mechanisms of t-tubule remodelling in heart failure. *Cardiovascular Research*, 98:204–215, 2013.

[141] W.E. Louch, V. Bito, F.R. Heinzel, R. Macianskiene, J. Vanhaecke, W. Flameng, K. Mubagwa, and K.R. Sipido. Reduced synchrony of Ca^{2+} release

with loss of t-tubules - a comparison to Ca^{2+} release in human failing myocytes. *Cardiovascular Research*, 62:63–73, 2004.

[142] C. Peracchia. Chemical gating of gap junction channels: Roles of calcium, ph and calmodulin. *Biochimica et Biophysica Acta - Biomembranes*, 1662:61–80, 2004.

[143] C. Oka, H. Matsuda, N. Sarai, and A. Noma. Modeling the calcium gate of cardiac gap junction channel. *Journal of Physiological Sciences*, 56:79–85, 2006.

[144] T.A.B. van Veen, H.V.M. van Rijen, and T. Opthof. Cardiac gap junction channels: modulation of expression and channel properties. *Cardiovascular Research*, 51:217–229, 2001.

[145] P.S. Skardal, A. Karma, and J.G. Restrepo. Spatiotemporal dynamics of calcium-driven cardiac alternans. *PHYSICAL REVIEW E*, 89:052707, 2014.

[146] R. FitzHugh. Impulses and physiological states in theoretical models of nerve membrane. *Biophysical Journal*, 1:445–466, 1961.

[147] A. Arenas, A. Diaz-Guilera, J. Kurths, Y. Moreno, and C. Zhou. Synchronization in complex networks. *Physics Reports*, 469:93–153, 2008.